Synthesis and Characterization of divalent metal-betaine-bistriflimide complexes: a property comparison with metal bistriflimide salts

Luca Guglielmero*[a], Lidia Ciccone,[b,c] Andrea Mezzetta[b], Felicia D'Andrea[b], Lorenzo Guazzelli[b], Christian Silvio Pomelli[b].

[a] Scuola Normale Superiore, Piazza dei Cavalieri 7, 56126 Pisa.

[b] Università di Pisa, Dipartimento di Farmacia, Via Bonanno 33, 56126 Pisa.

[c] Centre for Instrumentation Sharing of the University of Pisa (CISUP), Lungarno Pacinotti 43, 56126 Pisa, Italy.

Supporting information

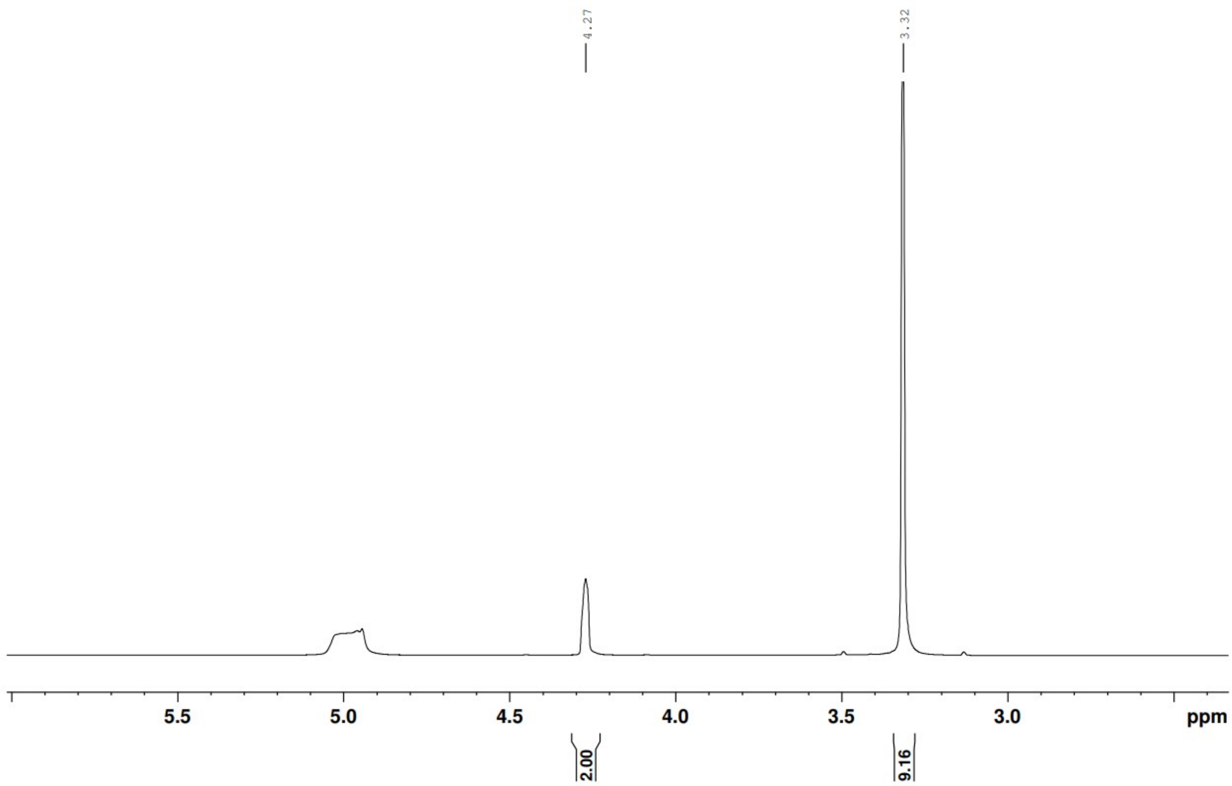

Figure S1. ^{1}H-NMR spectrum of [HBet][Tf_2N] in CD_3OD.

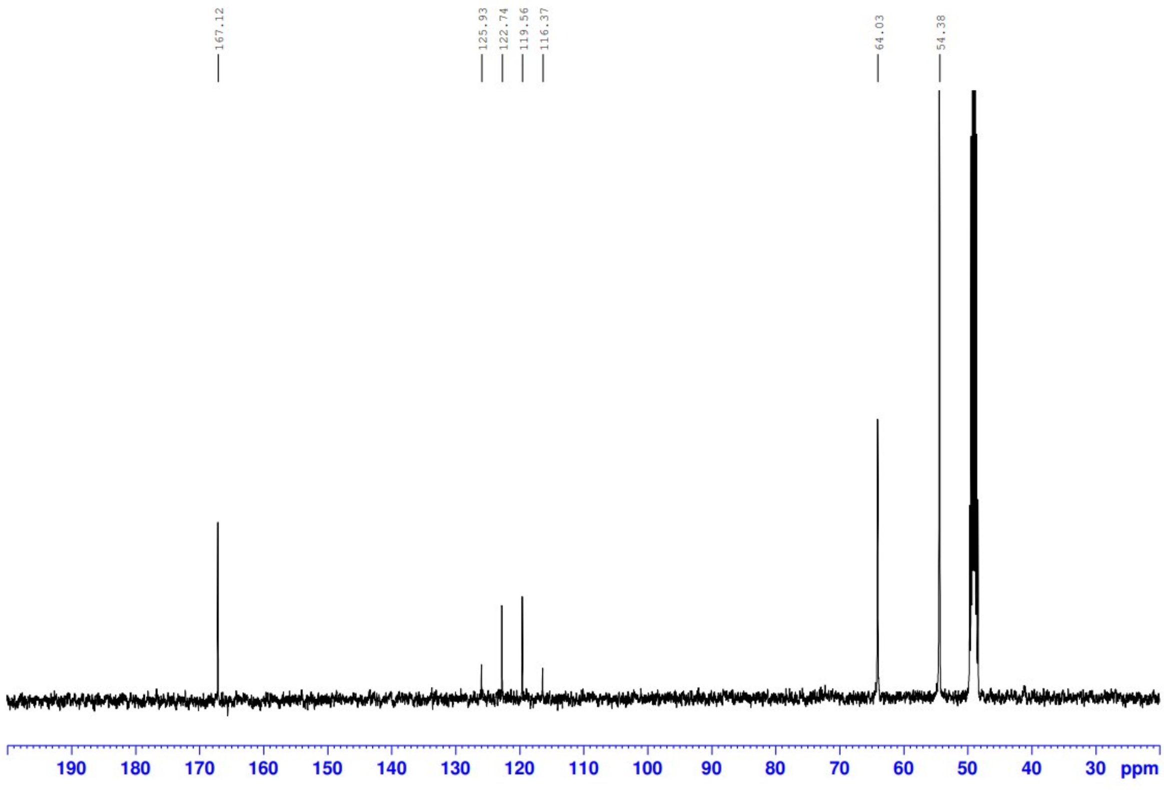

Figure S2. ^{13}C-NMR spectrum of [HBet][Tf_2N] in CD_3OD.

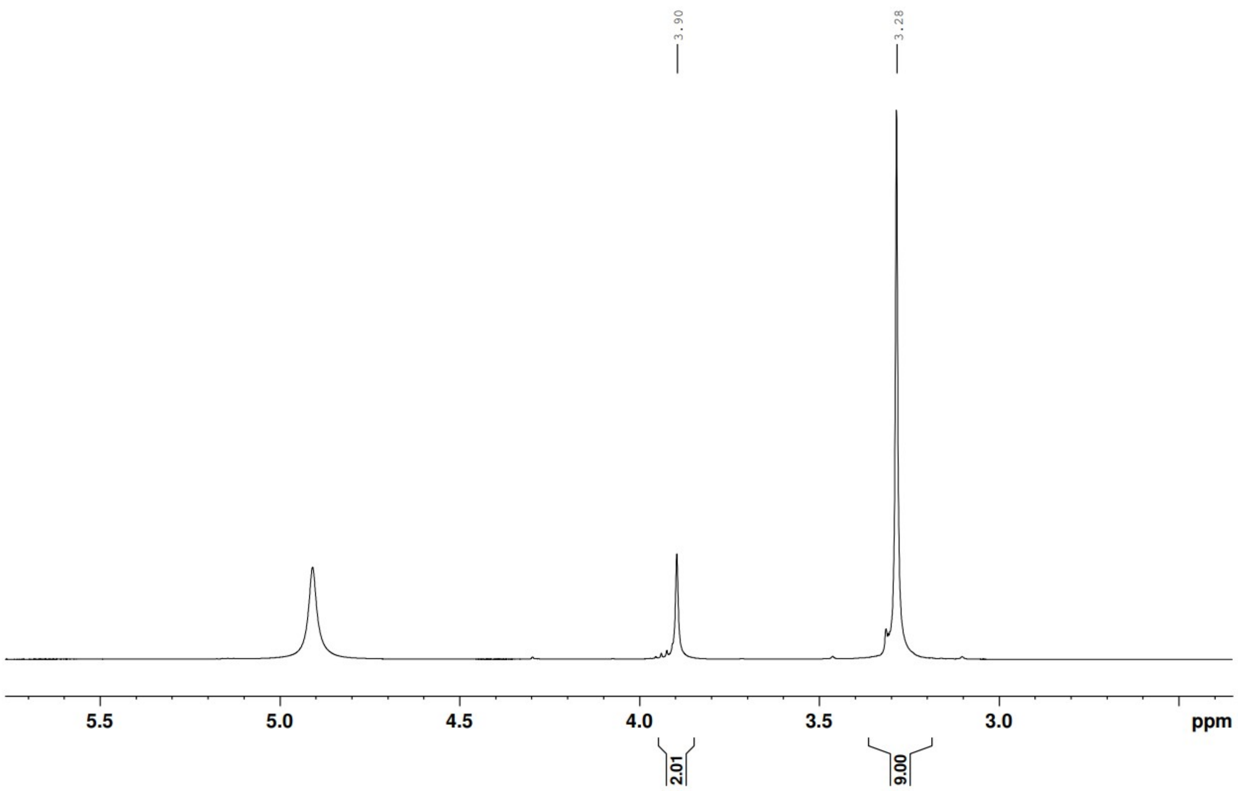

Figure S3. ^{1}H-NMR spectrum of $Mg[Bet]_2[Tf_2N]_2$ in CD_3OD.

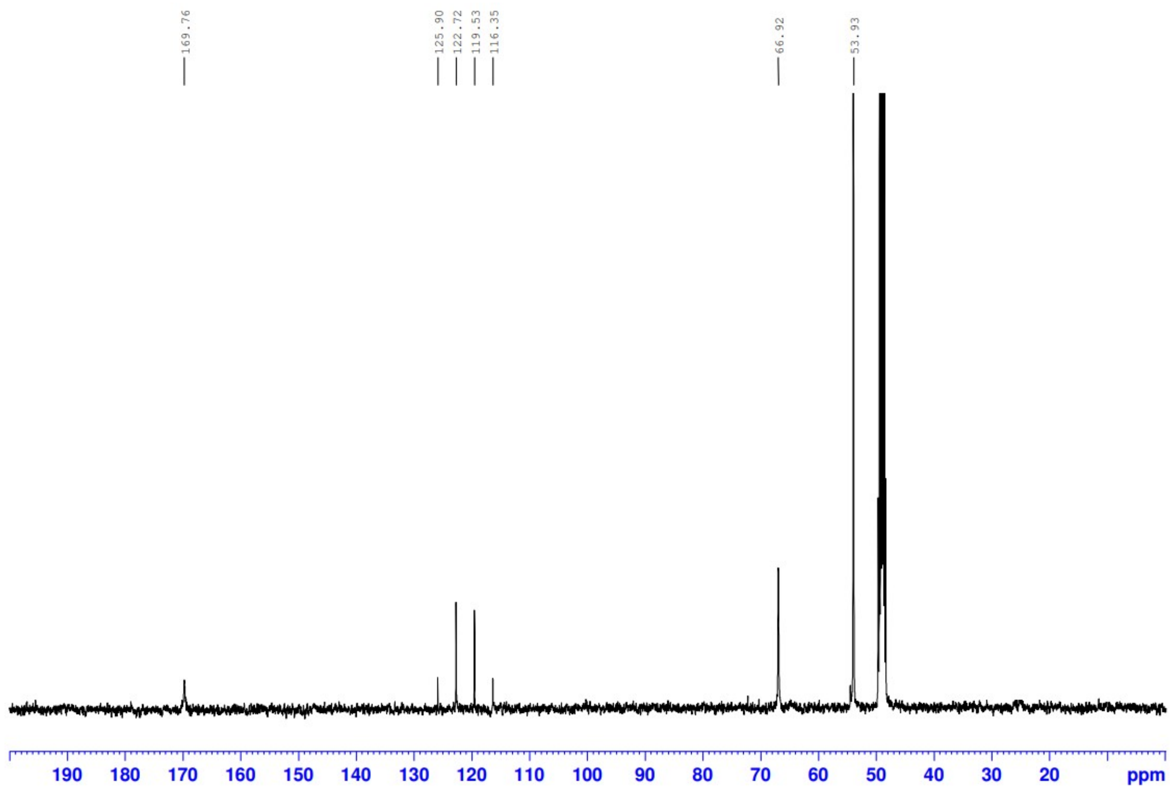

Figure S4. ^{13}C-NMR spectrum of $Mg[Bet]_2[Tf_2N]_2$ in CD_3OD.

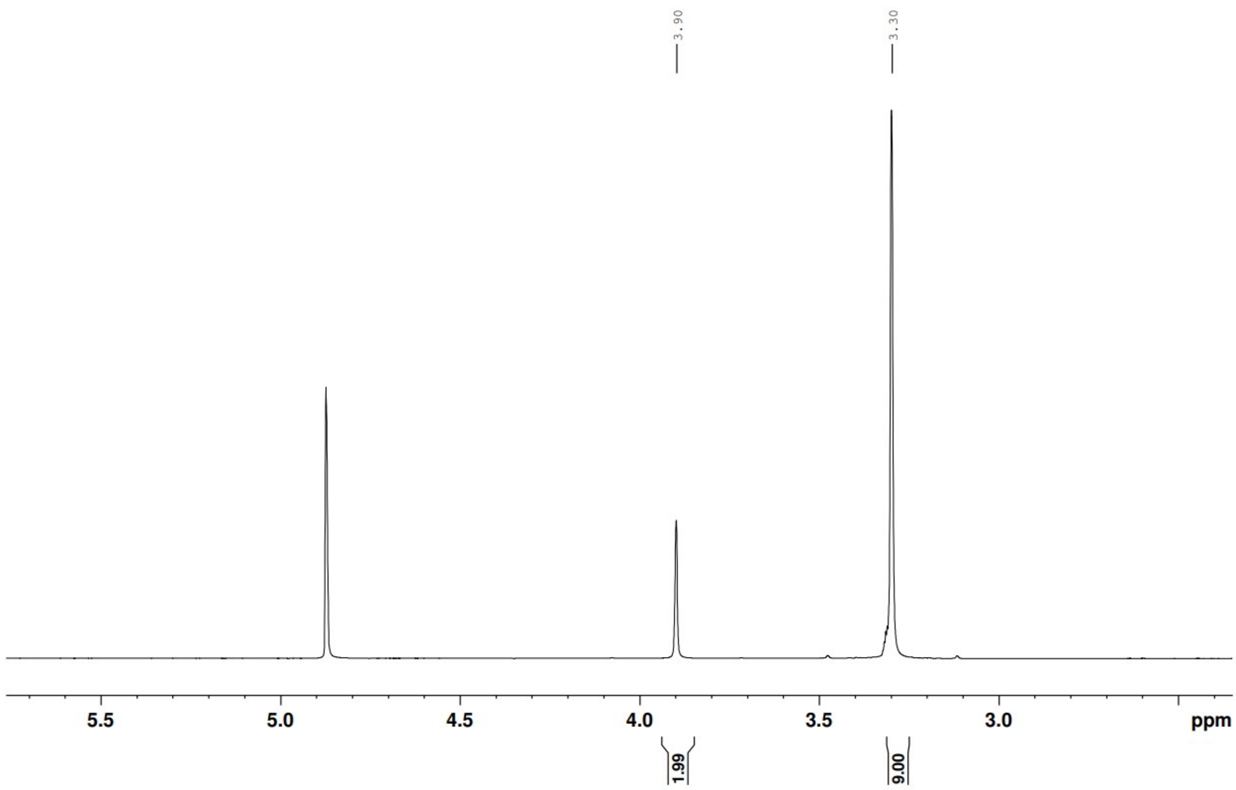

Figure S5. ^{1}H-NMR spectrum of $Ca[Bet]_2[Tf_2N]_2$ in CD_3OD.

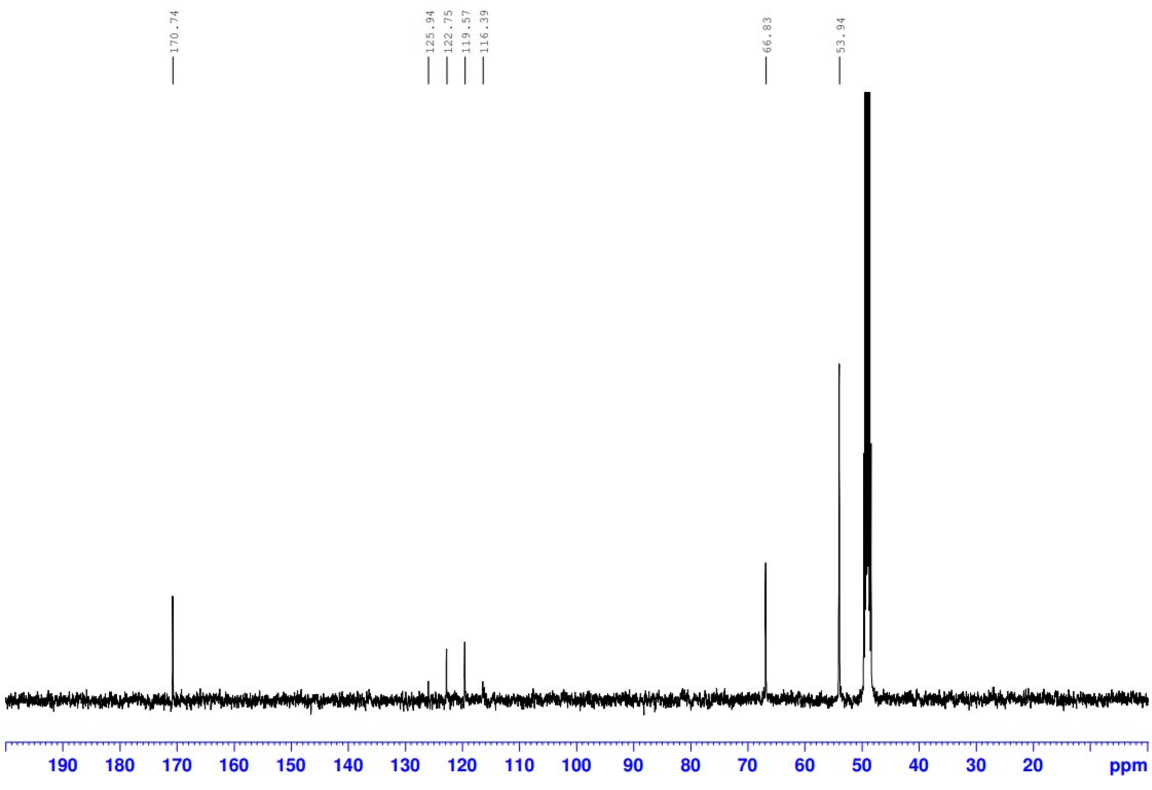

Figure S6. ^{13}C-NMR spectrum of $Ca[Bet]_2[Tf_2N]_2$ in CD_3OD.

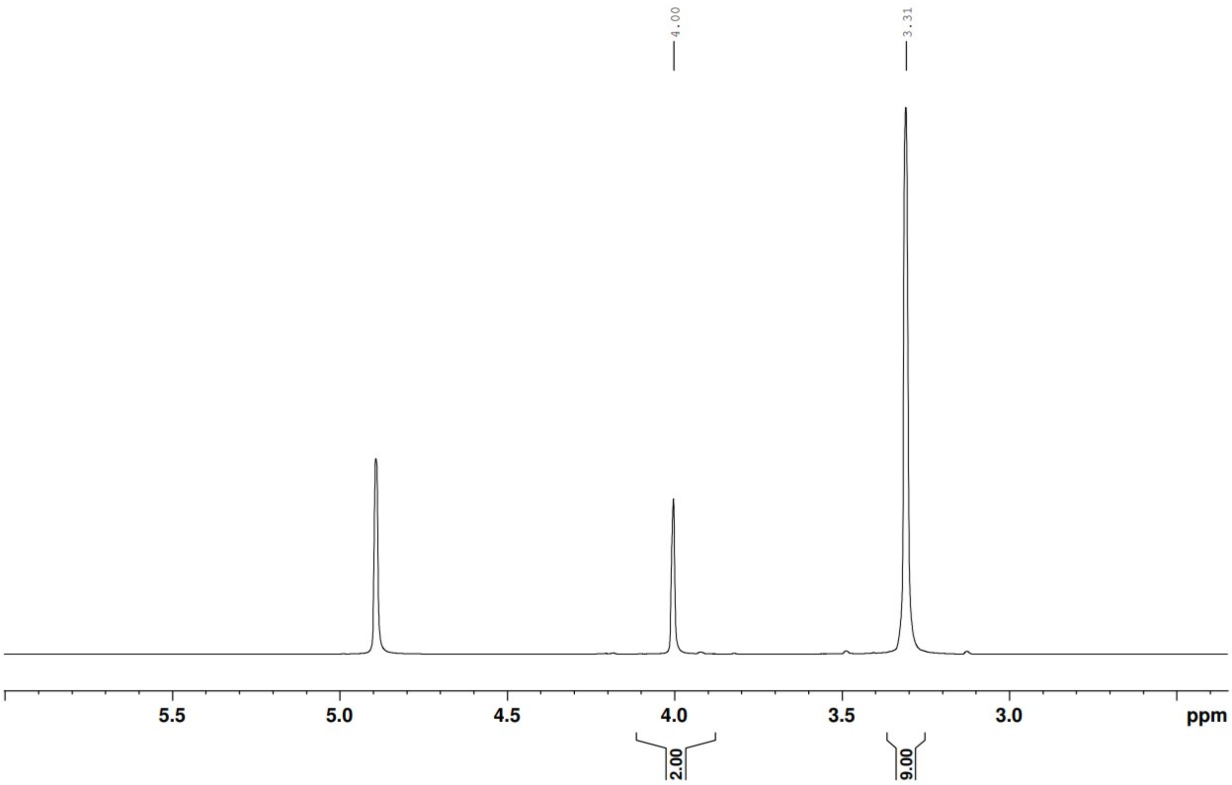

Figure S7. ^{1}H-NMR spectrum of Zn[Bet]$_2$[Tf$_2$N]$_2$ in CD_3OD.

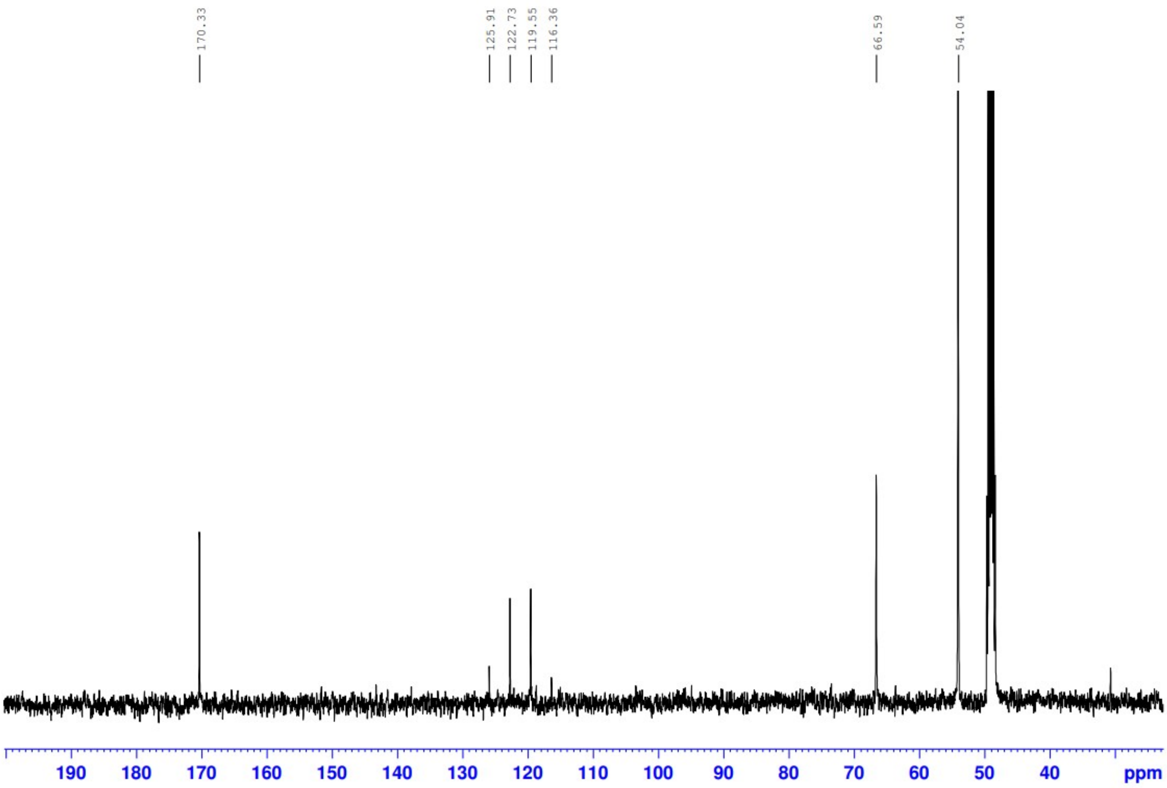

Figure S8. ^{13}C-NMR spectrum of Zn[Bet]$_2$[Tf$_2$N]$_2$ in CD_3OD.

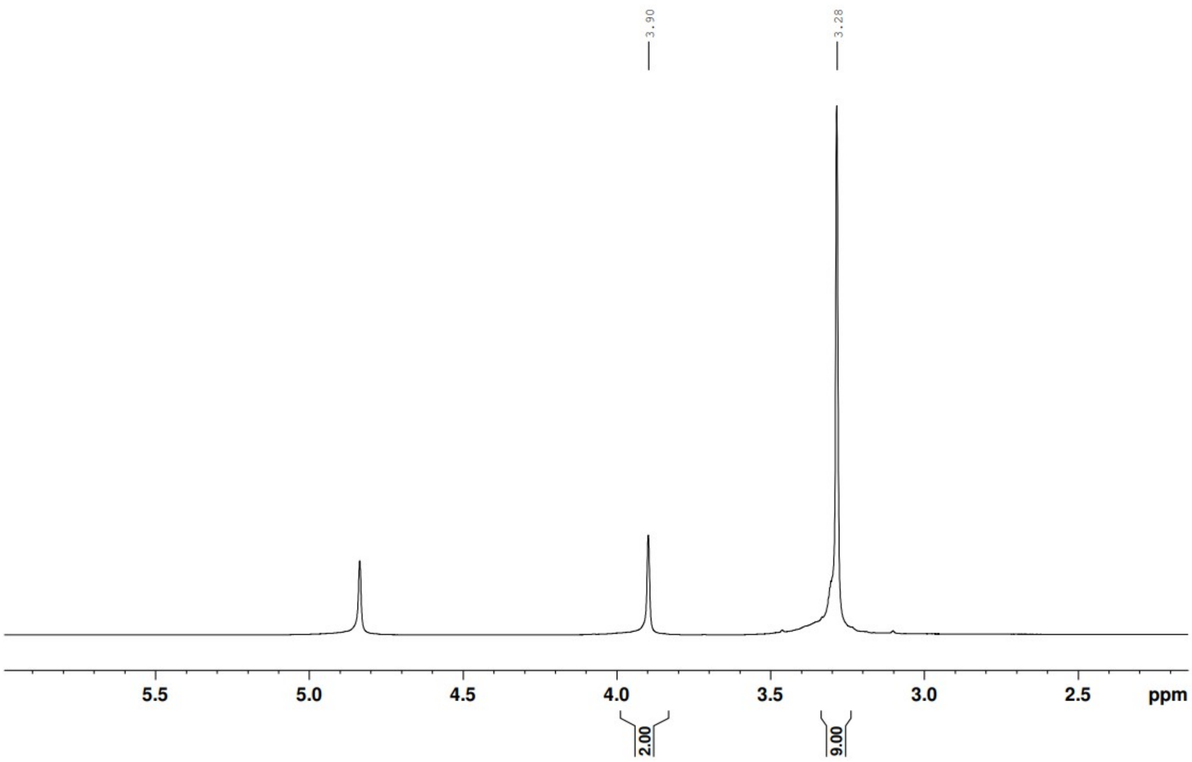

Figure S9. ^{1}H-NMR spectrum of $Mg[Bet]_3[Tf_2N]_2$ in CD_3OD.

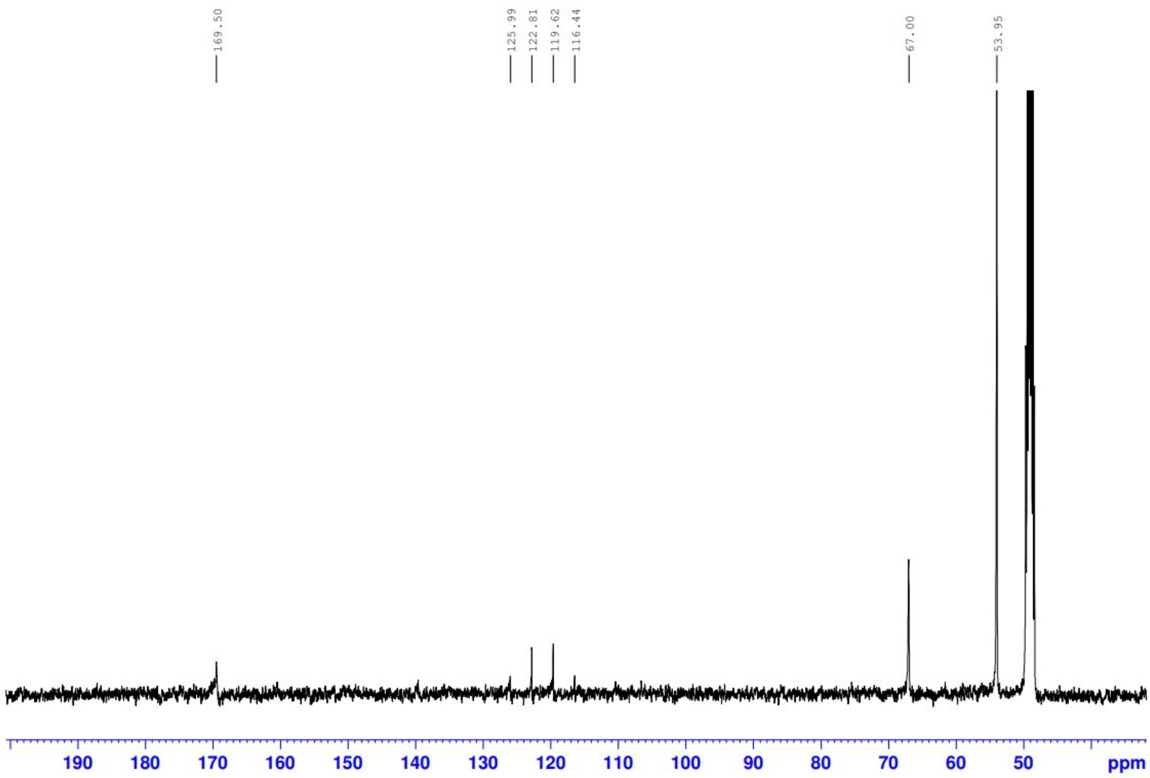

Figure S10. ^{13}C-NMR spectrum of $Mg[Bet]_3[Tf_2N]_2$ in CD_3OD.

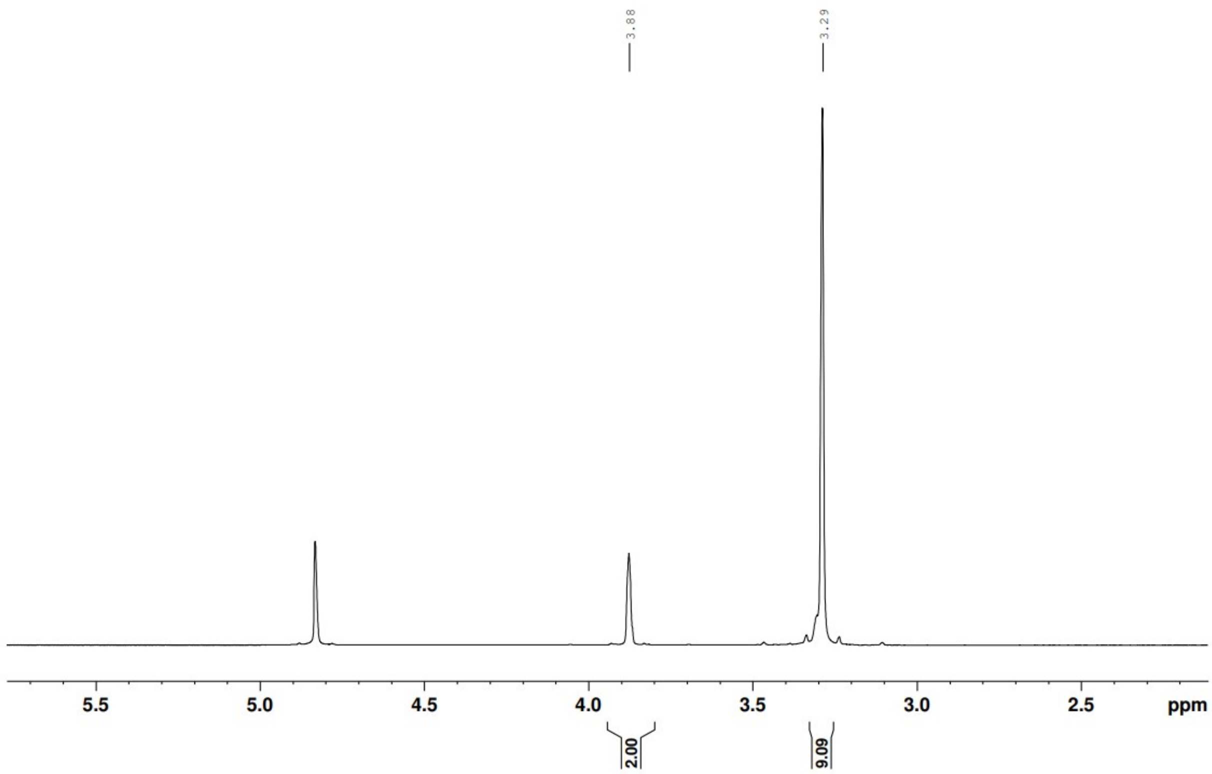

Figure S11. ^{1}H-NMR spectrum of $Ca[Bet]_3[Tf_2N]_2$ in CD_3OD.

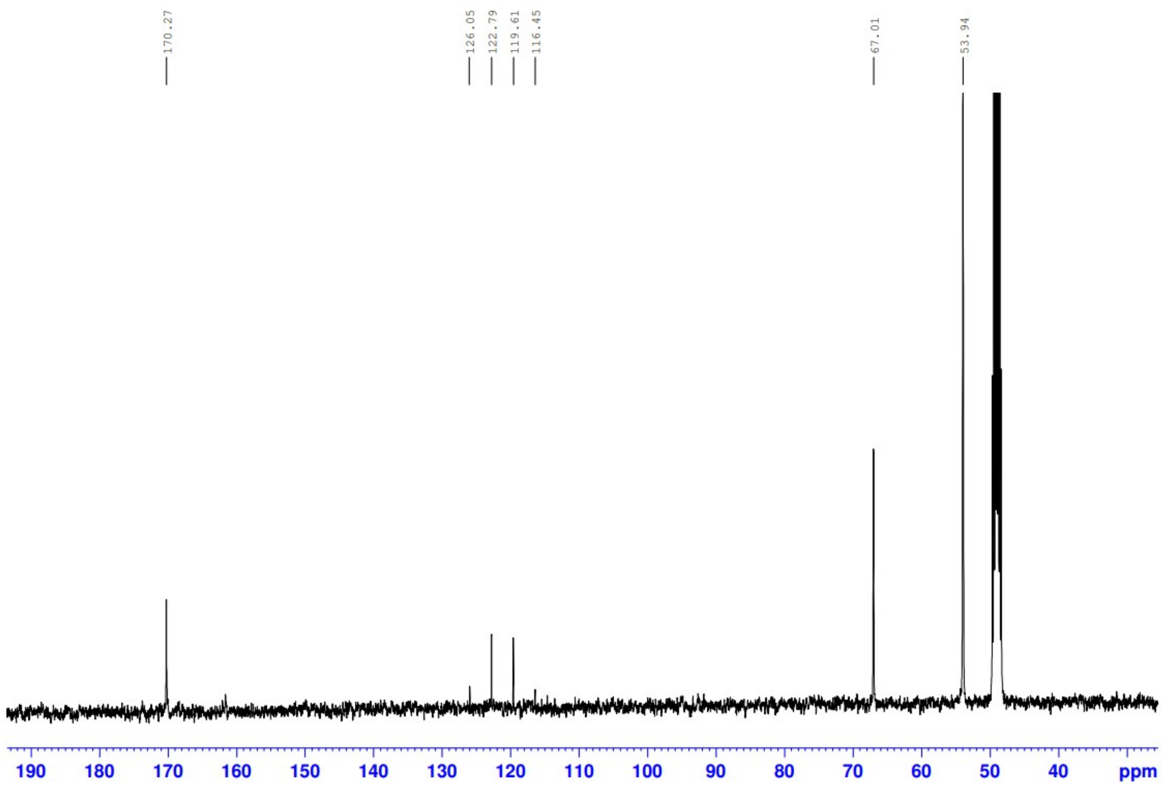

Figure S12. ^{13}C-NMR spectrum of $Ca[Bet]_3[Tf_2N]_2$ in CD_3OD.

	$Ca[Bet]_3[Tf_2N]_2$	$Cu_2[Bet]_4[Tf_2N]_4$
Crystal data		
Formula	$C_{19}H_{33}CaF_{12}N_5O_{14}S_4$	$C_{30}H_{52}Cu_2F_{24}N_8O_{26}S_8$
Molecular weight	951.82	1780.38
Size (mm^3)	0.05 × 0.05 × 0.250	0.29 × 0.24 × 0.20
Crystal system, space group	Triclinic, *P*-1 (No. 2)	Orthorhombic, *Pccn* (No. 56)
a (Å)	9.0322(2)	21.4028(8)
b (Å)	15.1177(4)	22.6225(9)
c (Å)	15.2478(4)	13.9791(6)
α (°)	105.4270(10)	90
β (°)	105.0780(10)	90
γ (°)	101.0740(10)	90
V (Å^3)	1860.00(8)	6768.5(5)
Z	2	4
D_{calc} (g cm^{-3})	1.714	1.747
Data collection and refinement		
Radiation, λ (Å)	Mo*K*α, 0.71073	Mo*K*α, 0.71073
Temperature (K)	100	100
$2\theta_{max}$ (°)	56.55	60.10
μ (mm^{-1})	0.519	1.017
Abs corr	multi-scan	multi-scan
F(000)	972.0	3592
no. of measured reflns	52290	107323
no. of unique reflns	9211	9890
no. of obsd reflns ($I_0 > 2\sigma(I_0)$)	8259	8676
R_{int}	0.0361	0.0358
R_σ	0.025	0.0177
Range of *h,k,l*	$-11 \leq h \leq 12$ $-20 \leq k \leq 20$ $-20 \leq l \leq 20$	$-29 \leq h \leq 30$ $-31 \leq k \leq 31$ $-19 \leq l \leq 19$
GOF on F^2	1.051	1.003
R_1	0.0324	0.0308
R_1 (all data)	0.0362	0.0365
wR_2	0.0801	0.0819
wR_2 (all data)	0.0826	0.0860
Maximum and minimum residual peak (*e* Å^{-3})	+0.916 -0.471	+0.86 -0.57

Table S1. Crystallographic data for Calcium(II) and Copper(II) complexes

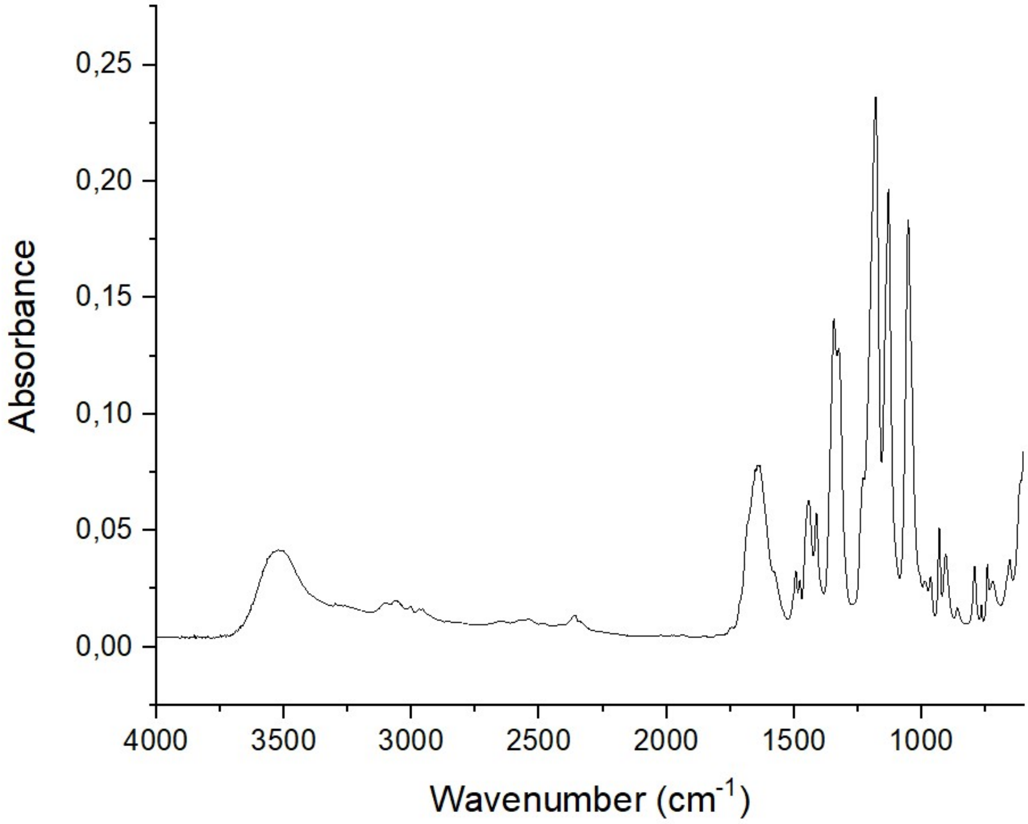

Figure S13. ATR-FTIR spectrum of $Mg[Bet]_2[Tf_2N]_2$.

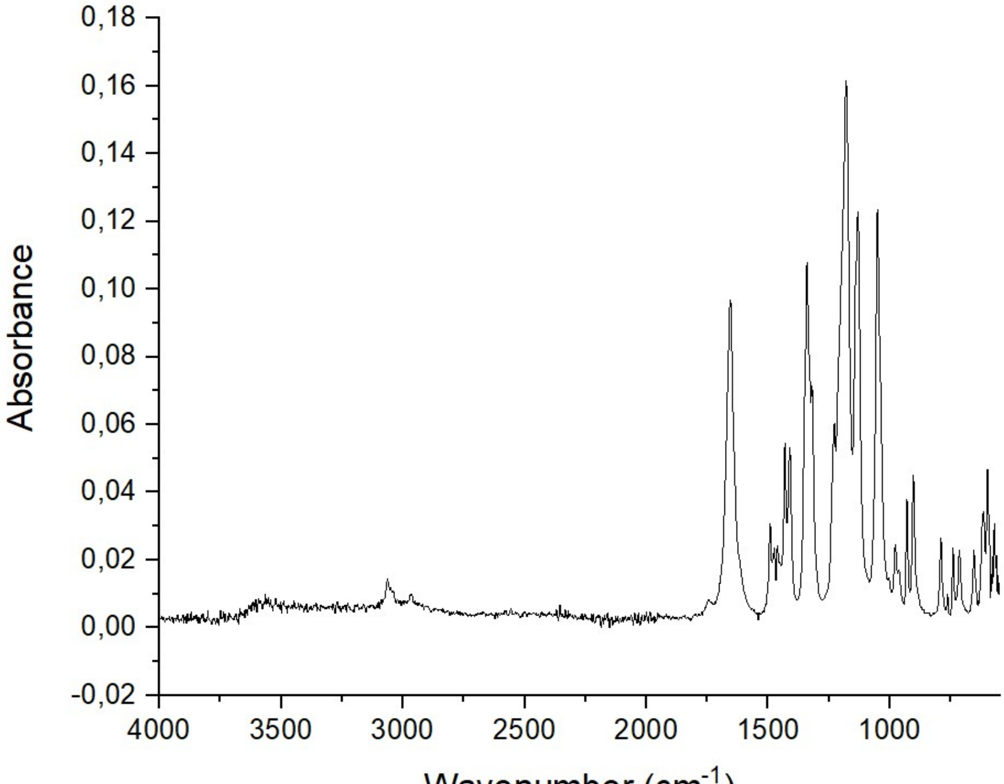

Figure S14. ATR-FTIR spectrum of $Mg[Bet]_3[Tf_2N]_2$.

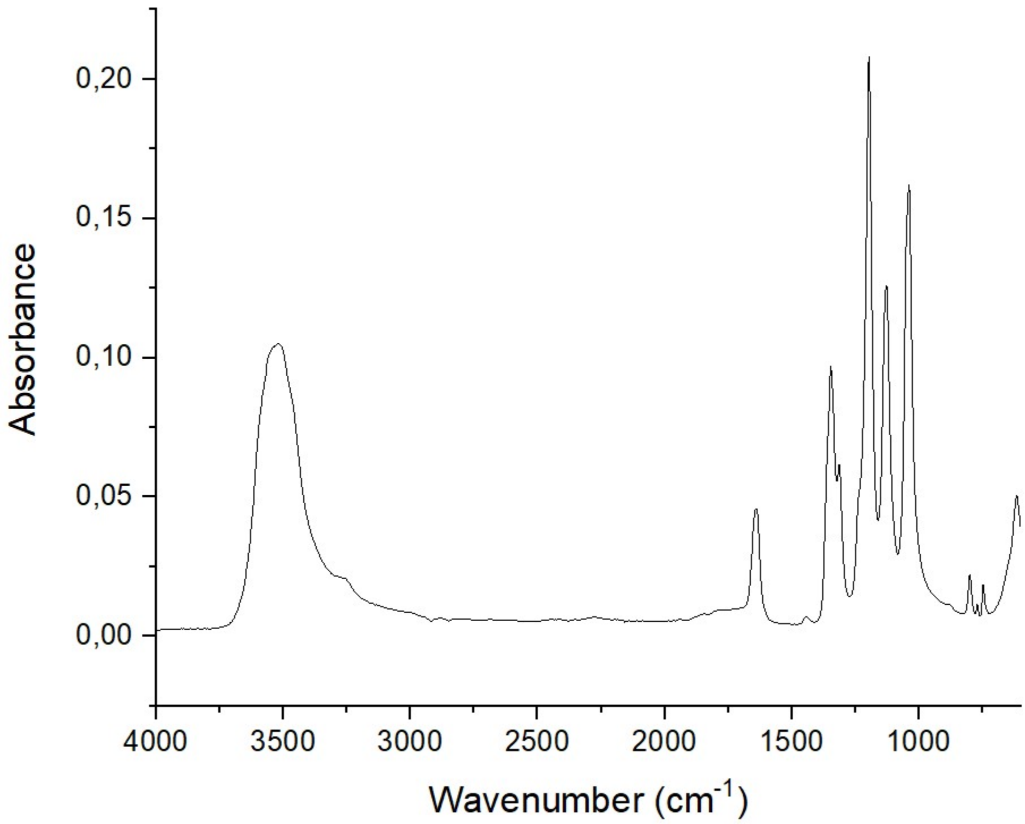

Figure S15. ATR-FTIR spectrum of $Mg[Tf_2N]_2$

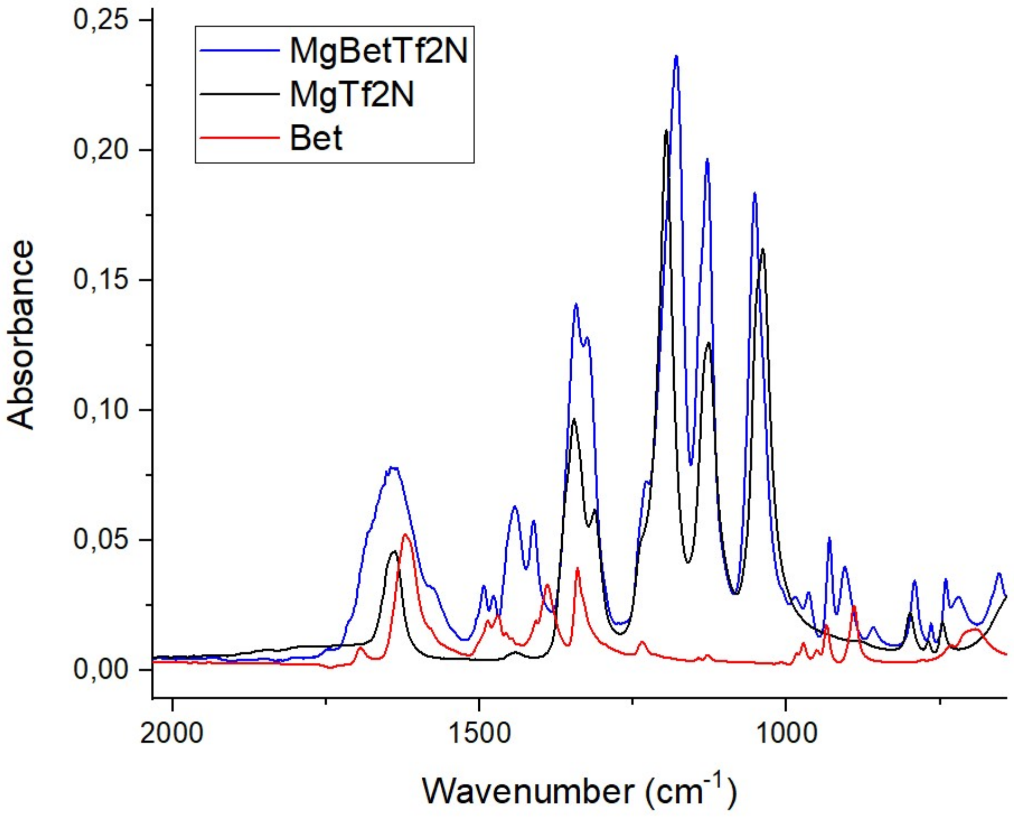

Figure S16. Comparison of ATR-FTIR spectra of $Mg[Bet]_2[Tf_2N]_2$, $Mg[Tf_2N]_2$ and betaine.

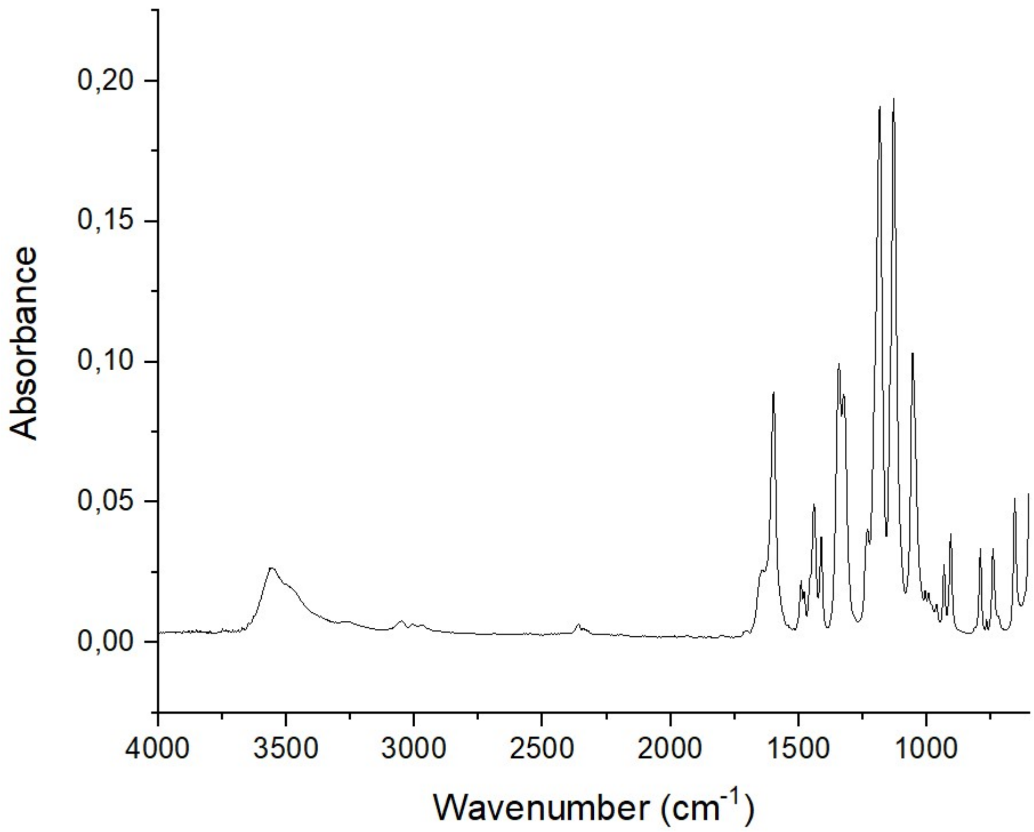

Figure S17. ATR-FTIR spectrum of Ca[Bet]$_2$[Tf$_2$N]$_2$

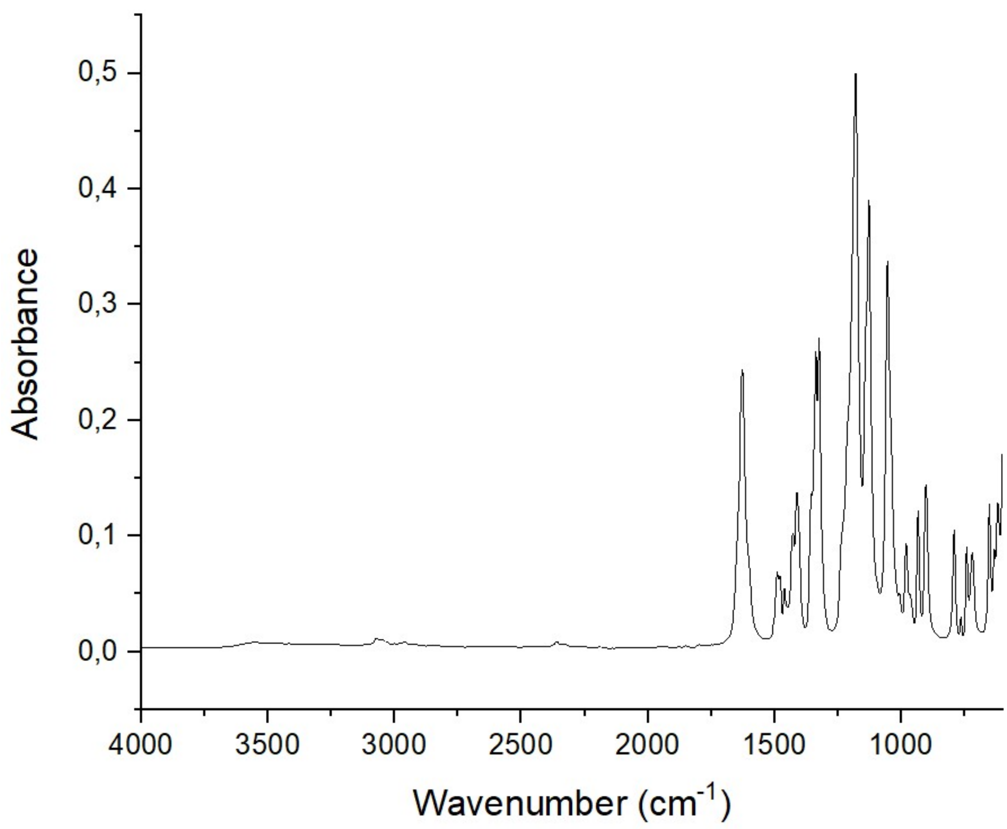

Figure S18a. ATR-FTIR spectrum of Ca[Bet]$_3$[Tf$_2$N]$_2$ (crystals)

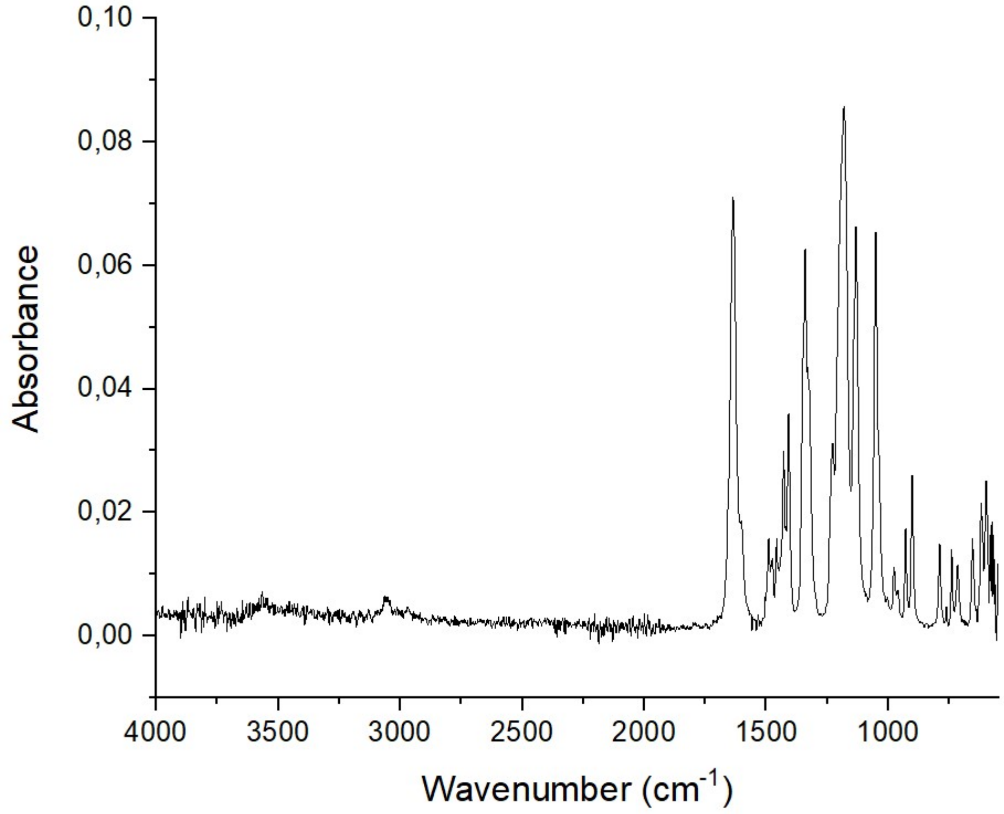

Figure S18b. ATR-FTIR spectrum of Ca[Bet]$_3$[Tf$_2$N]$_2$ (synthetized).

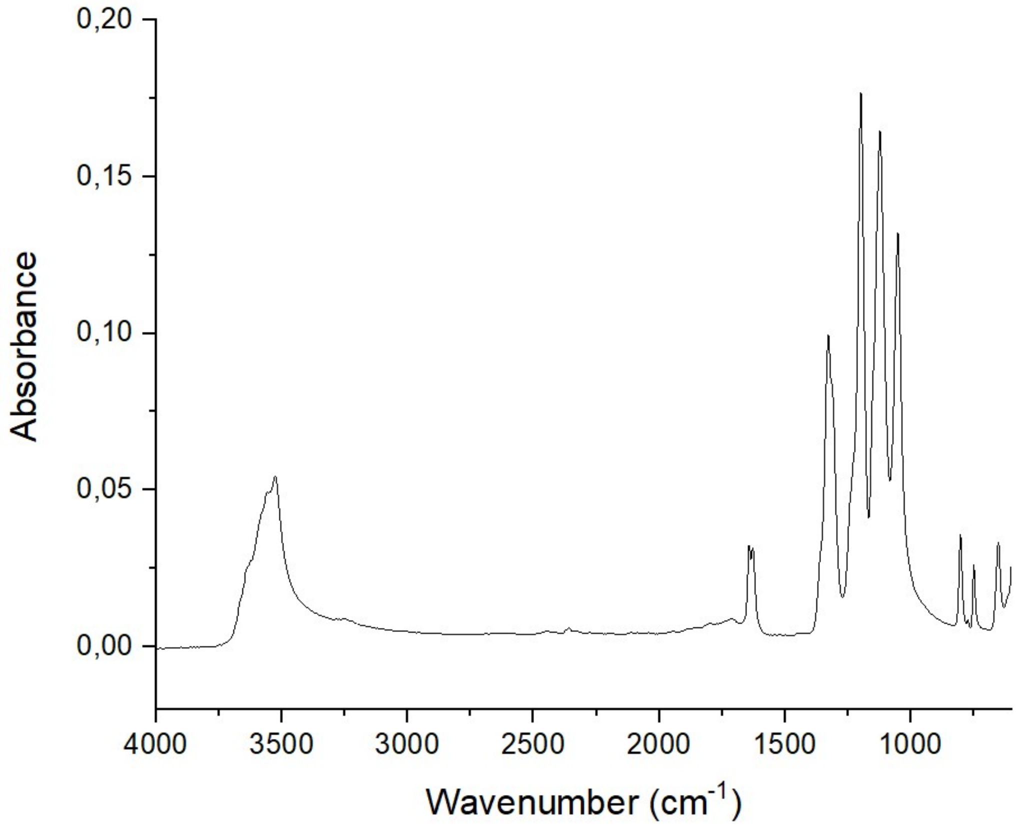

Figure S19. ATR-FTIR spectrum of Ca[Tf$_2$N]$_2$

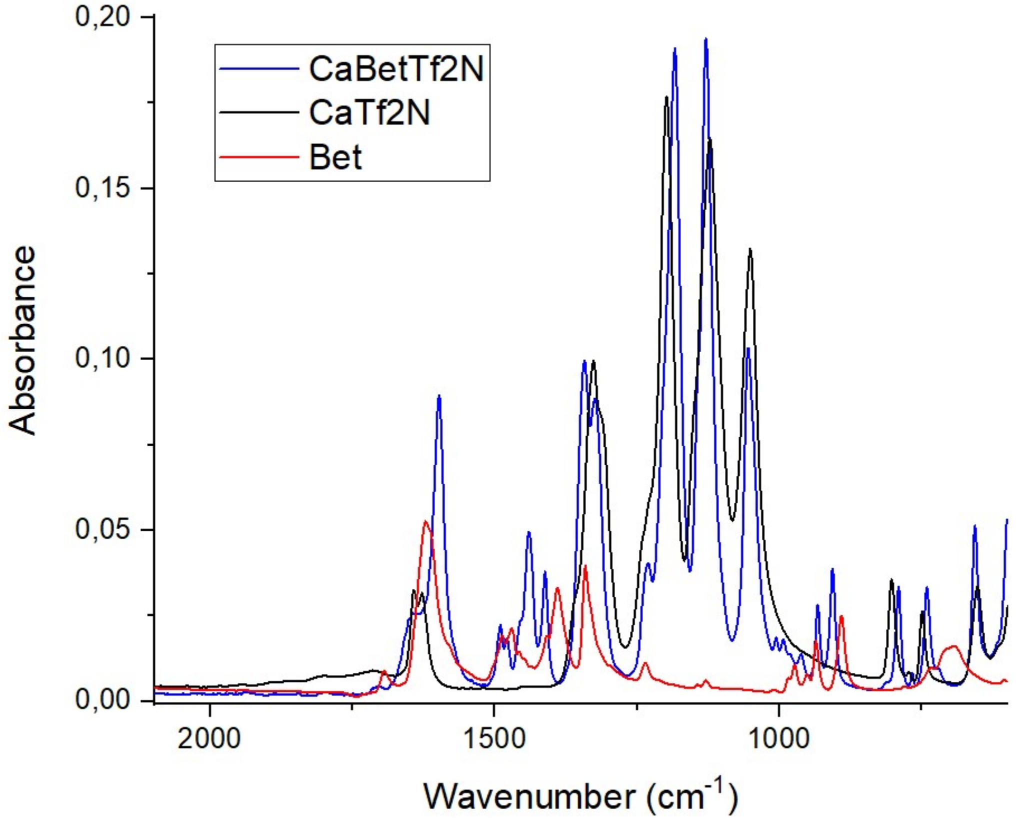

Figure S20. Comparison of ATR-FTIR spectra of Ca[Bet]$_2$[Tf$_2$N]$_2$, Ca[Tf$_2$N]$_2$ and betaine.

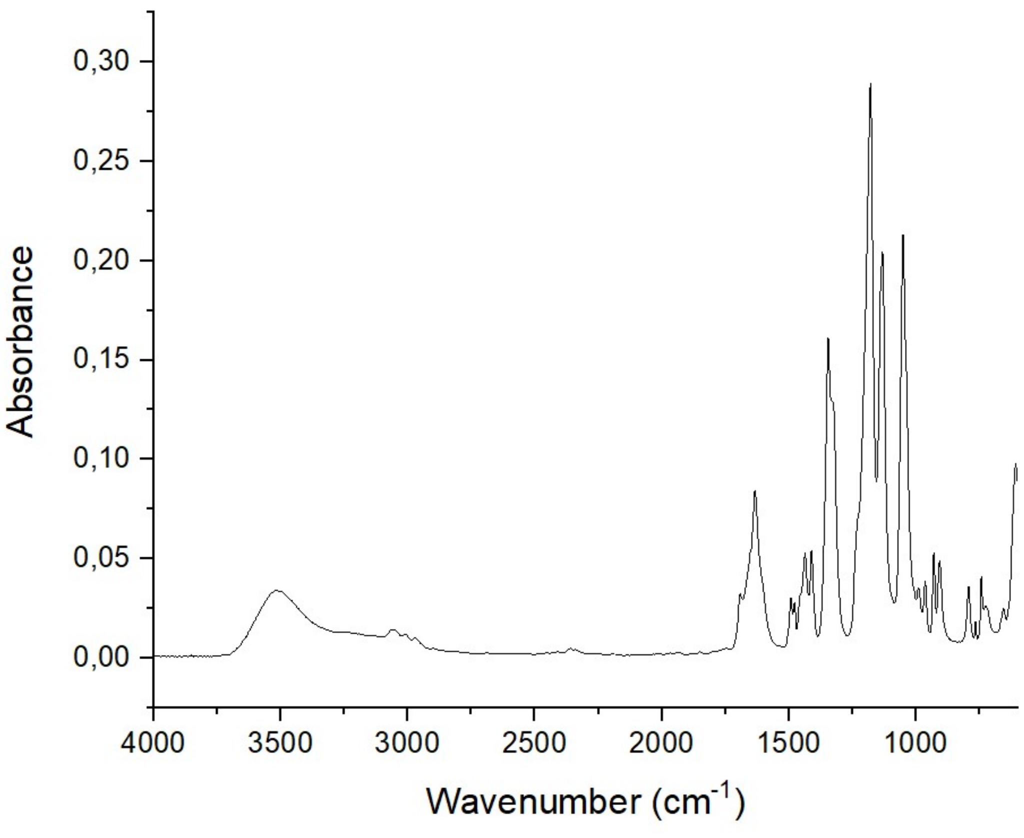

Figure S21. ATR-FTIR spectrum of Zn[Bet]$_2$[Tf$_2$N]$_2$

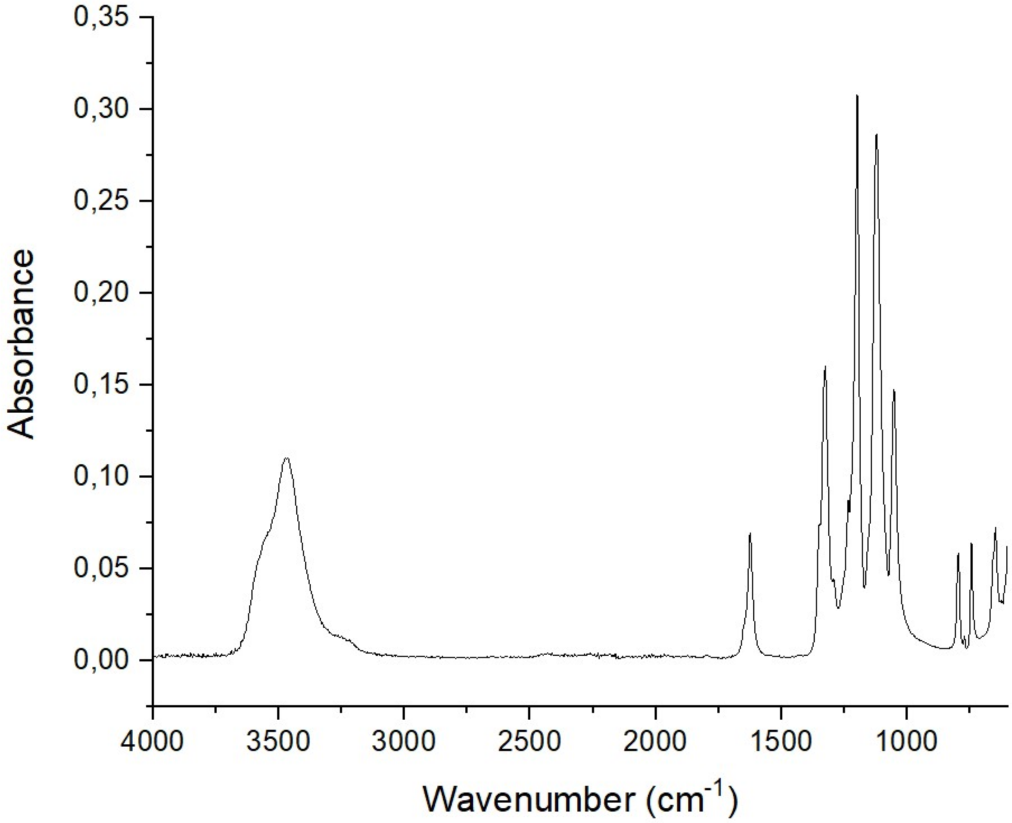

Figure S22. ATR-FTIR spectrum of $Zn[Tf_2N]_2$

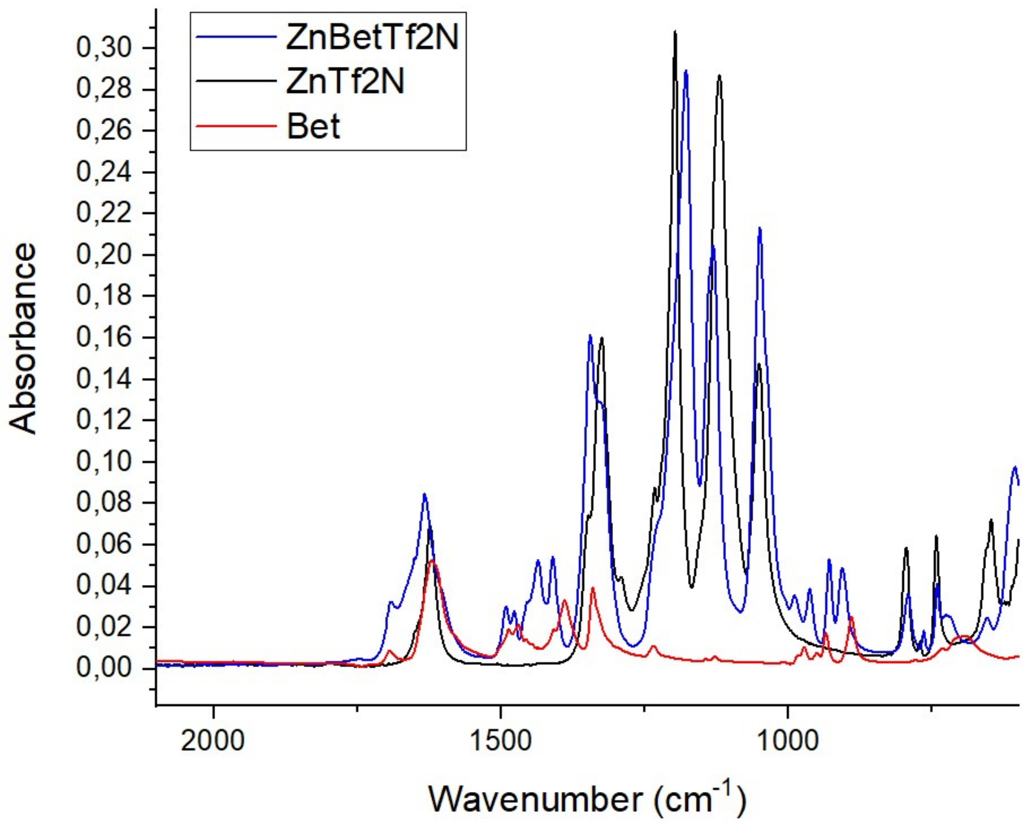

Figure S23. Comparison of ATR-FTIR spectra of $Zn[Bet]_2[Tf_2N]_2$, $Zn[Tf_2N]_2$ and betaine.

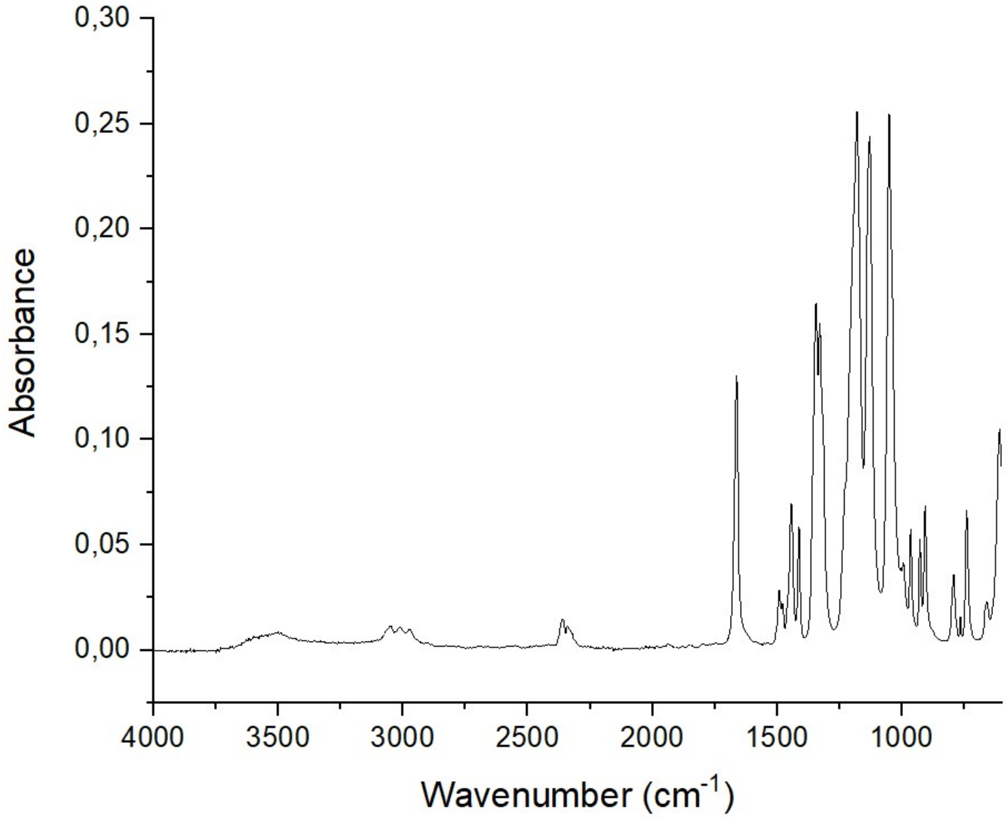

Figure S24. ATR-FTIR spectrum of $Cu[Bet]_2[Tf_2N]_2$.

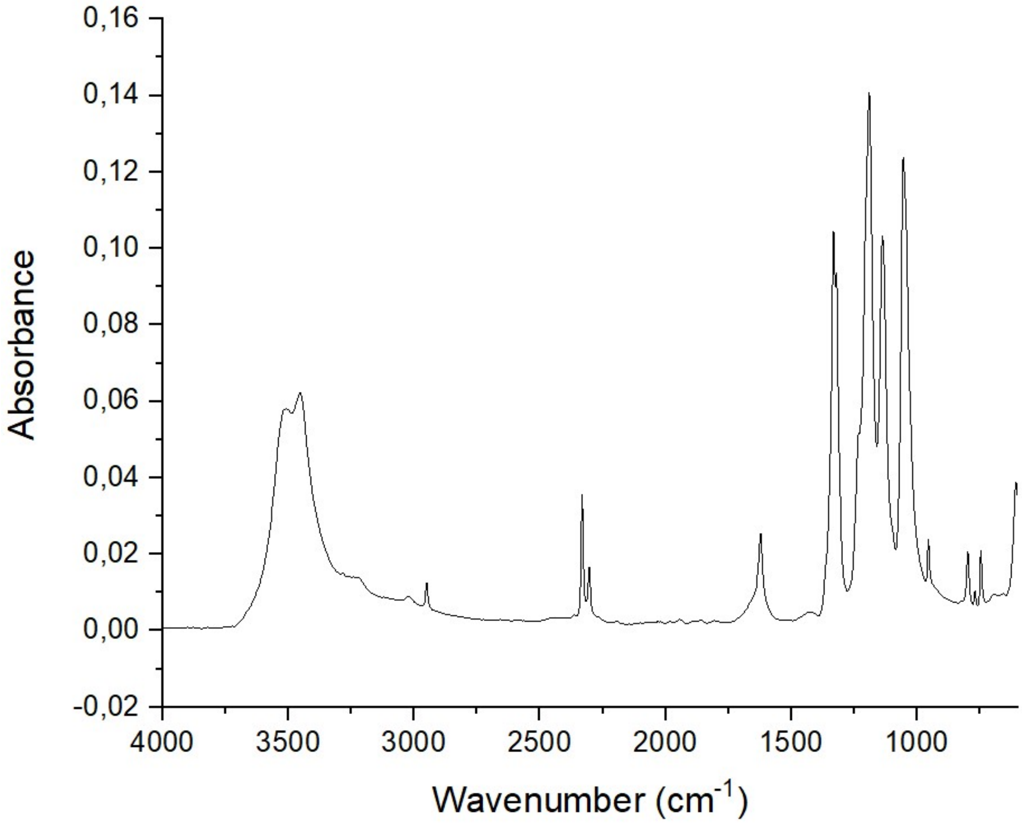

Figure S25. ATR-FTIR spectrum of $Cu[Tf_2N]_2$.

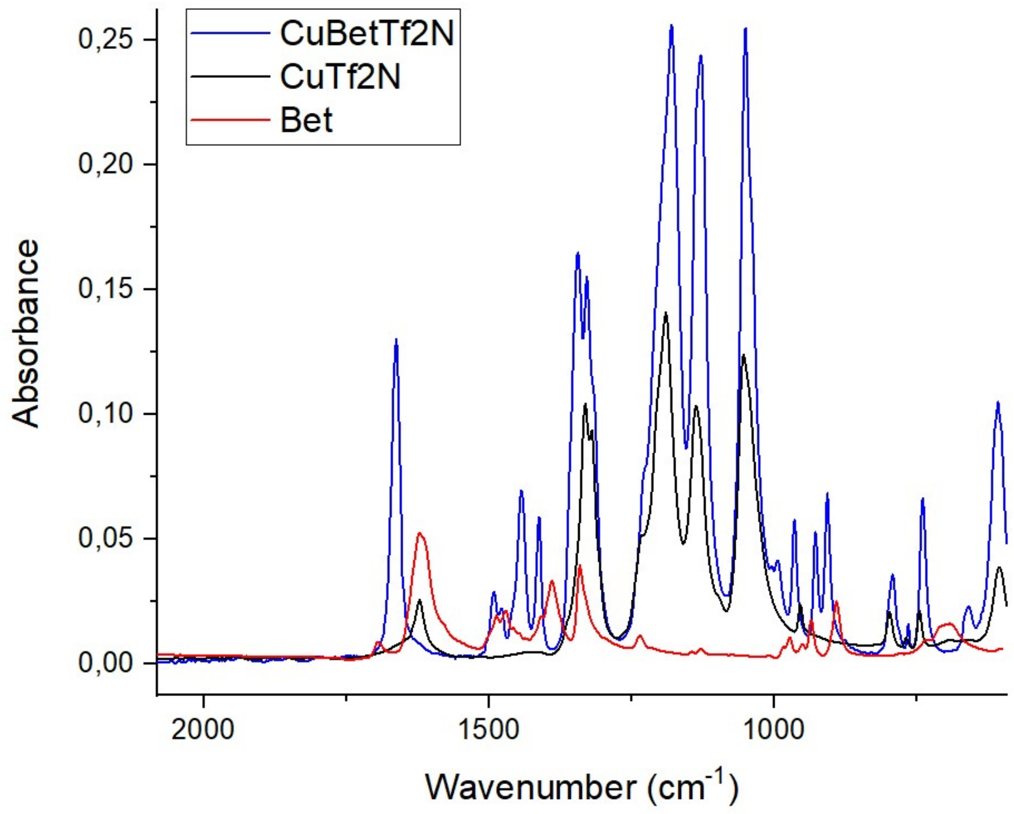

Figure S26. Comparison of ATR-FTIR spectra of $Cu[Bet]_2[Tf_2N]_2$, $Cu[Tf_2N]_2$ and betaine.

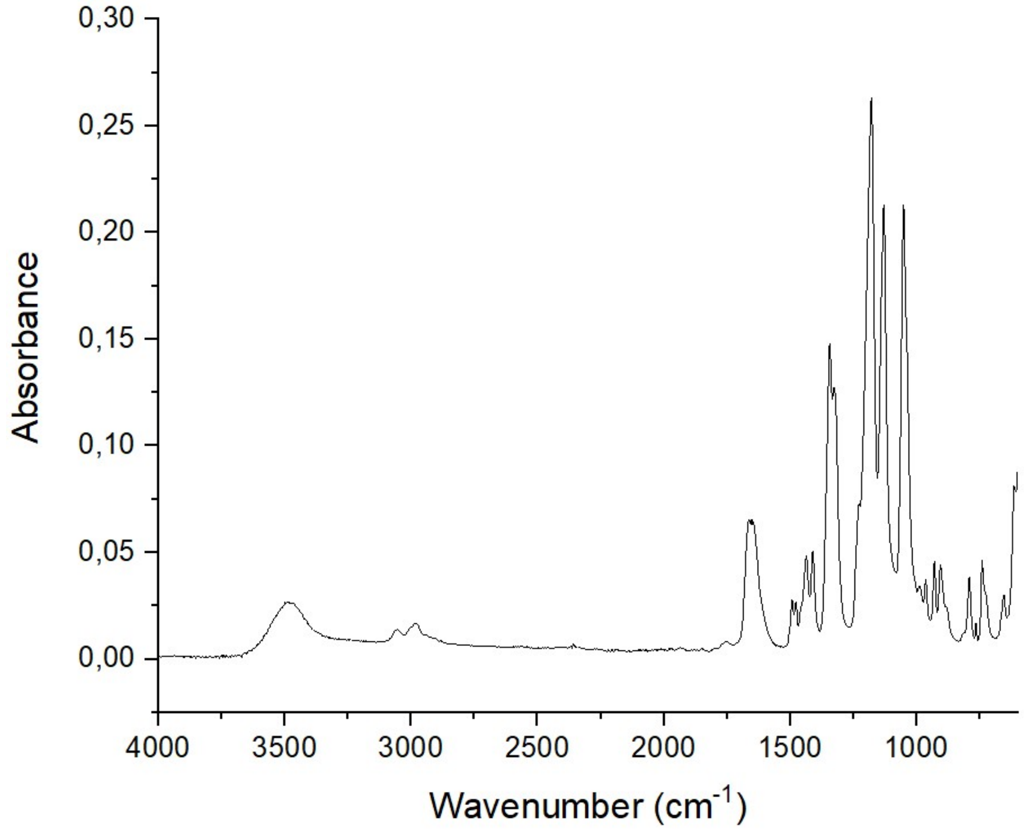

Figure S27. ATR-FTIR spectrum of $Ni[Bet]_2[Tf_2N]_2$.

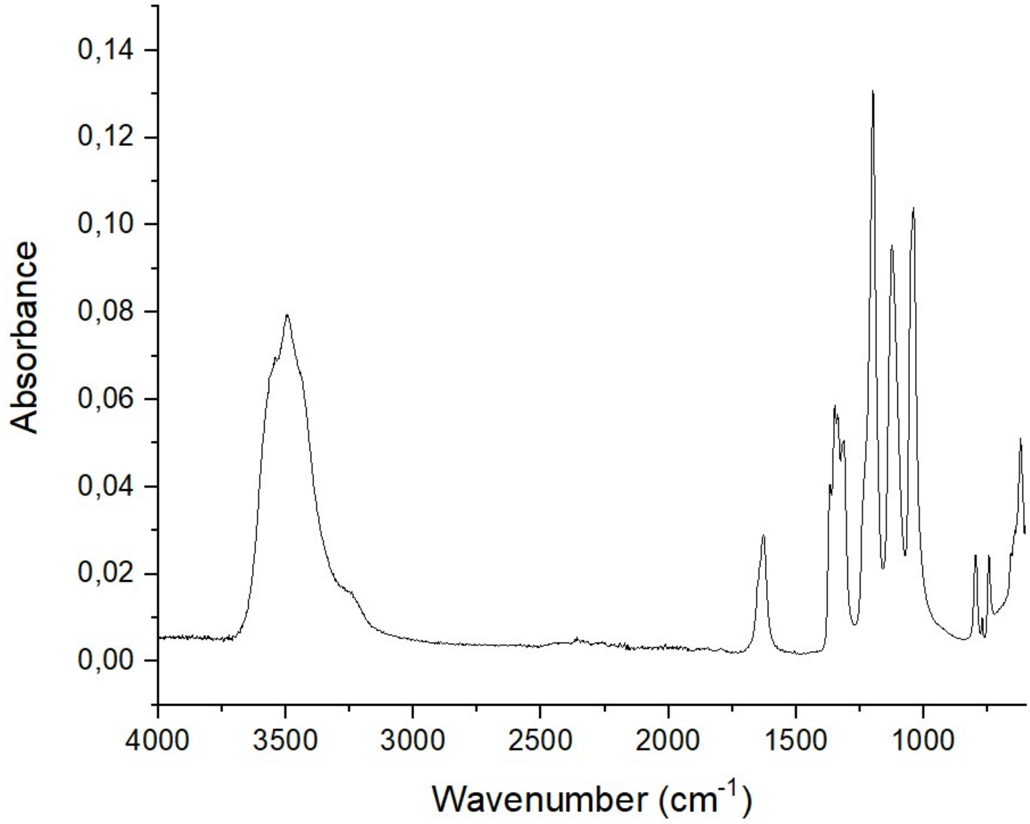

Figure S28. ATR-FTIR spectrum of $Ni[Tf_2N]_2$.

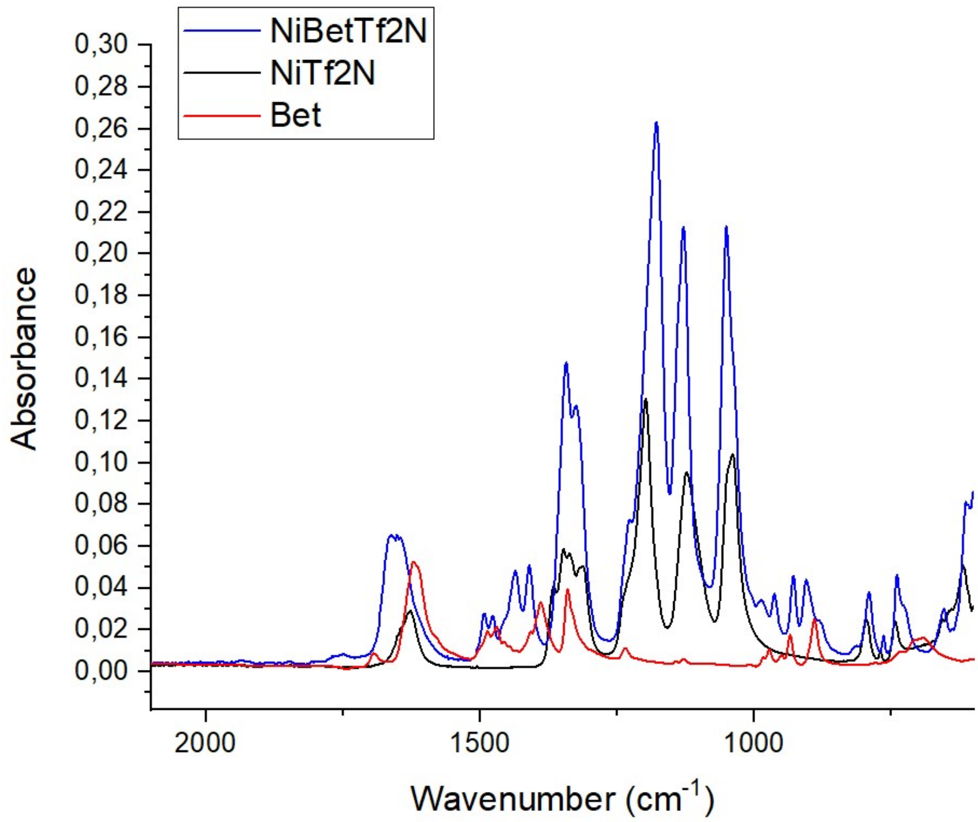

Figure S29. Comparison of ATR-FTIR spectra of $Cu[Bet]_2[Tf_2N]_2$, $Cu[Tf_2N]_2$ and betaine.

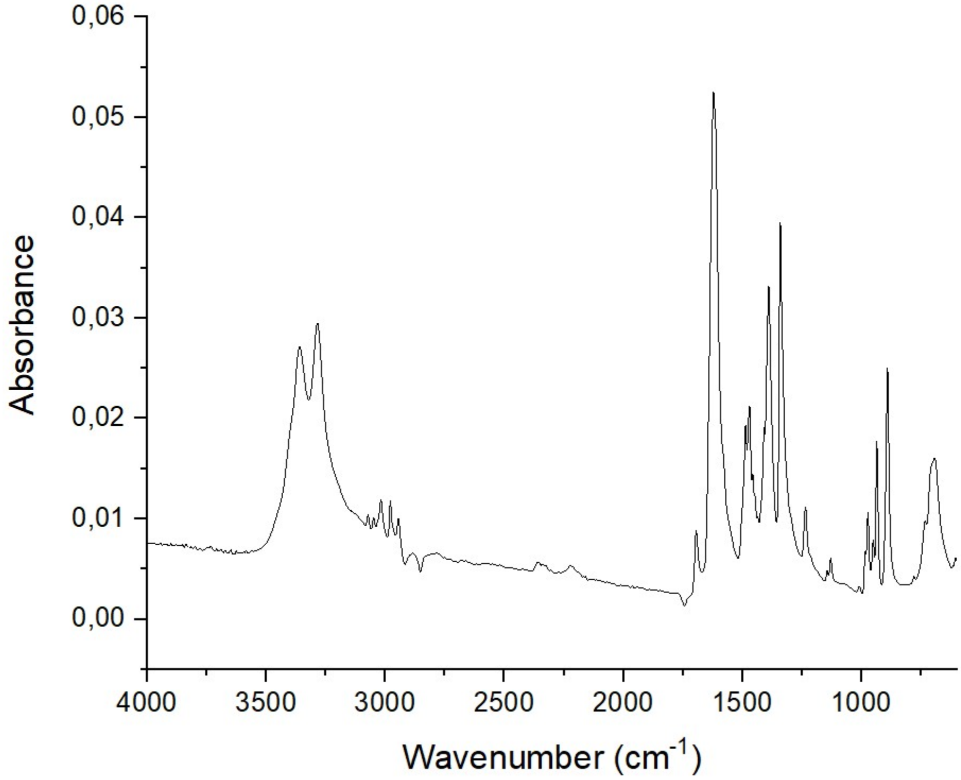

Figure S30. ATR-FTIR spectrum of betaine.

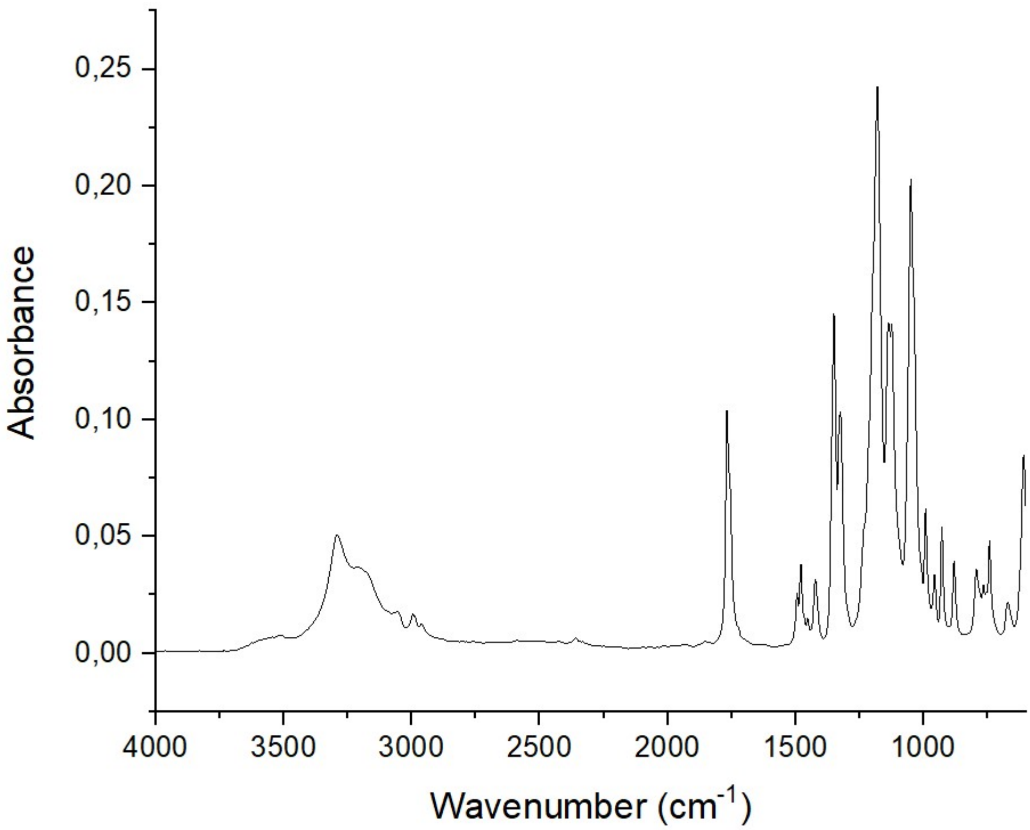

Figure S31. ATR-FTIR spectrum of H[Bet][Tf_2N].

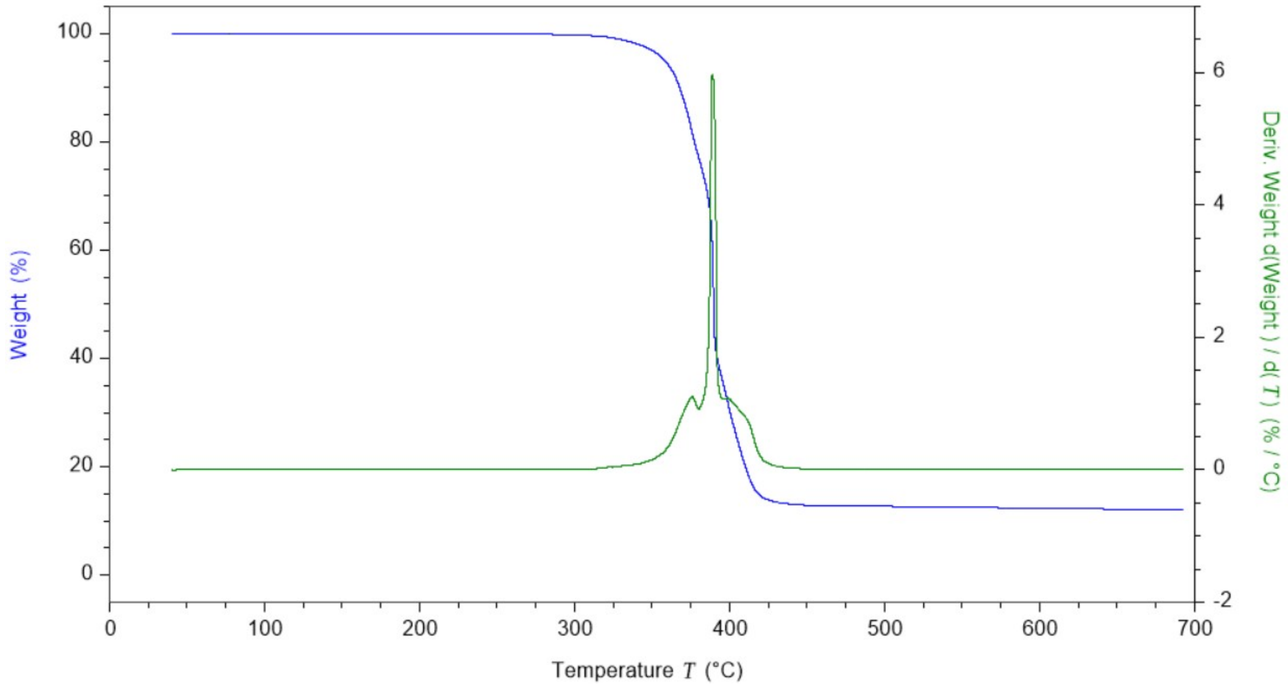

Figure S32. Thermogravimetric analysis of Mg[Bet]$_2$[Tf_2N]$_2$.

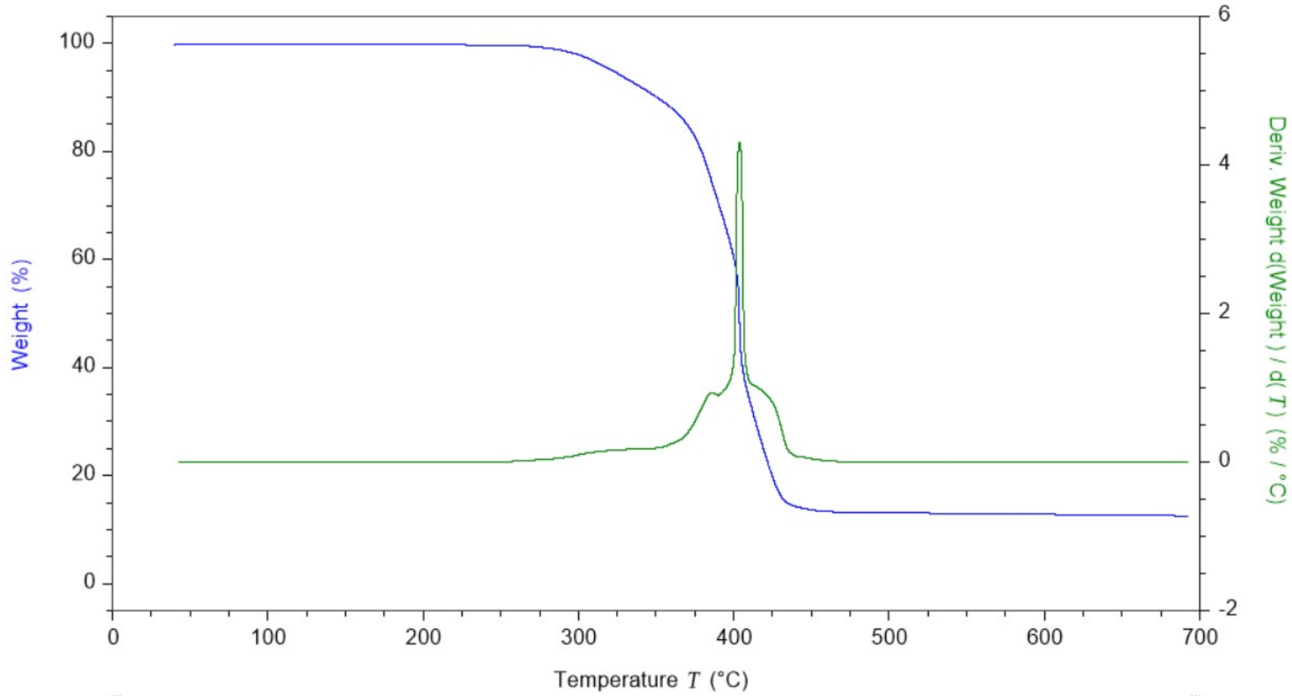

Figure S33. TGA thermogram of Mg[Bet]$_3$[Tf_2N]$_2$.

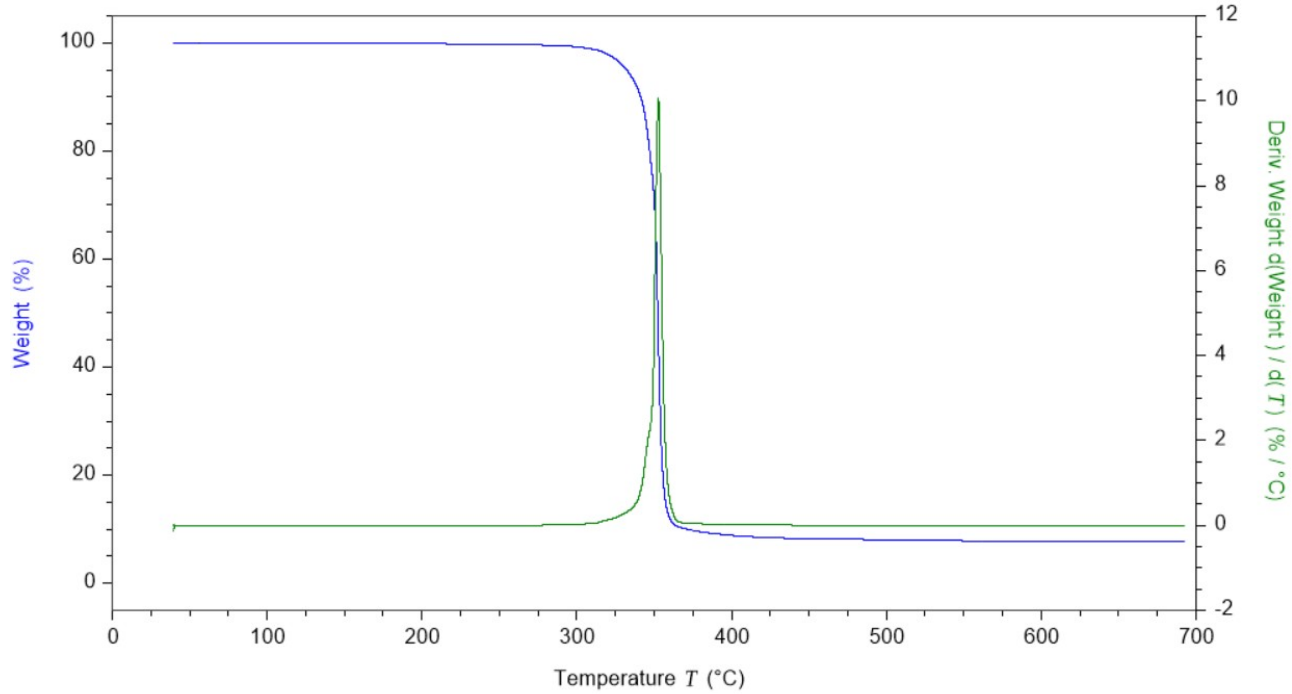

Figure S34. Thermogravimetric analysis of $Mg[Tf_2N]_2$.

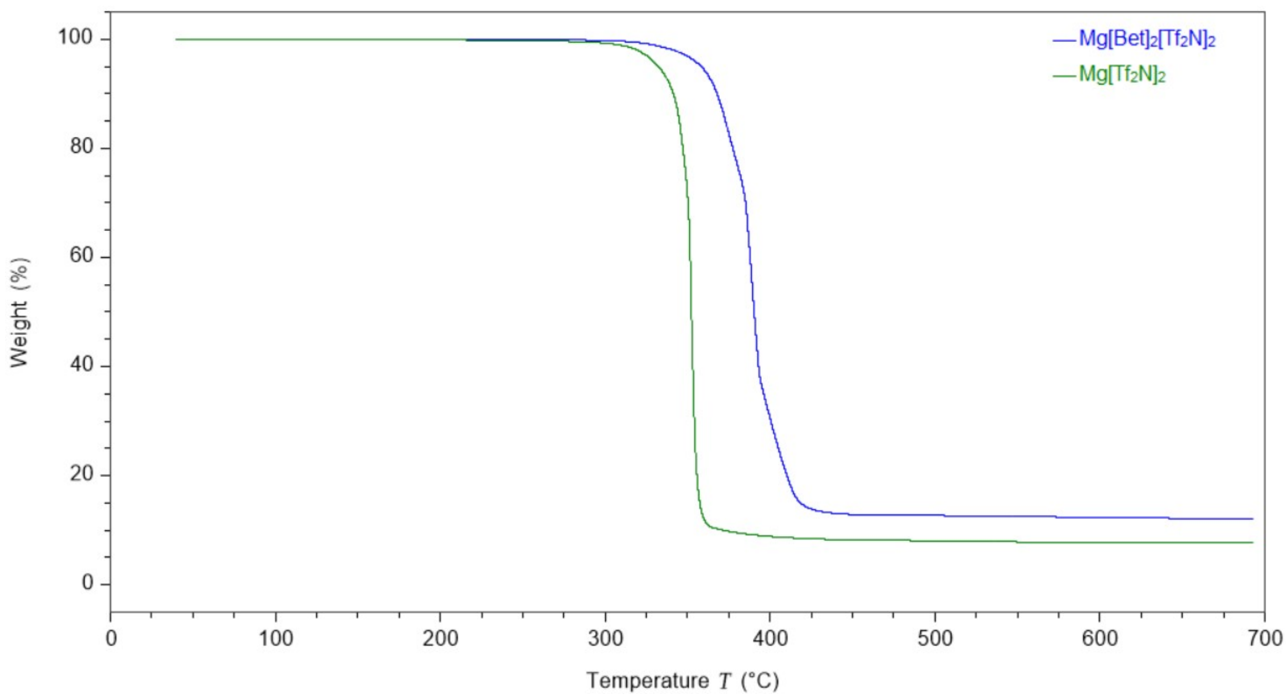

Figure S35. Comparison of thermogravimetric analysis of $Mg[Bet]_2[Tf_2N]_2$ and $Mg[Tf_2N]_2$.

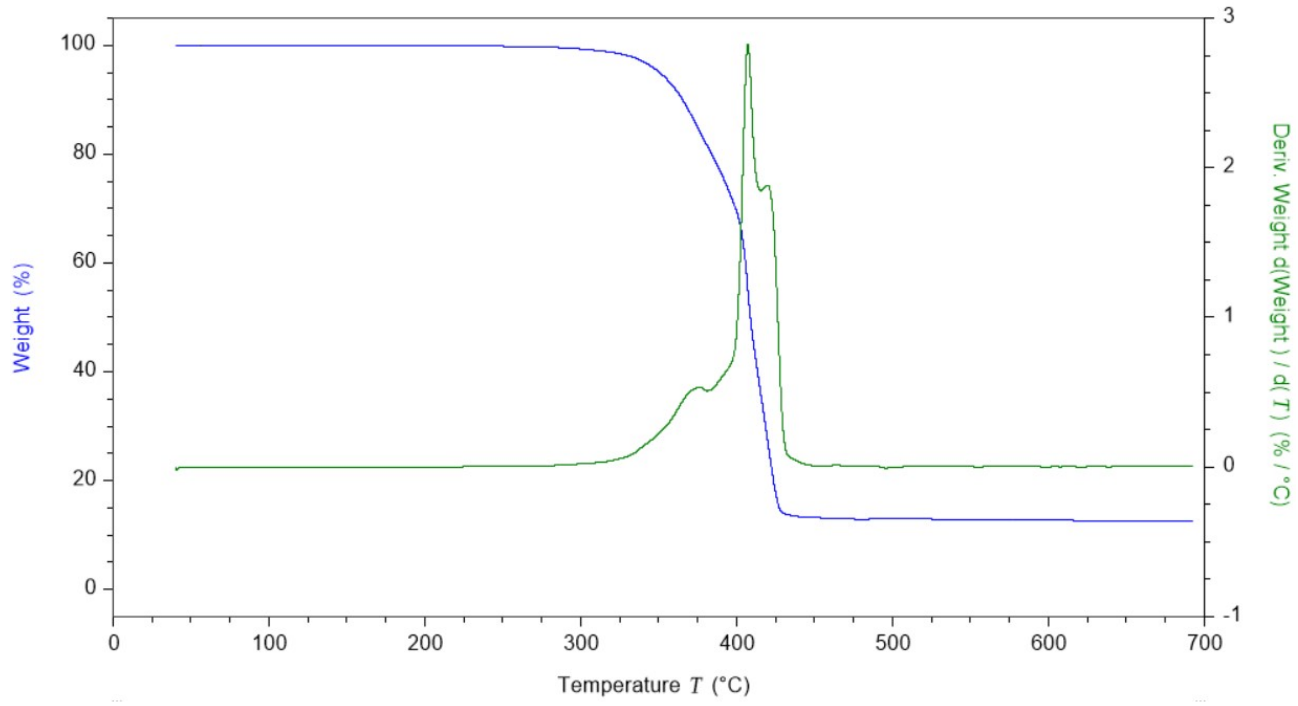

Figure S36. Thermogravimetric analysis of $Ca[Bet]_2[Tf_2N]_2$.

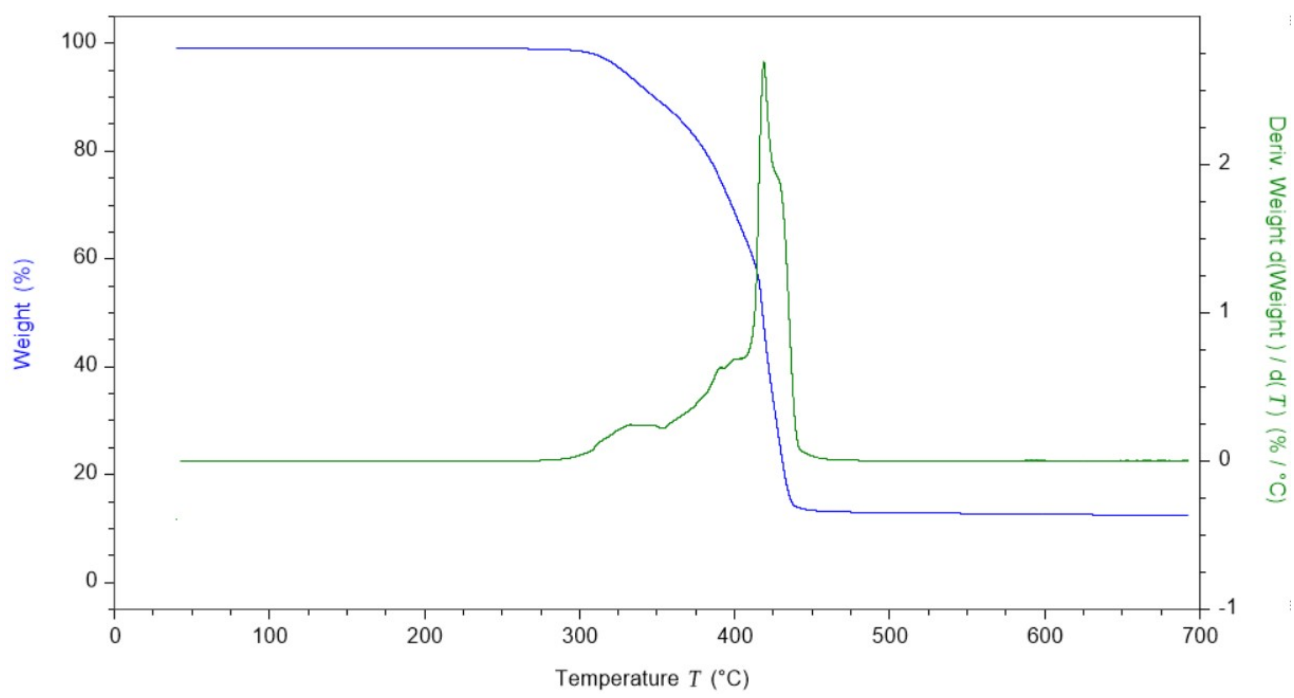

Figure S37. TGA thermogram of $Ca[Bet]_3[Tf_2N]_2$ (synthesized).

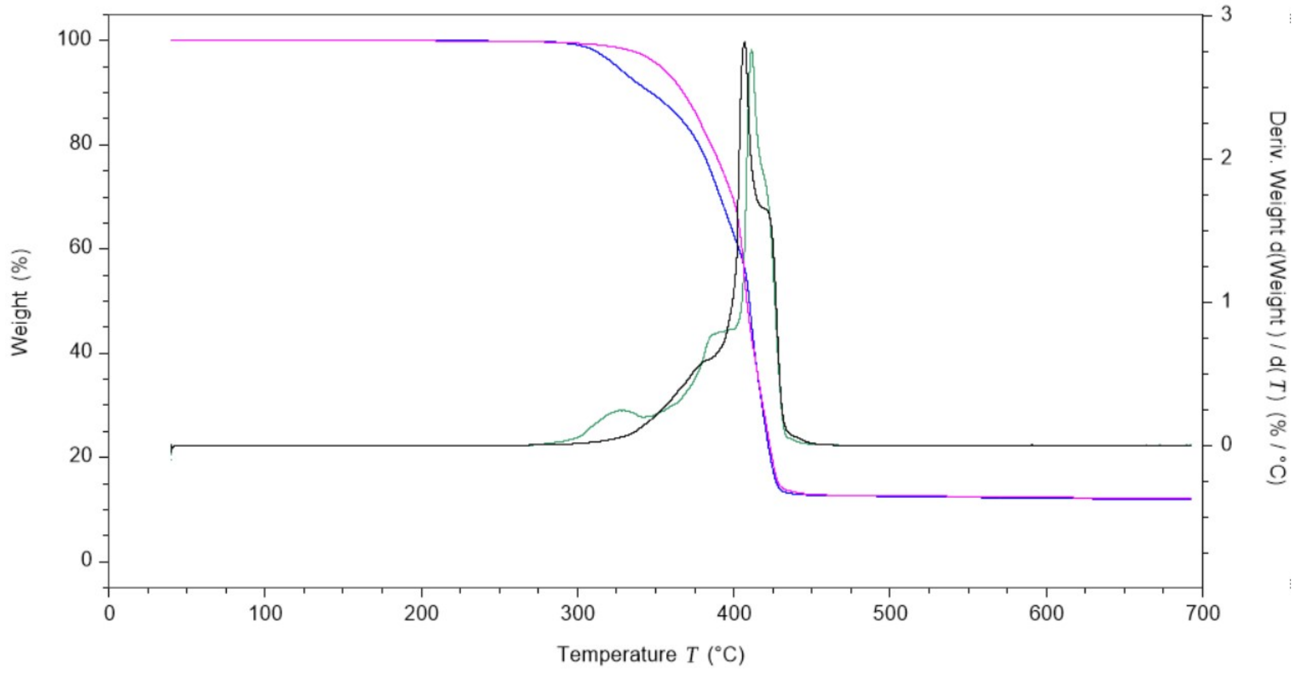

Figure S38. Thermogravimetric analysis of $Ca[Bet]_3[Tf_2N]_2$ crystals (blue and green curves) compared with the thermogravimetric analysis of $Ca[Bet]_2[Tf_2N]_2$ (violet and black curves) .

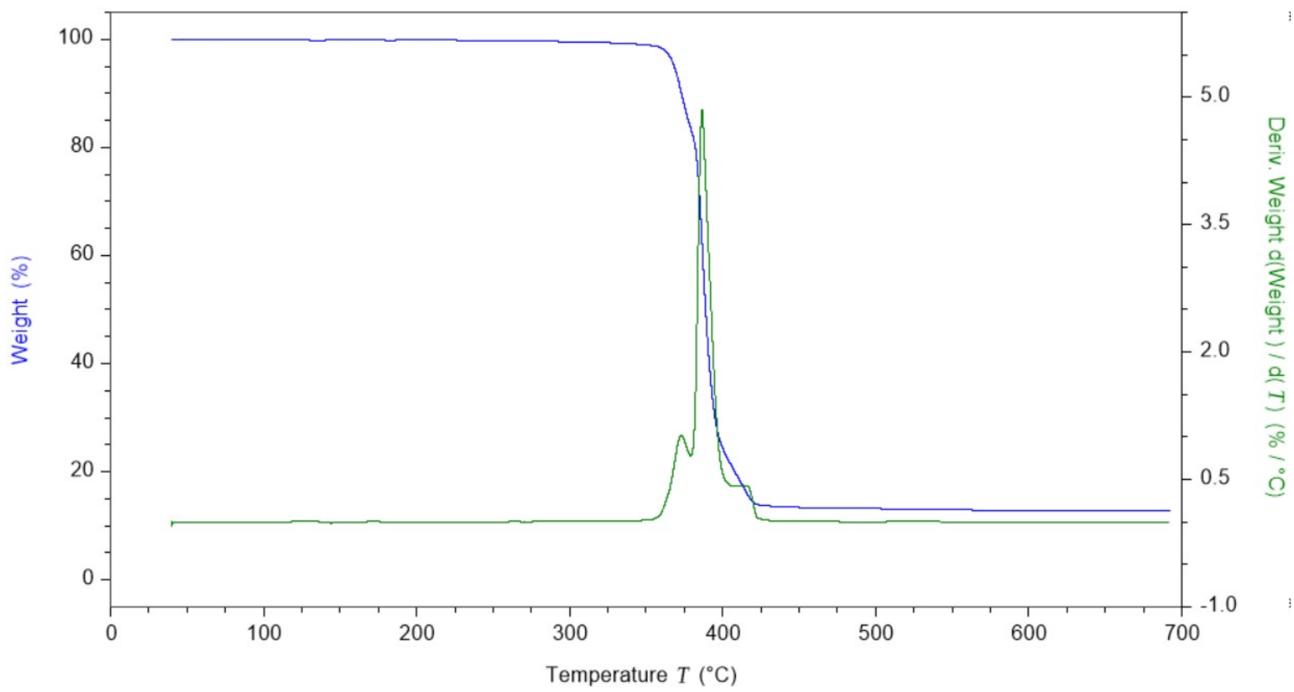

Figure S39. Thermogravimetric analysis of $Ca[Tf_2N]_2$.

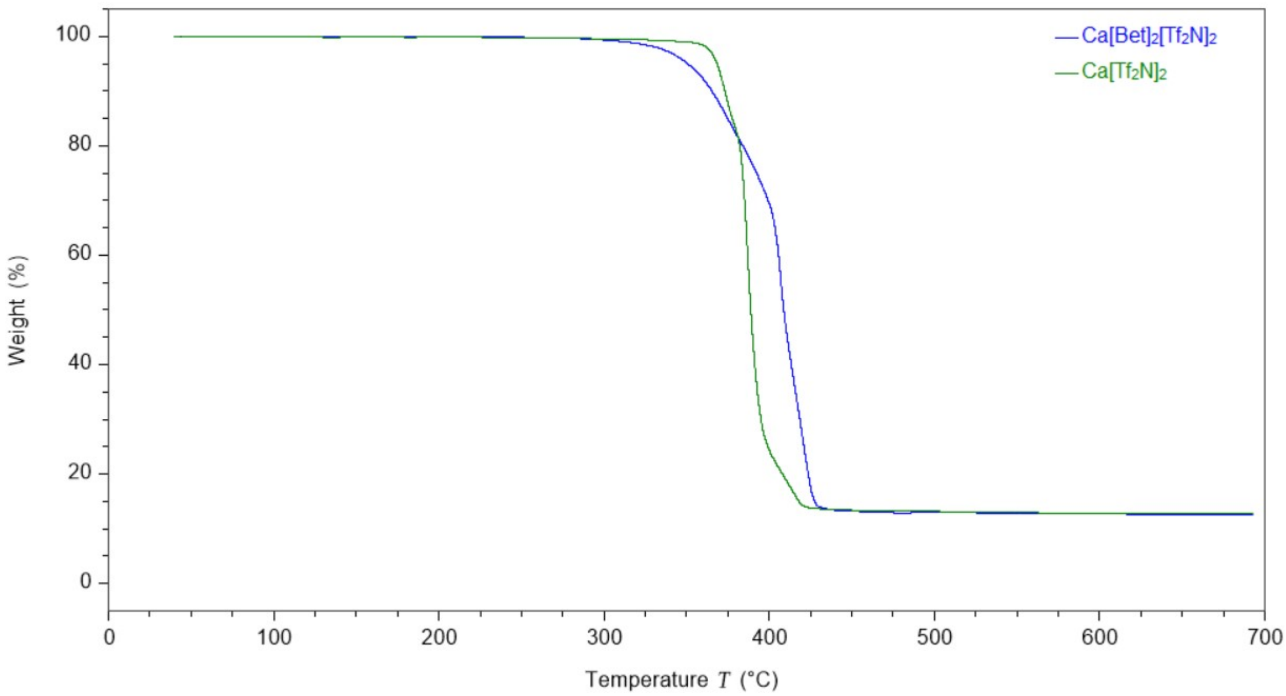

Figure S40. Comparison of thermogravimetric analysis of $Mg[Bet]_2[Tf_2N]_2$ and $Mg[Tf_2N]_2$.

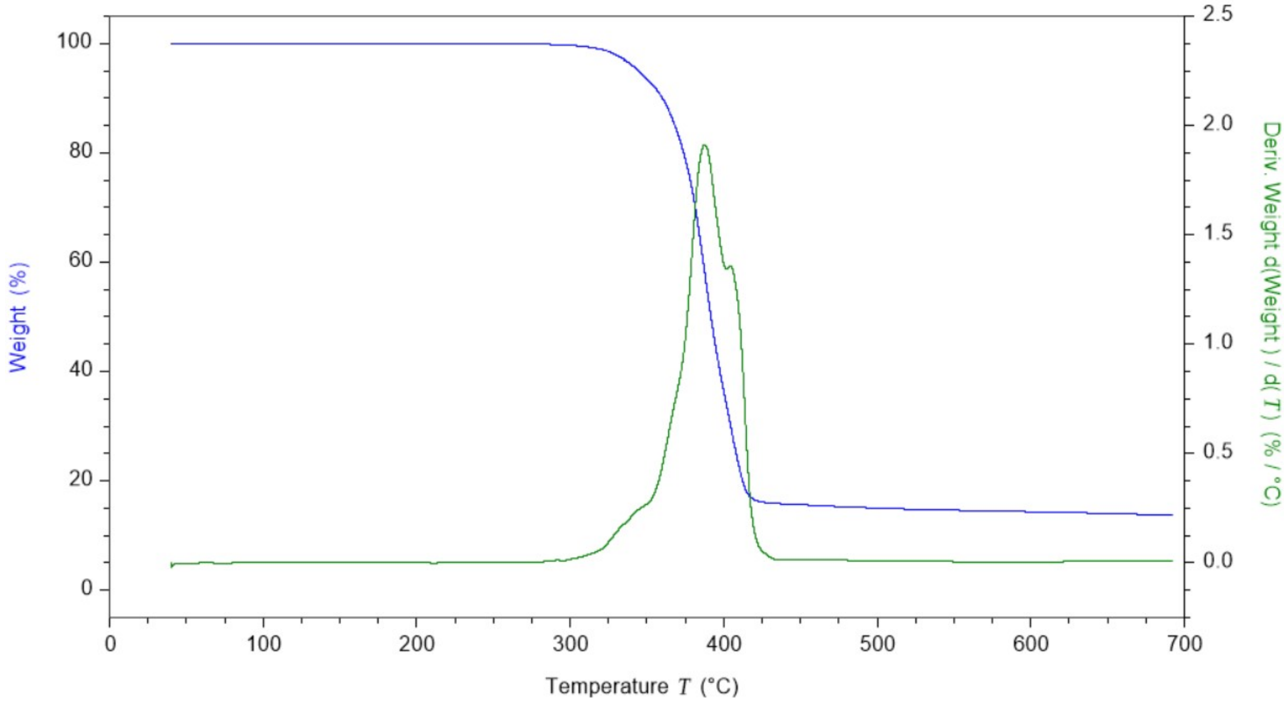

Figure S41. Thermogravimetric analysis of $Zn[Bet]_2[Tf_2N]_2$.

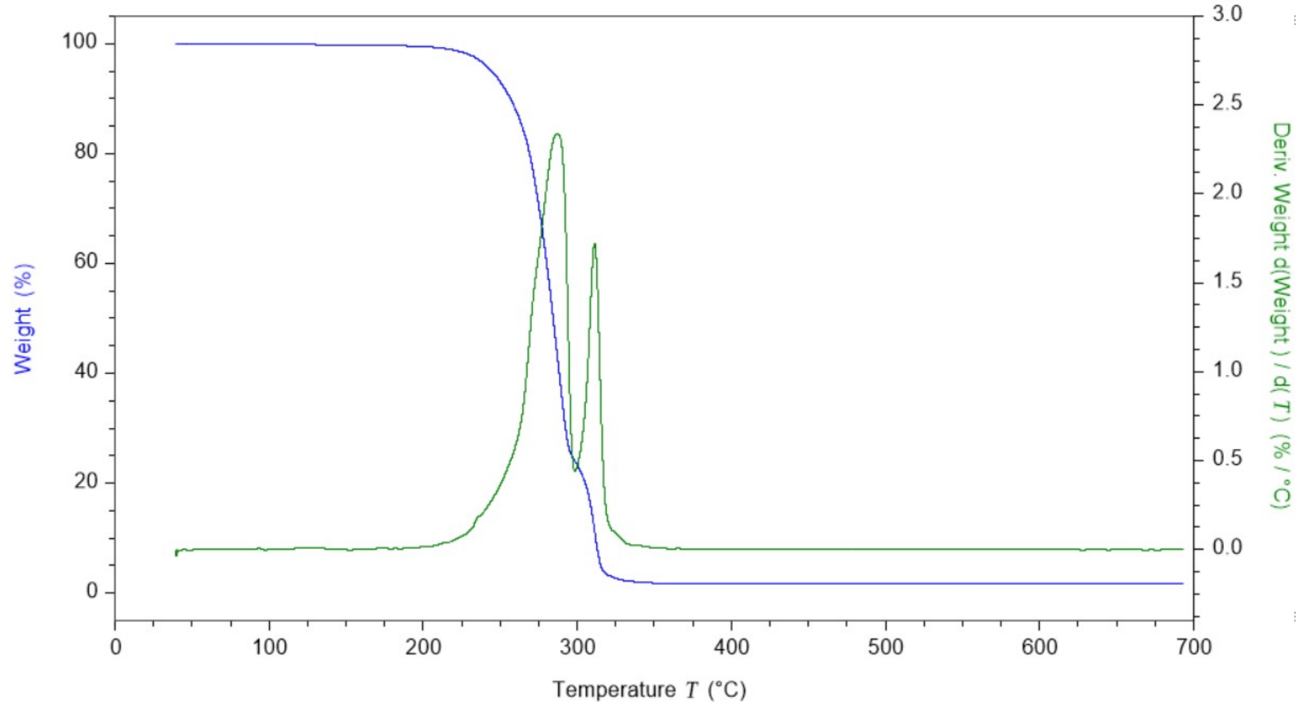

Figure S42. Thermogravimetric analysis of $Zn[Tf_2N]_2$.

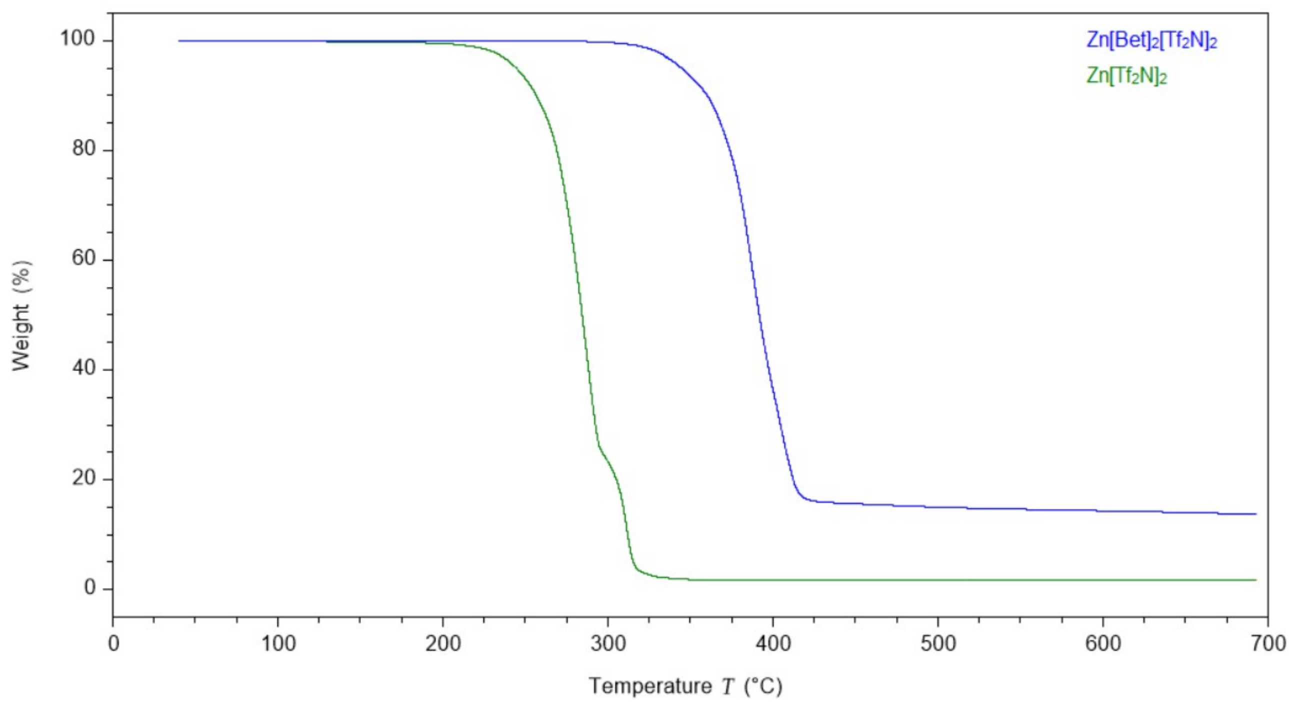

Figure S43. Comparison of thermogravimetric analysis of $Zn[Bet]_2[Tf_2N]_2$ and $Zn[Tf_2N]_2$.

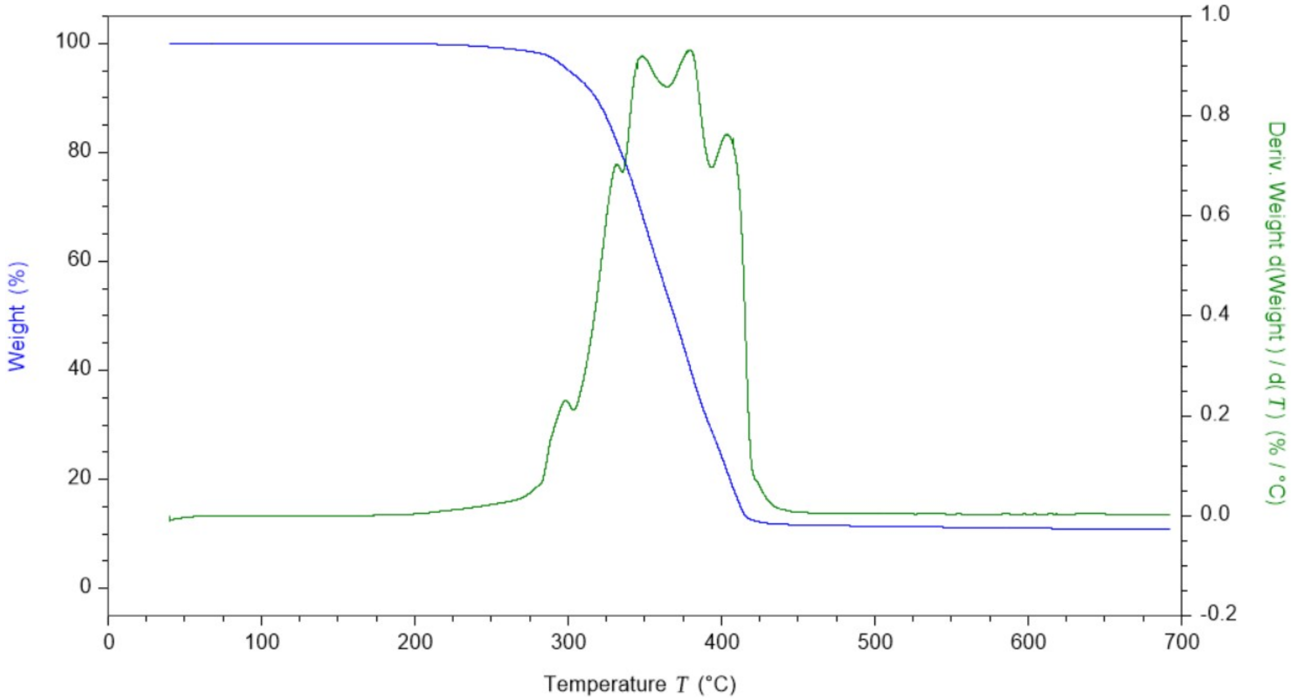

Figure S44. Thermogravimetric analysis of Cu[Bet]$_2$[Tf$_2$N]$_2$.

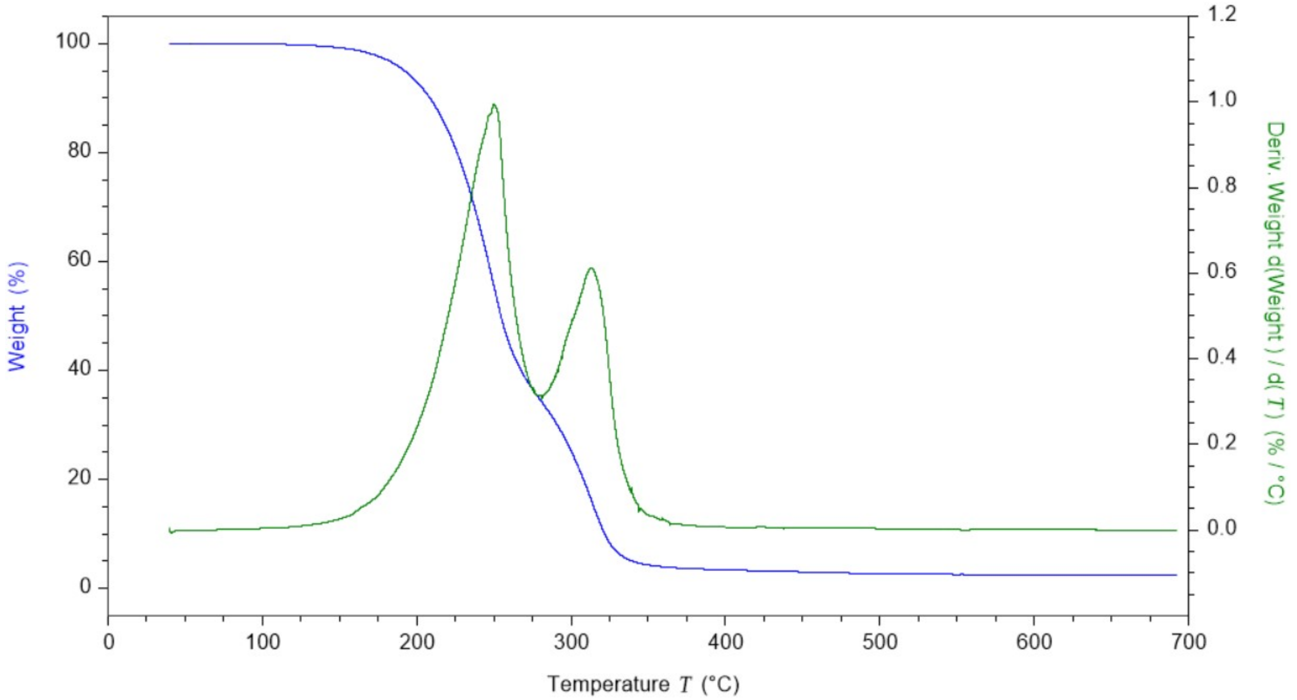

Figure S45. Thermogravimetric analysis of Cu[Tf$_2$N]$_2$.

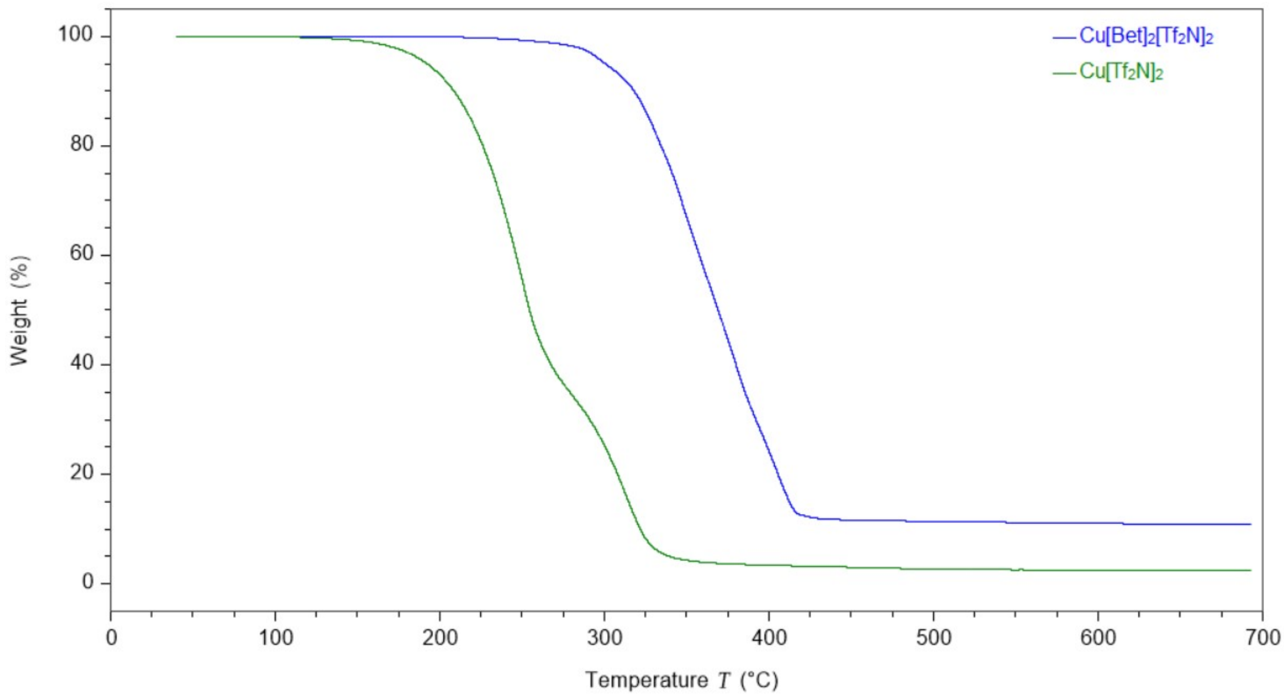

Figure S46. Comparison of thermogravimetric analysis of $Cu[Bet]_2[Tf_2N]_2$ and $Cu[Tf_2N]_2$.

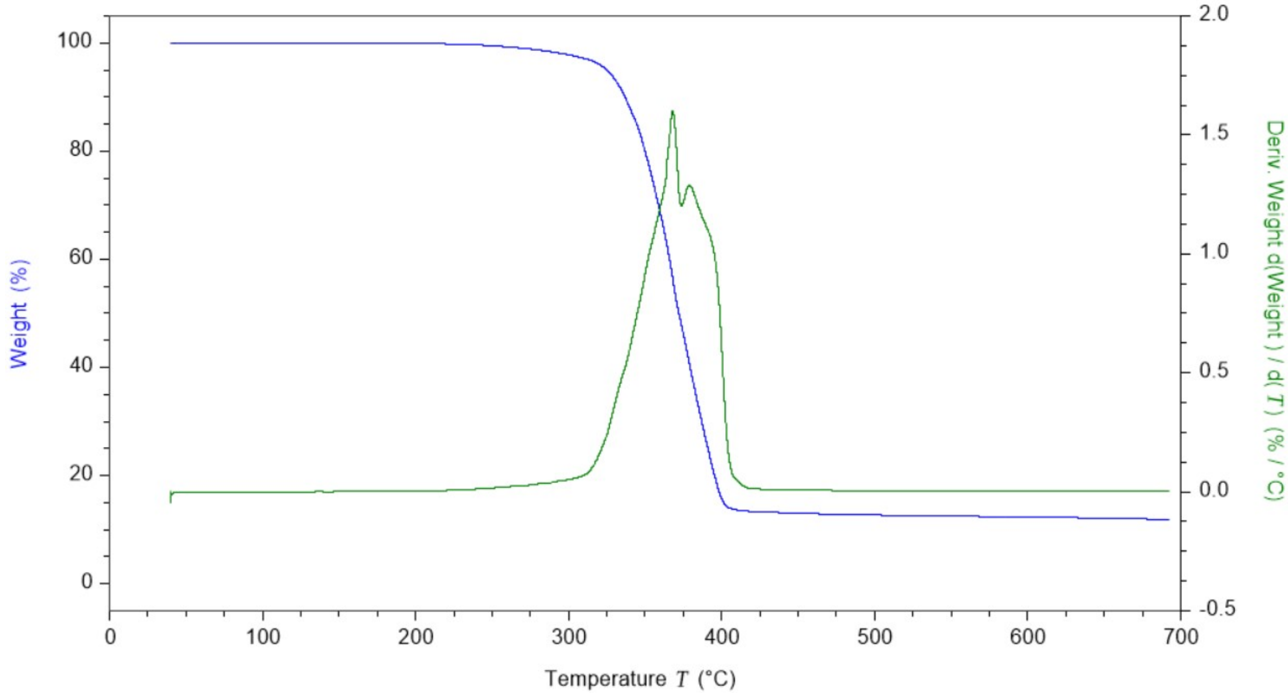

Figure S47. Thermogravimetric analysis of $Ni[Bet]_2[Tf_2N]_2$.

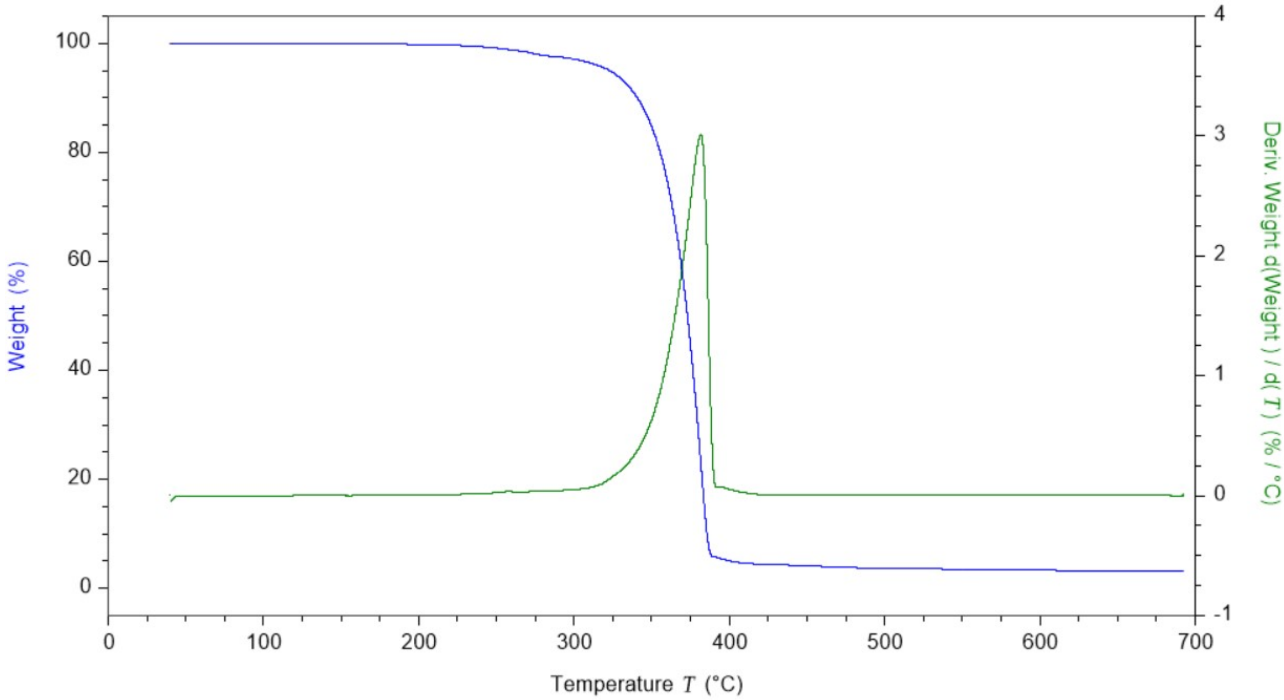

Figure S48. Thermogravimetric analysis of $Ni[Tf_2N]_2$.

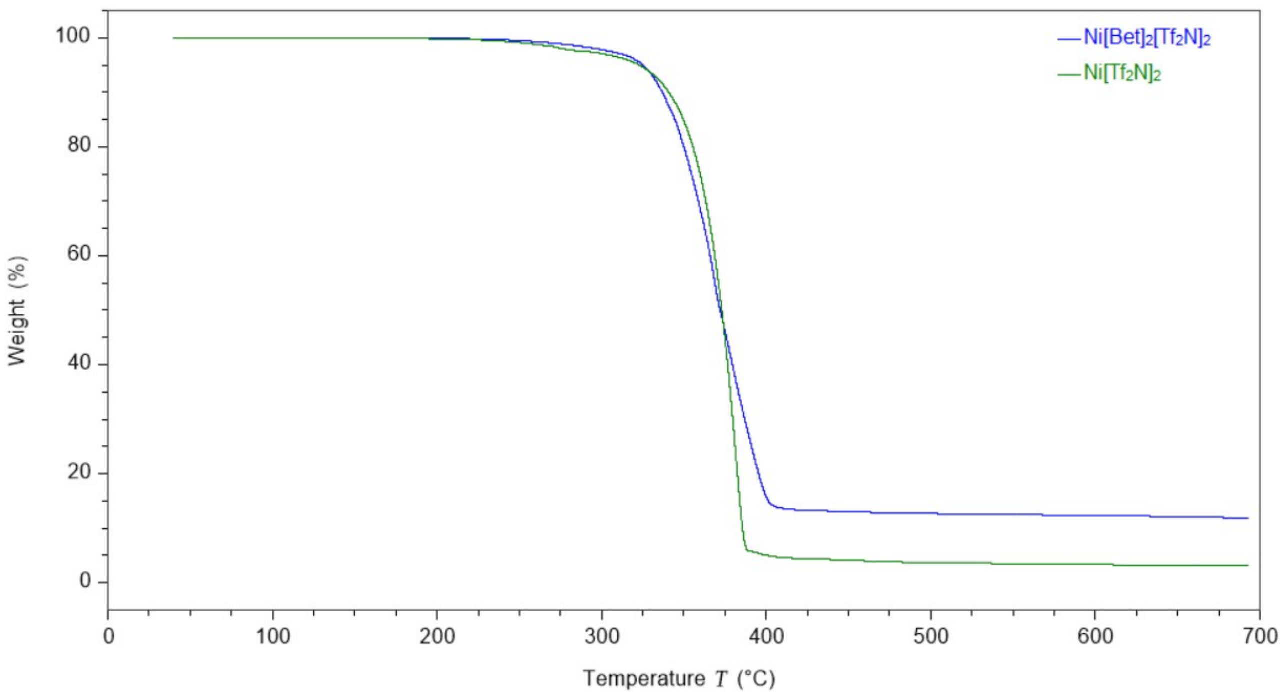

Figure S49. Comparison of thermogravimetric analysis of $Ni[Bet]_2[Tf_2N]_2$ and $Ni[Tf_2N]_2$.

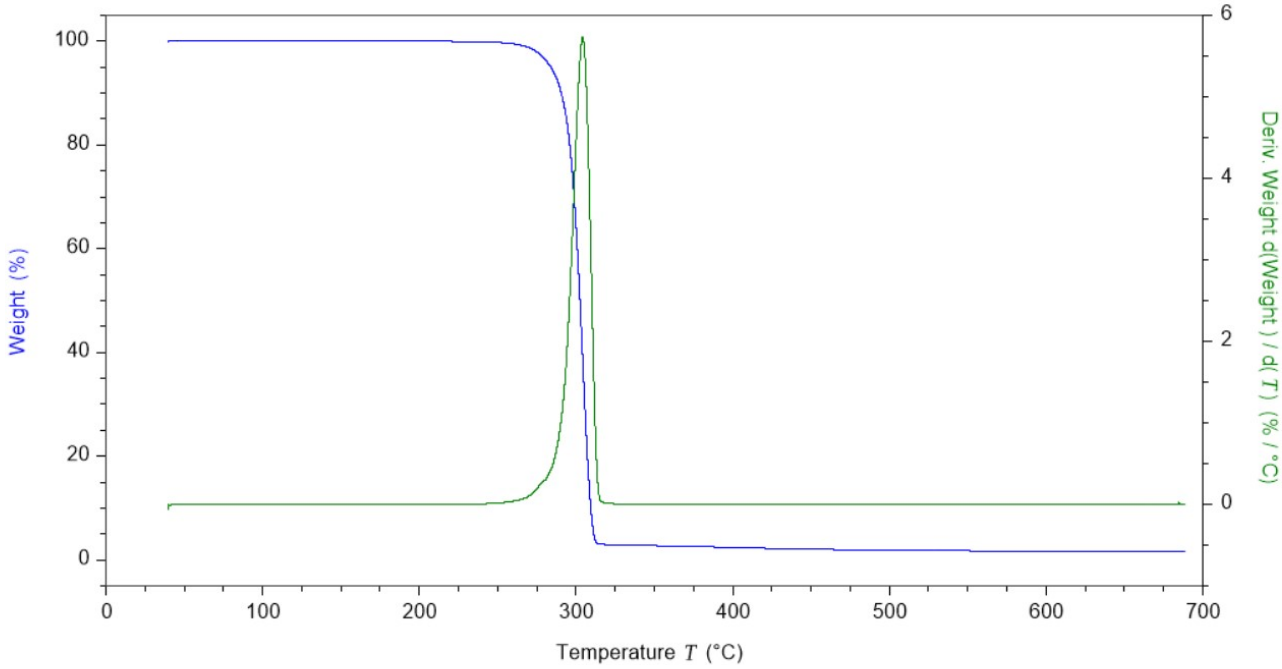

Figure S50. Thermogravimetric analysis of betaine.

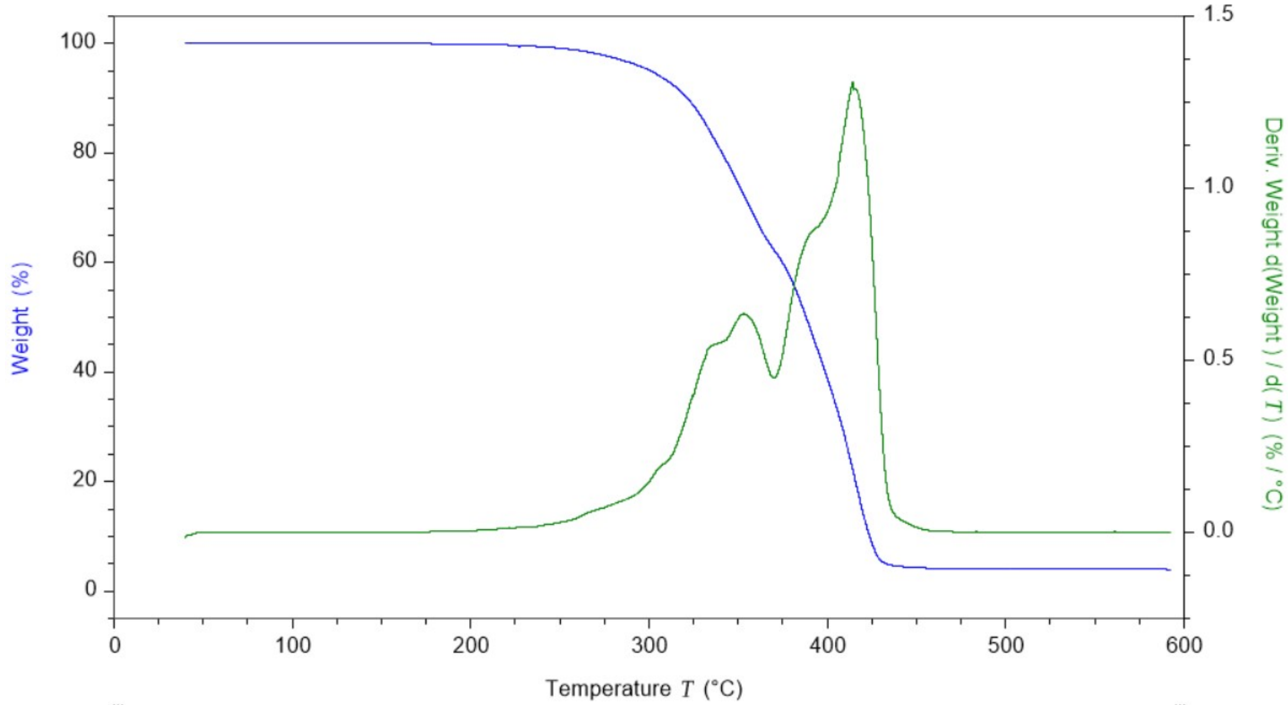

Figure S51. Thermogravimetric analysis of H[Bet][Tf_2N].

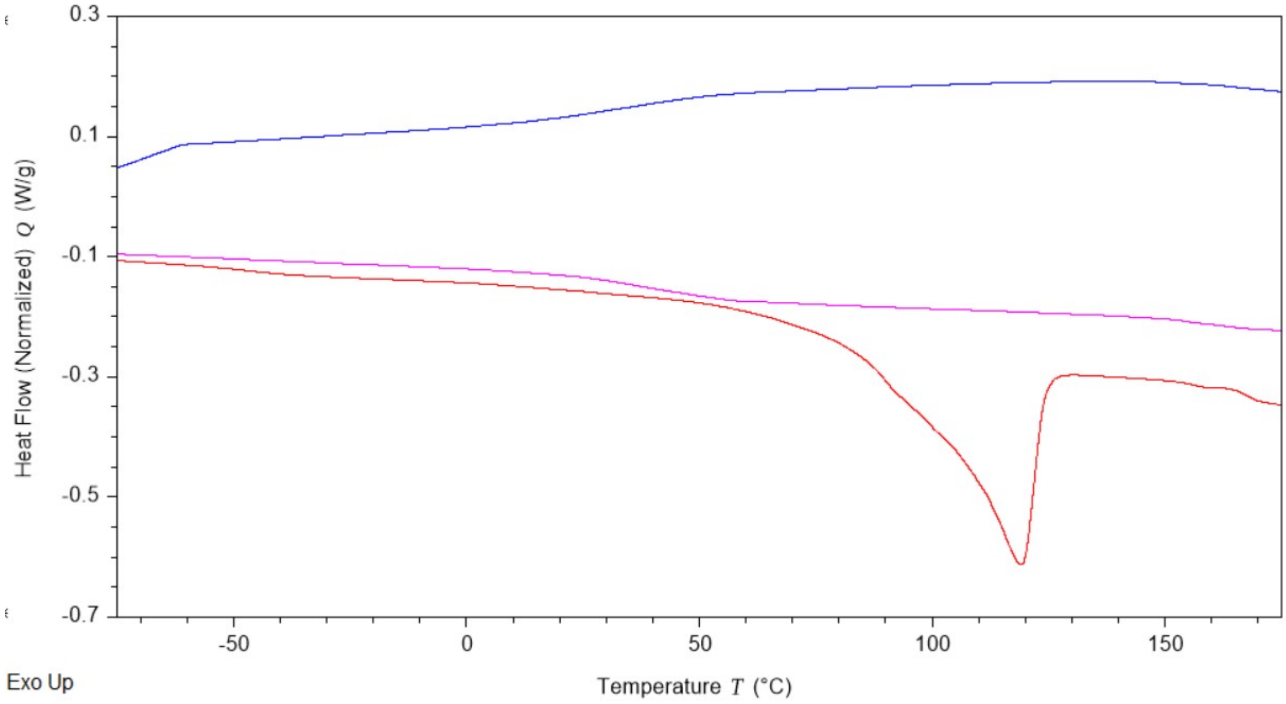

Figure S52. Differential scanning calorimetry of $Mg[Bet]_2[Tf_2N]_2$.

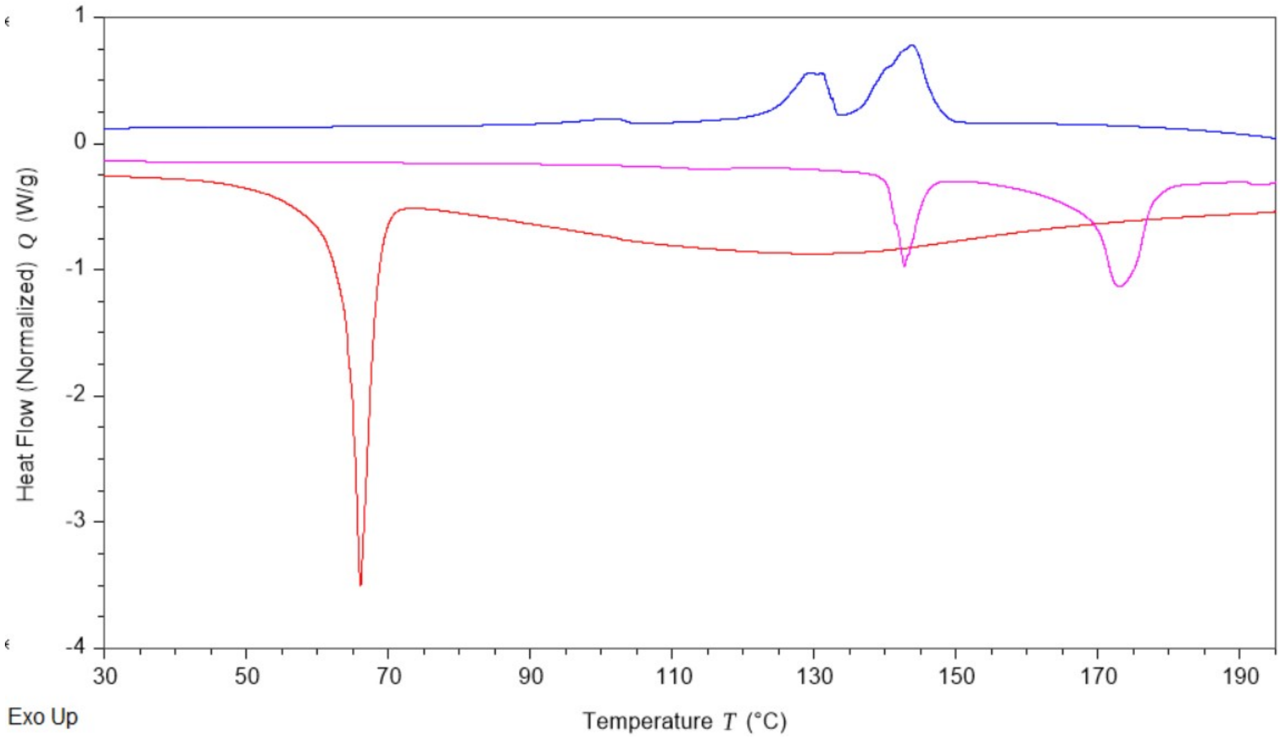

Figure S53. Differential scanning calorimetry of $Mg[Tf_2N]_2$.

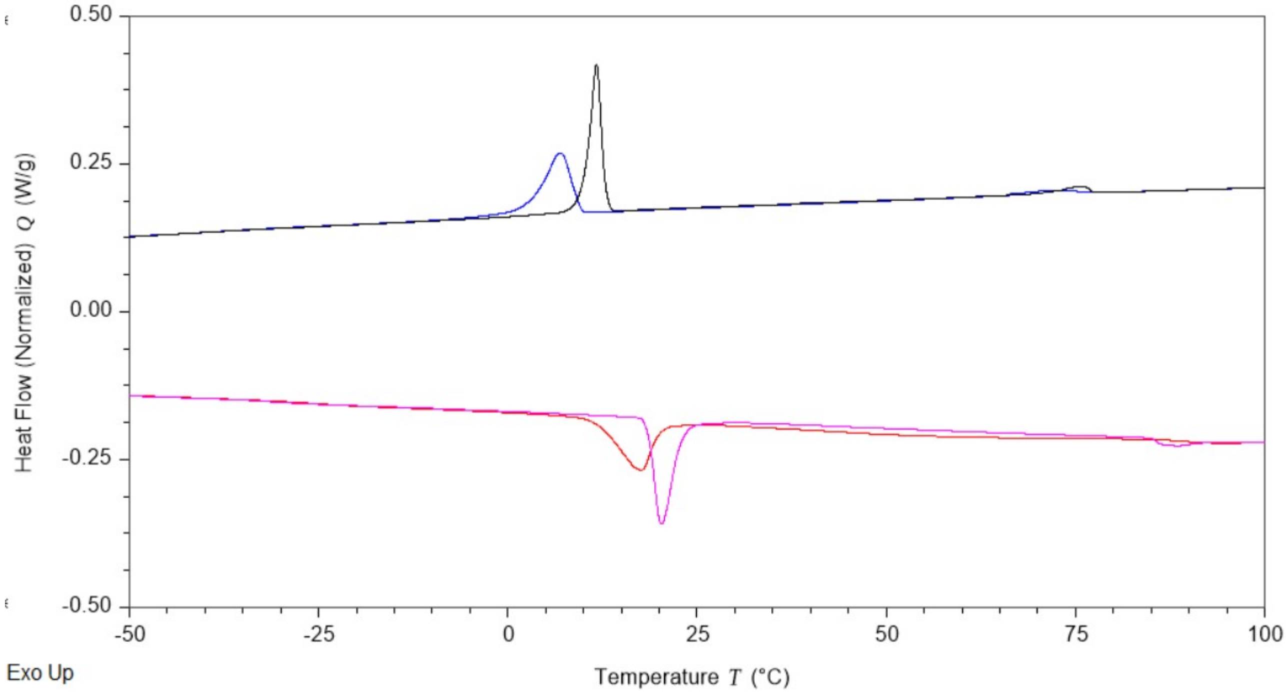

Figure S54a. DSC thermogram of $Mg[Bet]_3[Tf_2N]_2$.

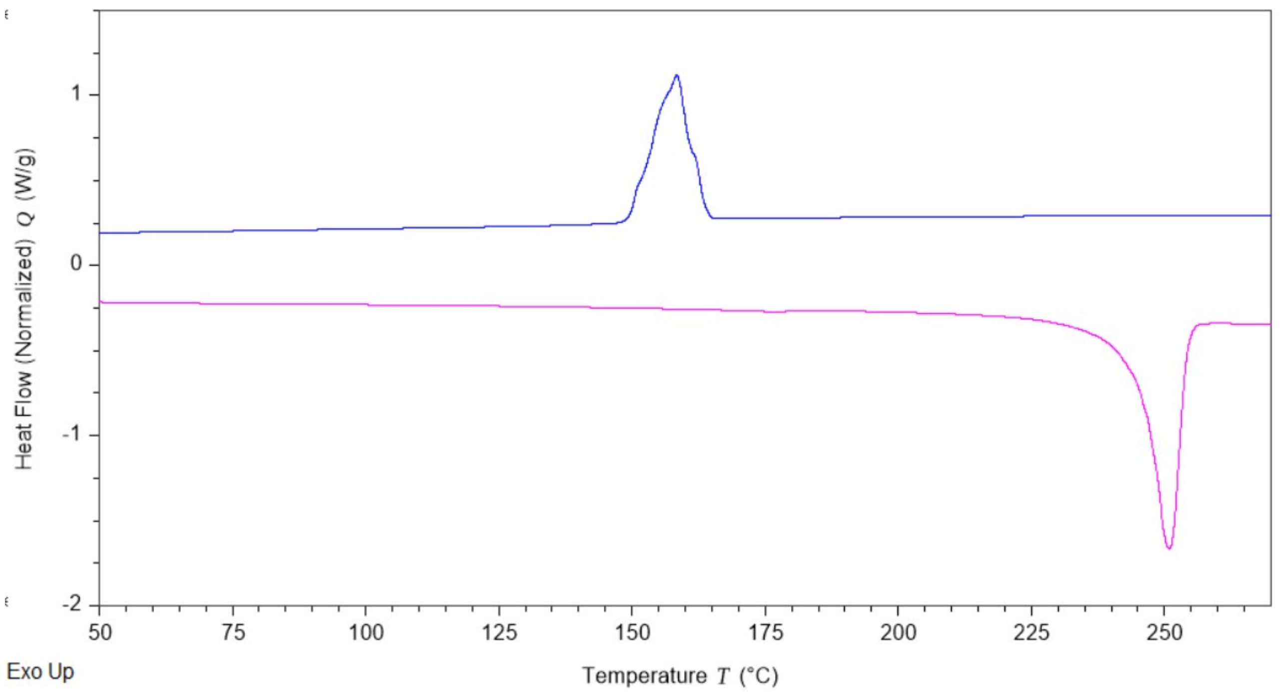

Figure S54b. DSC thermogram of $Mg[Bet]_3[Tf_2N]_2$, ramp to 280 °C.

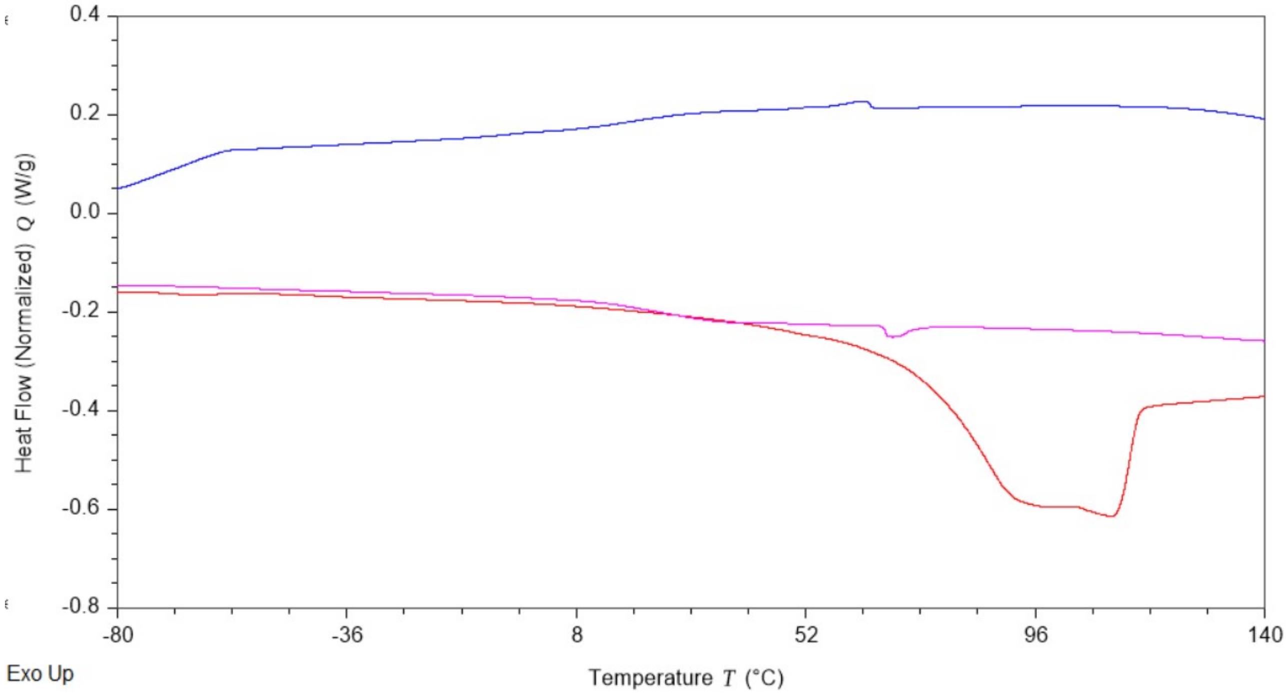

Figure S55. Differential scanning calorimetry of $Ca[Bet]_2[Tf_2N]_2$.

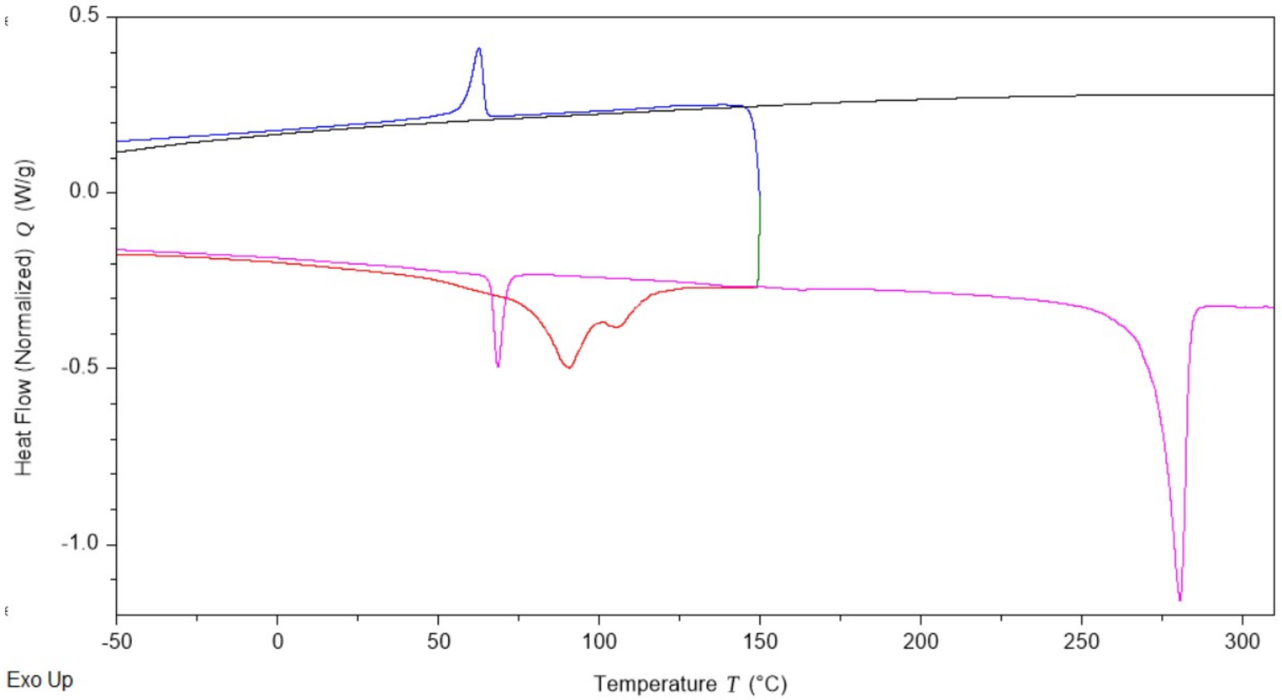

Figure S56a. Differential scanning calorimetry of $Ca[Bet]_3[Tf_2N]_2$ crystals.

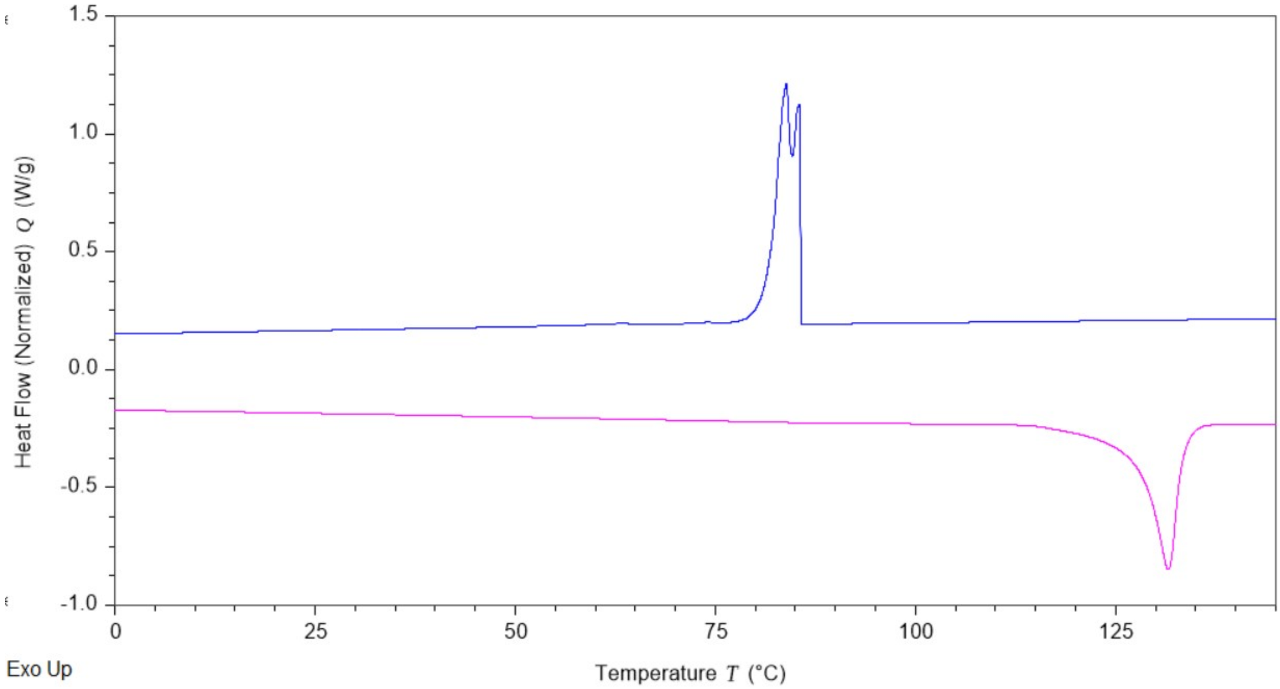

Figure S56b. Differential scanning calorimetry of $Ca[Bet]_3[Tf_2N]_2$ crystals after the melting transition at about 280 °C.

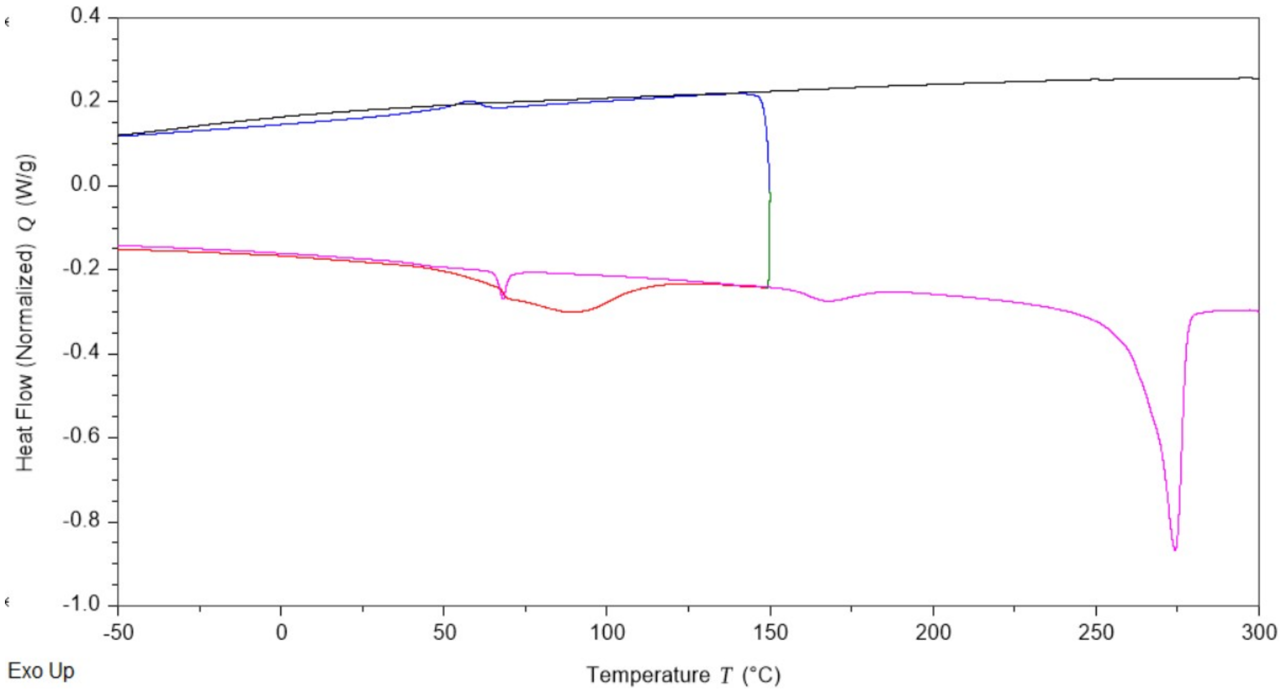

Figure S56c. DSC thermogram of $Ca[Bet]_3[Tf_2N]_2$ (synthetized).

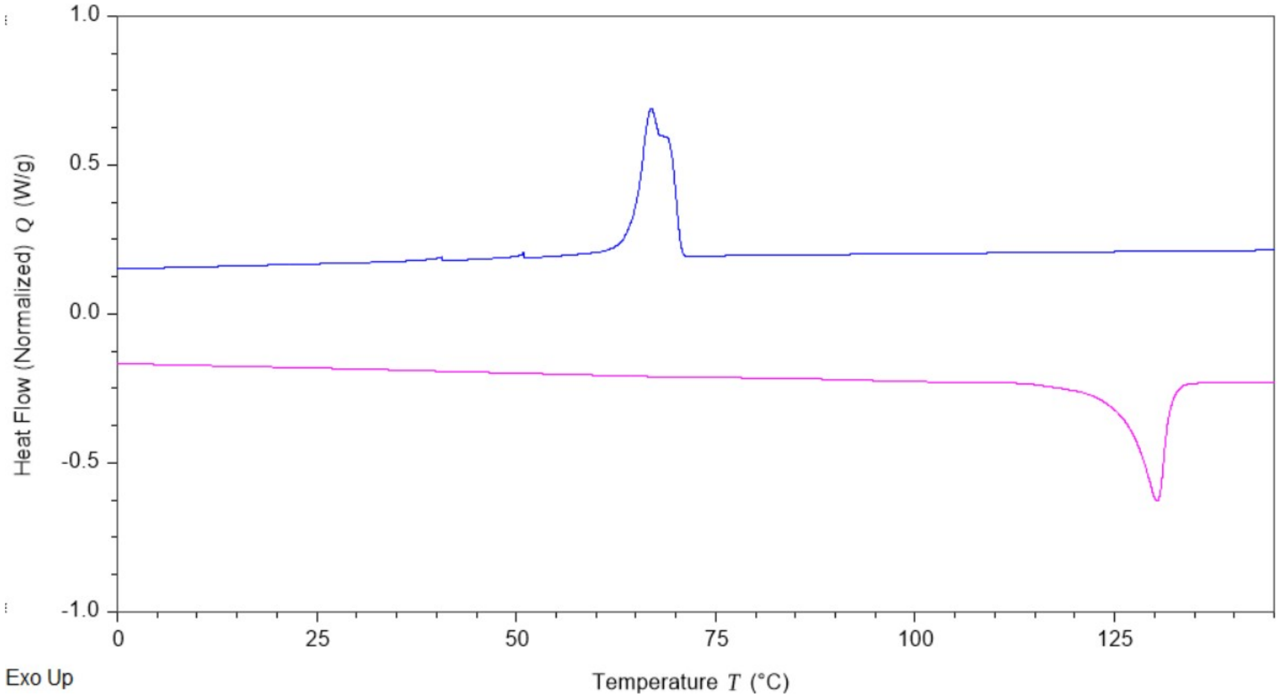

Figure S56d. DSC thermogram of Ca[Bet]$_3$[Tf$_2$N]$_2$ (synthetized).

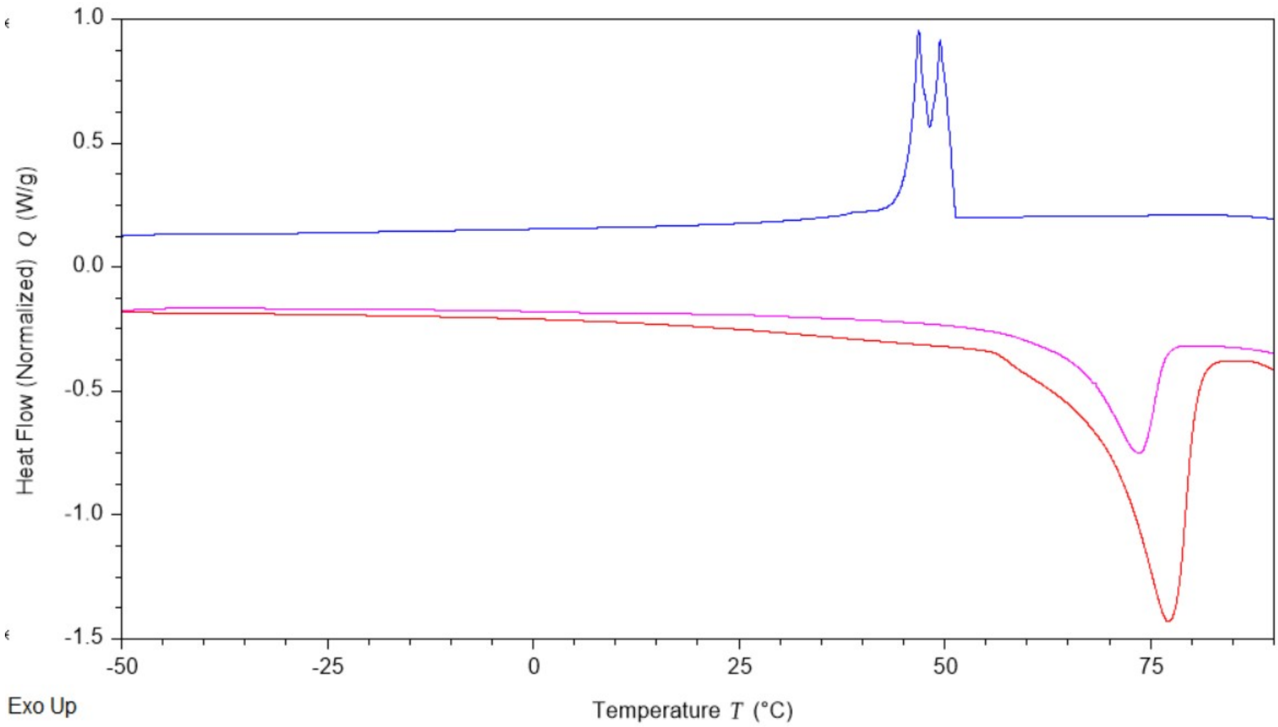

Figure S57a. Differential scanning calorimetry of Ca[Tf$_2$N]$_2$.

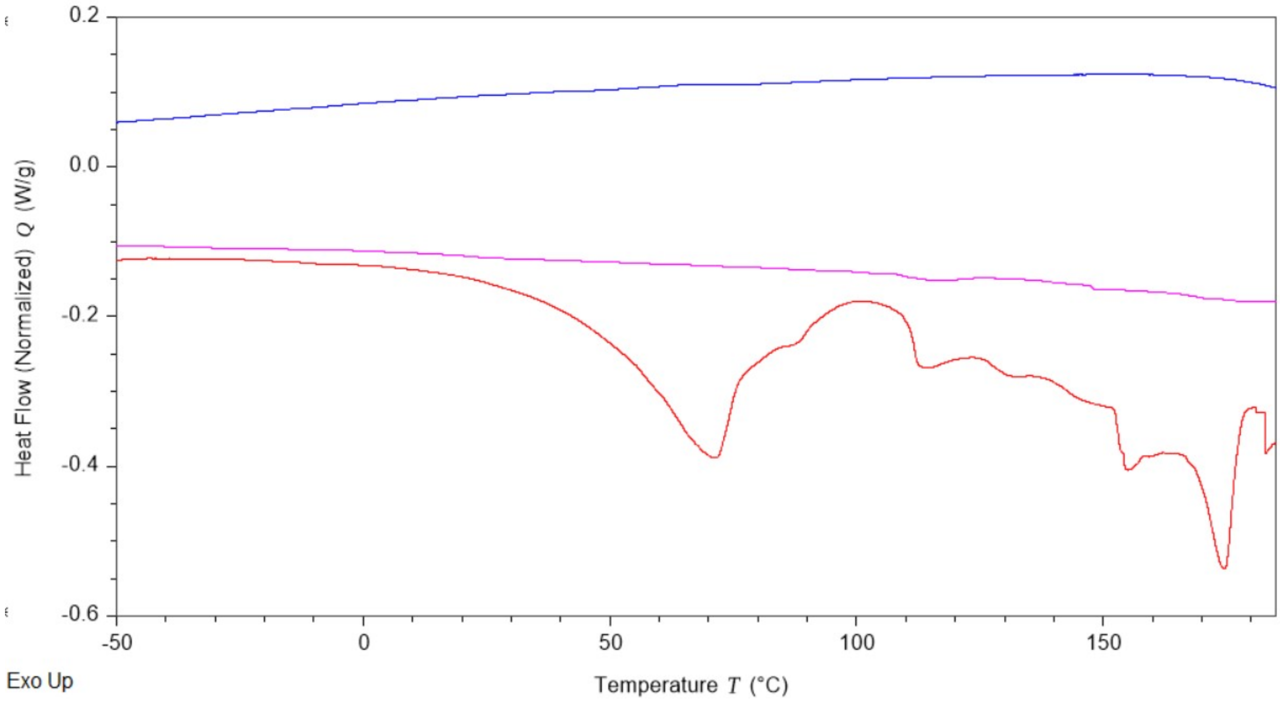

Figure S57b. Differential scanning calorimetry of $Ca[Tf_2N]_2$ above 100 °C.

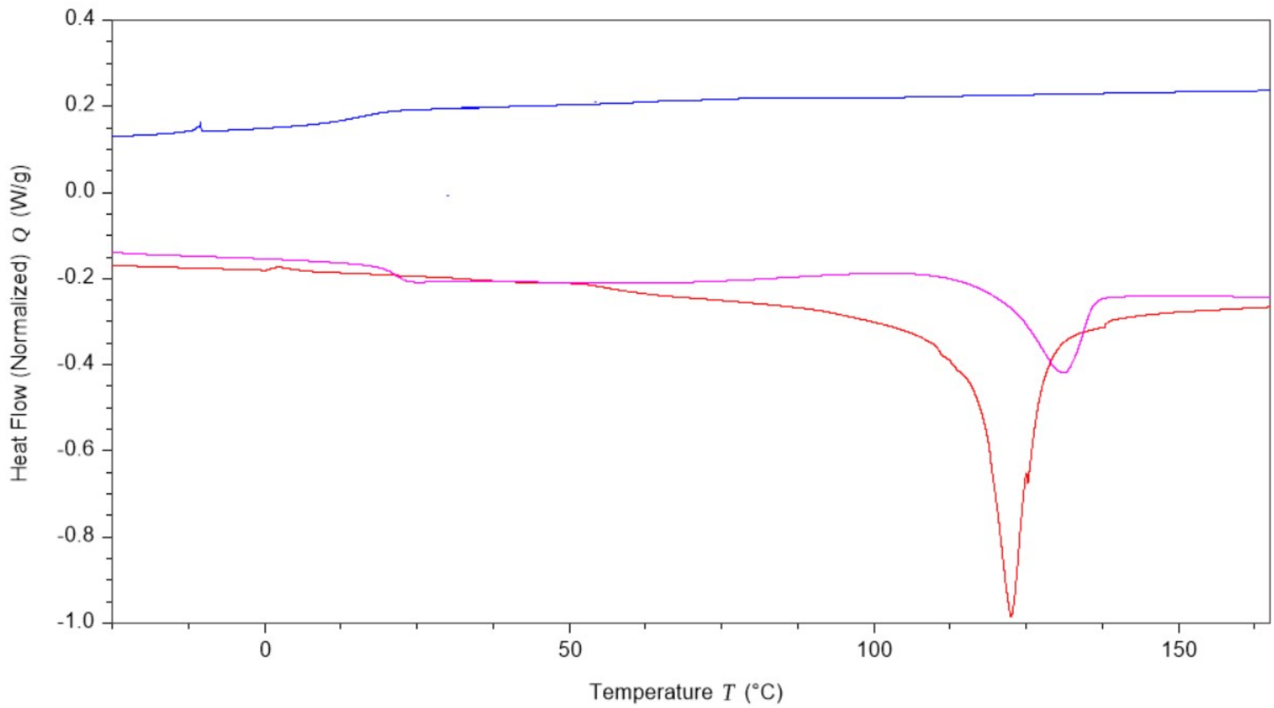

Figure S58a. Differential scanning calorimetry of $Zn[Bet]_2[Tf_2N]_2$.

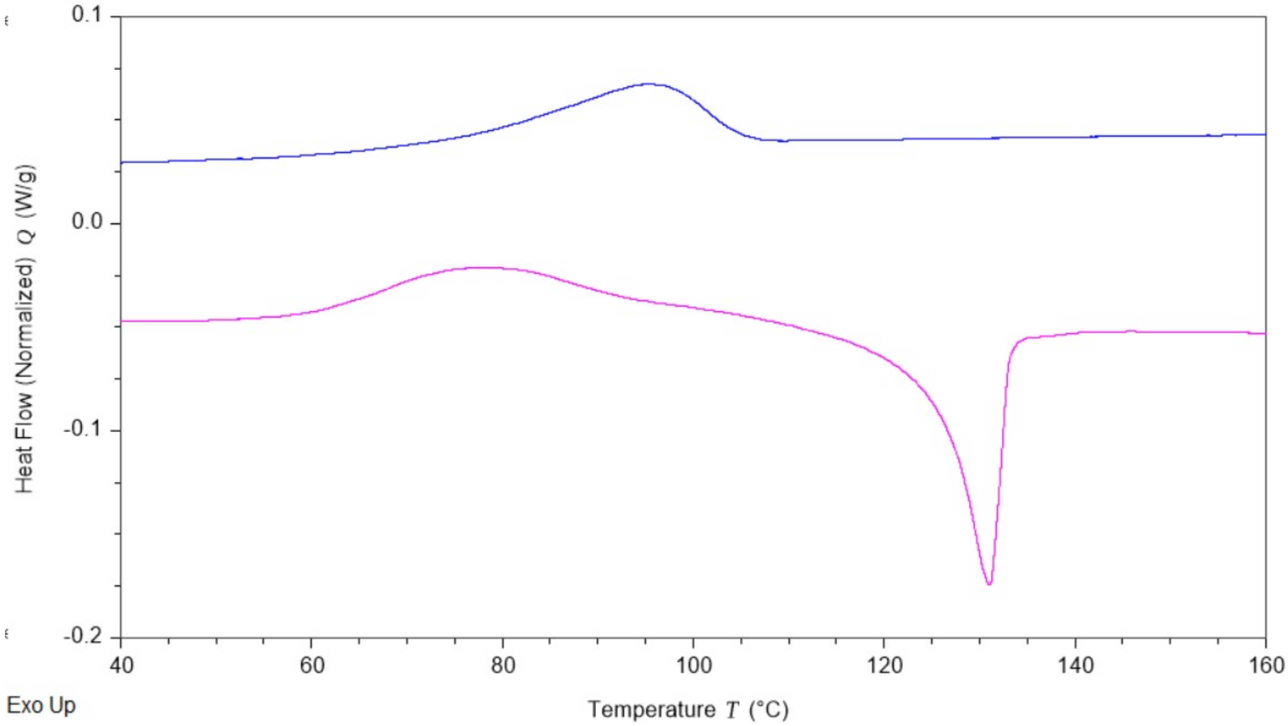

Figure S58b. Differential scanning calorimetry of $Zn[Bet]_2[Tf_2N]_2$, performed at 2 K/min

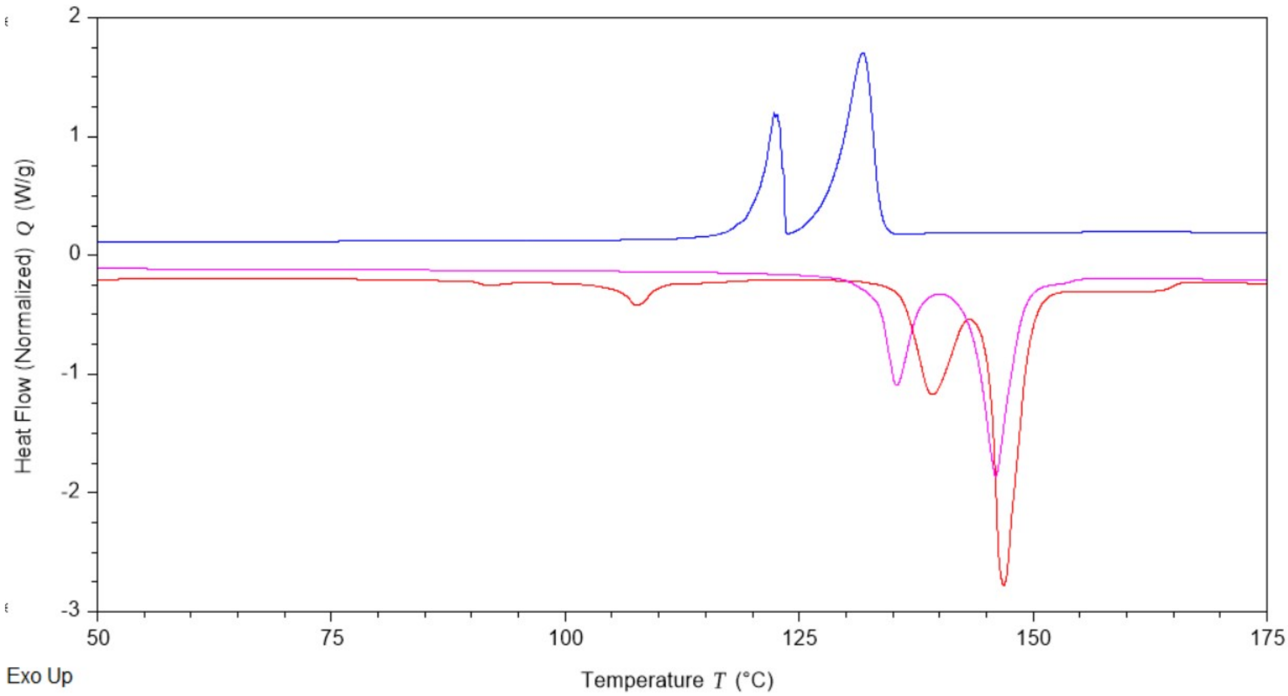

Figure S59. Differential scanning calorimetry of $Zn[Tf_2N]_2$.

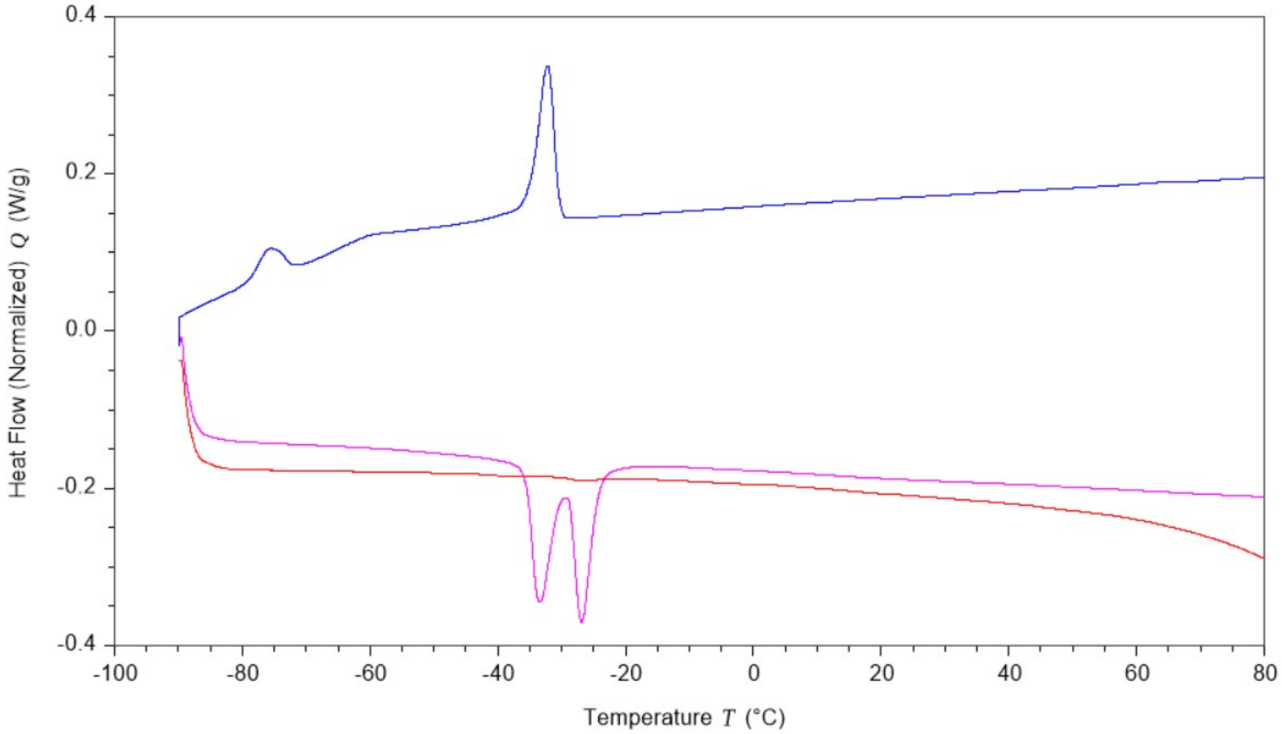

Figure S60a. Differential scanning calorimetry of $Cu[Bet]_2[Tf_2N]_2$.

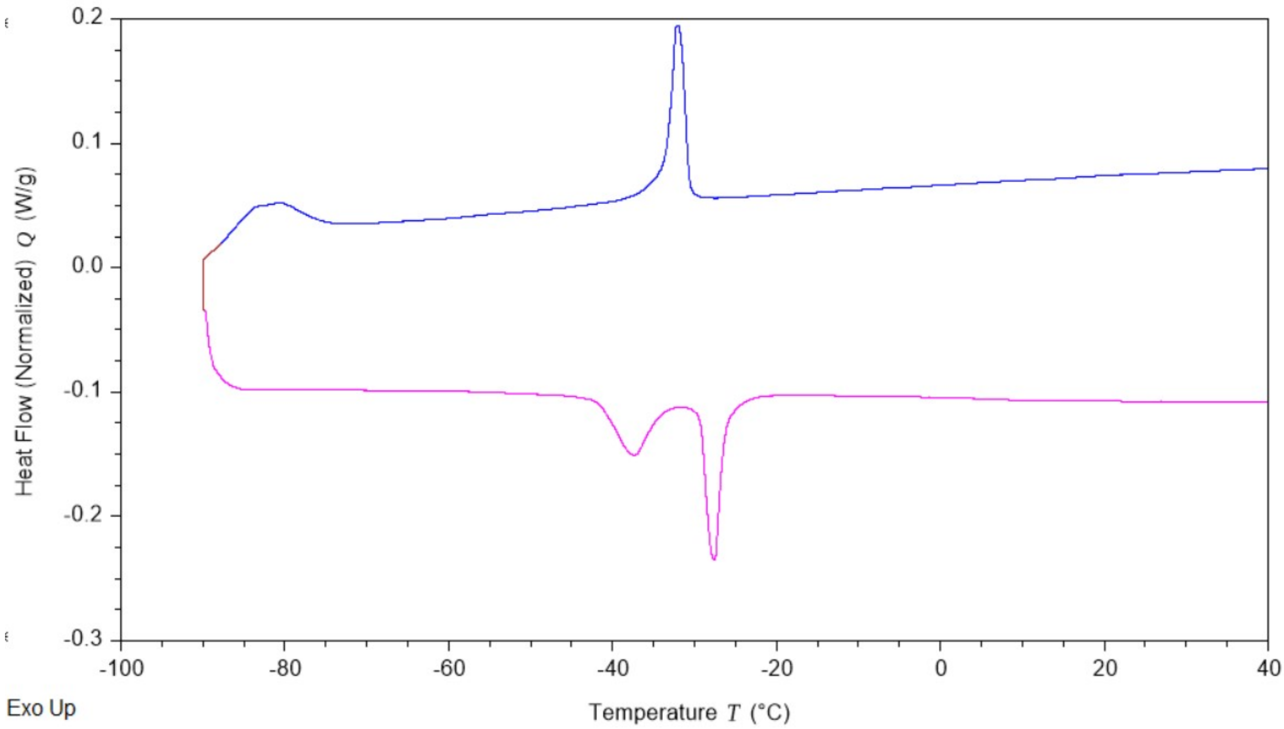

Figure S60b. Differential scanning calorimetry of $Cu[Bet]_2[Tf_2N]_2$, performed at 5 K/min.

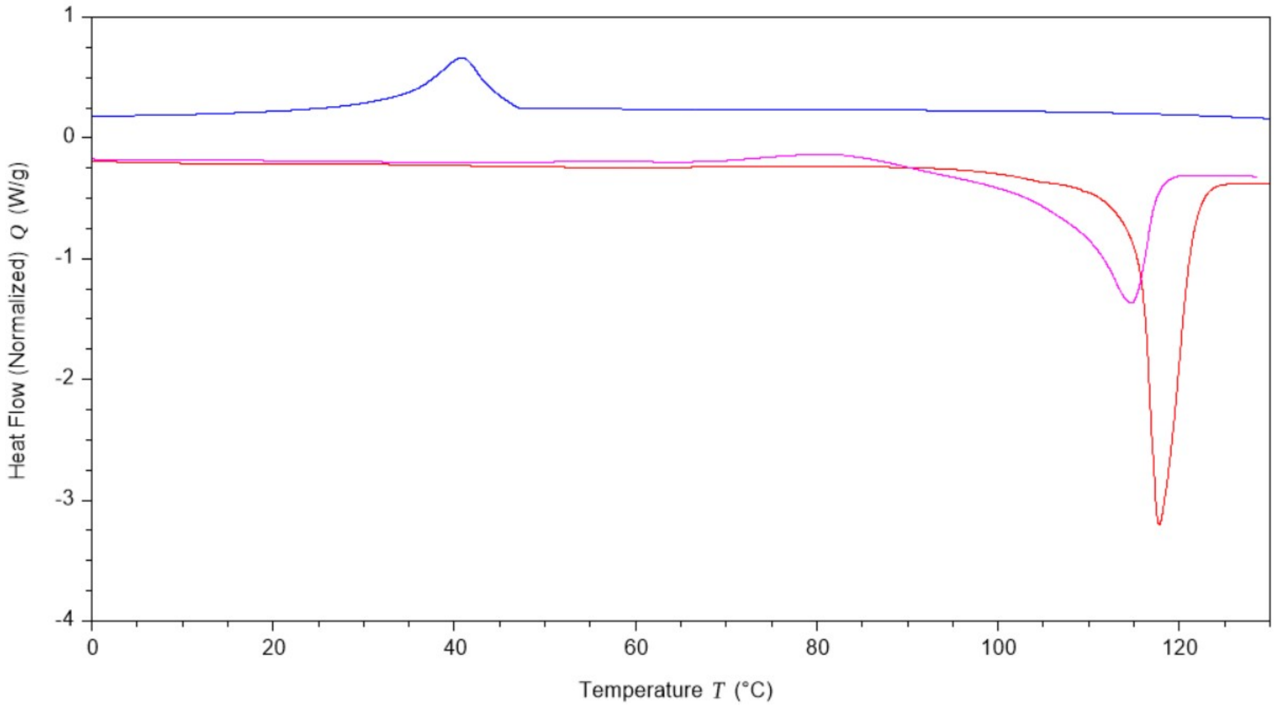

Figure S61. Differential scanning calorimetry of $Cu[Tf_2N]_2$.

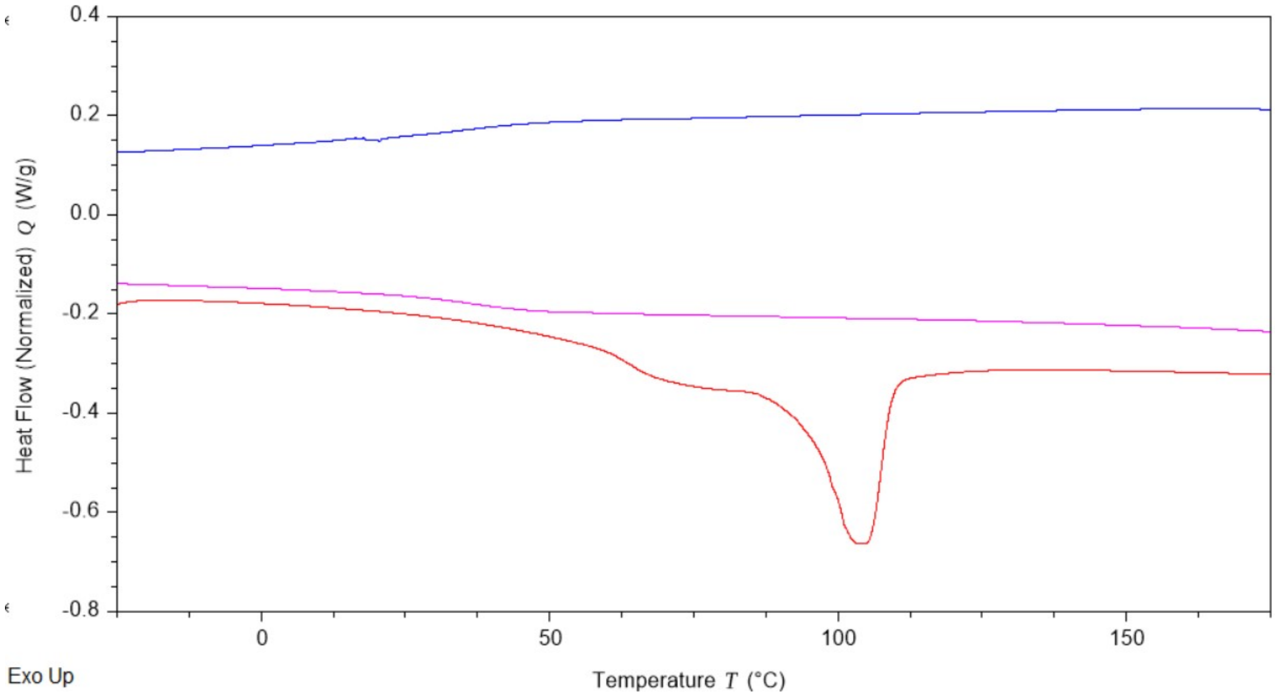

Figure S62. Differential scanning calorimetry of $Ni[Bet]_2[Tf_2N]_2$.

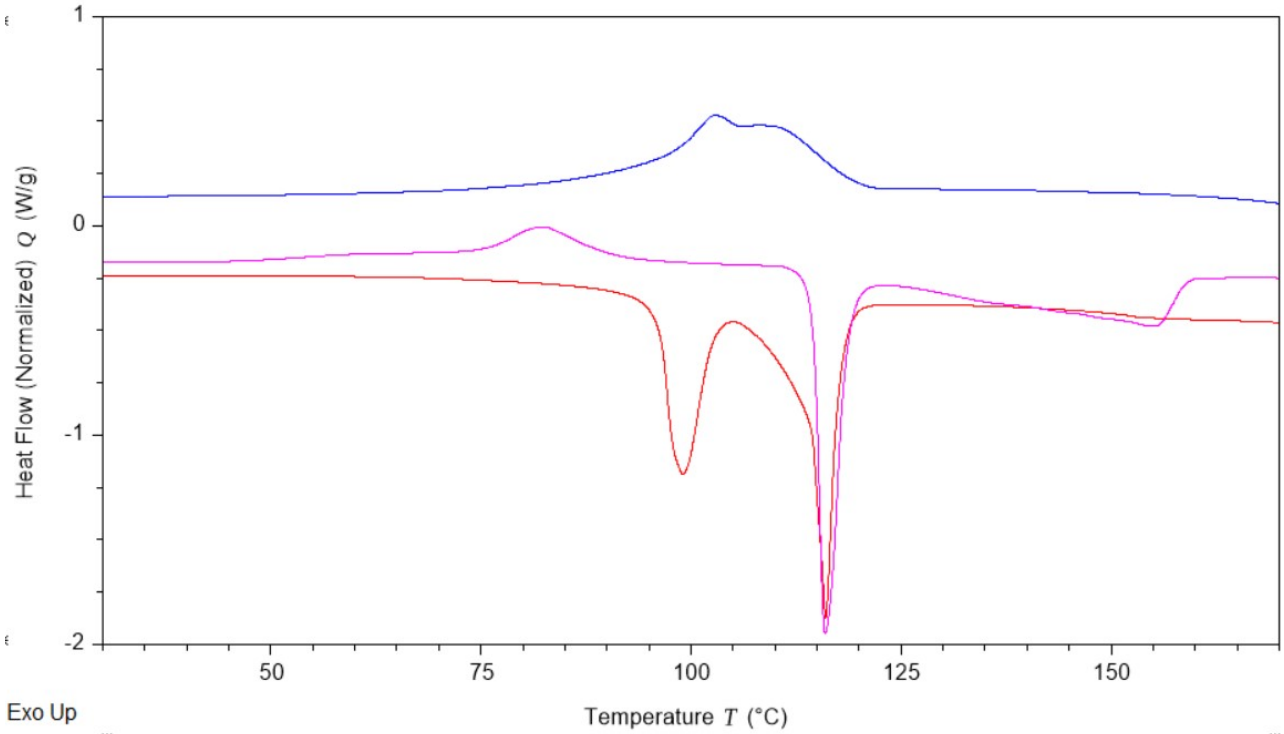

Figure S63a. Differential scanning calorimetry of $Ni[Tf_2N]_2$.

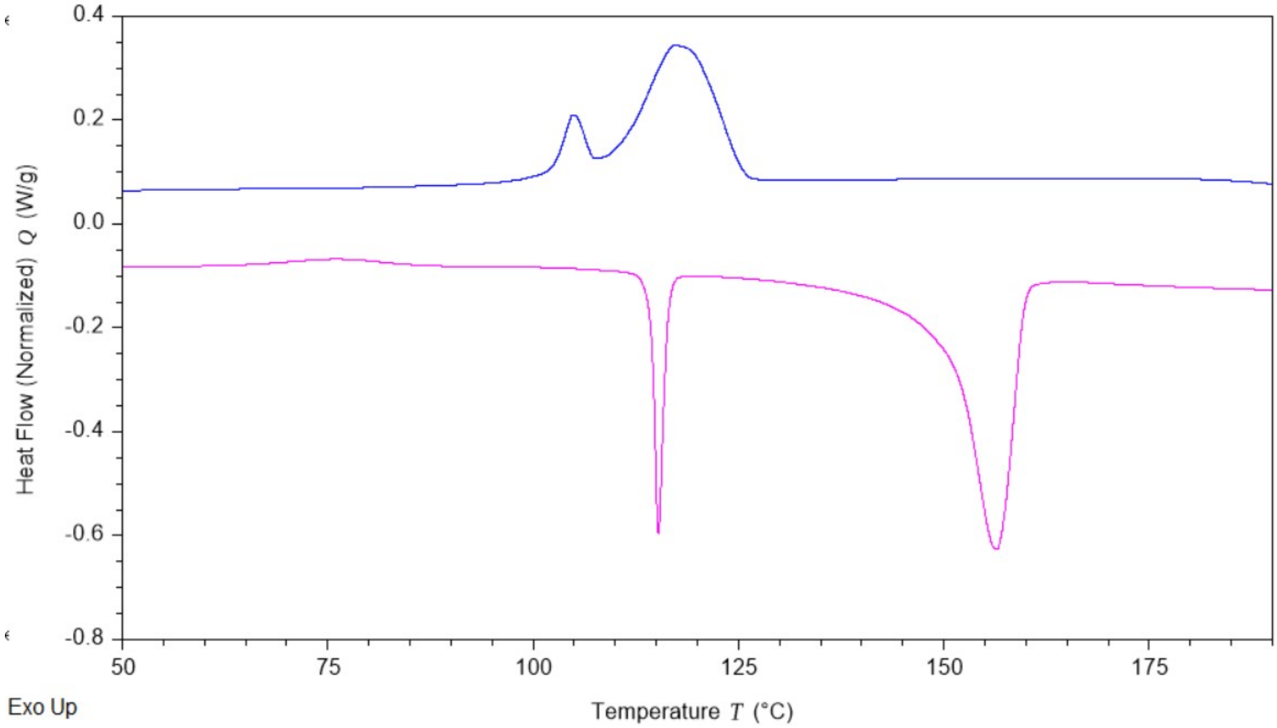

Figure S63b. Differential scanning calorimetry of $Ni[Tf_2N]_2$ performed at 5 K/min.

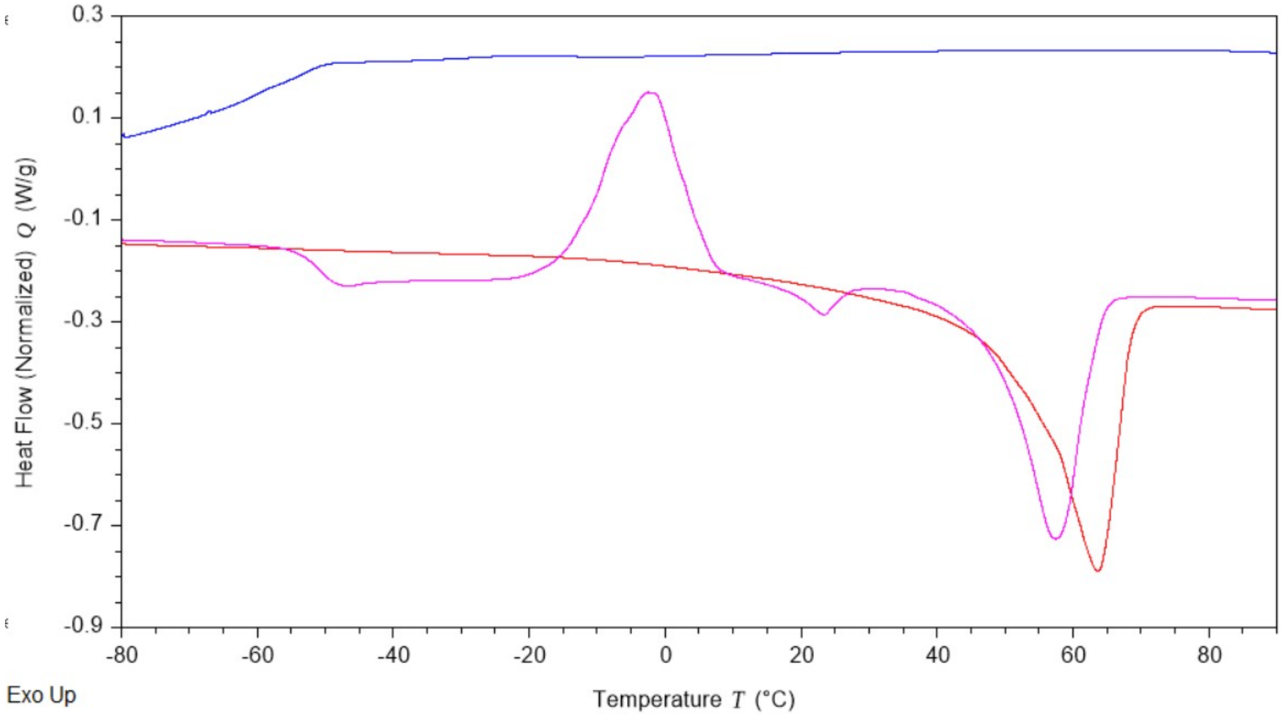

Figure S64. Differential scanning calorimetry of $H[Bet][Tf_2N]$

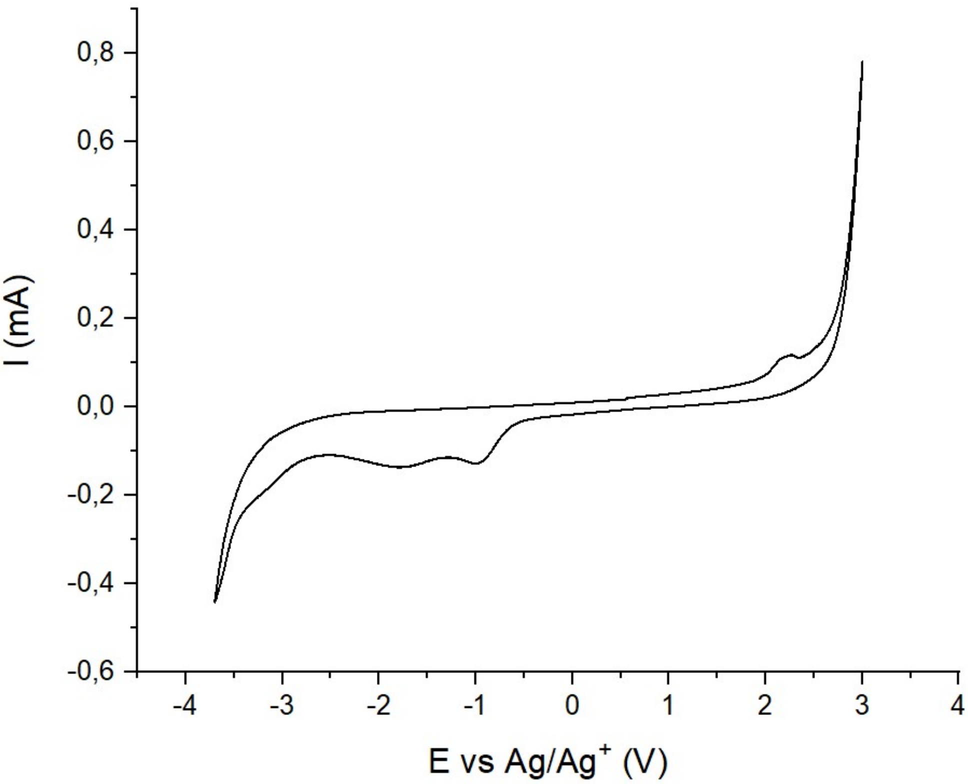

Figure S65. Cyclic voltammogram of Mg[Bet]$_2$[Tf$_2$N]$_2$ 0.1 M in MeCN, on a GC working electrode.

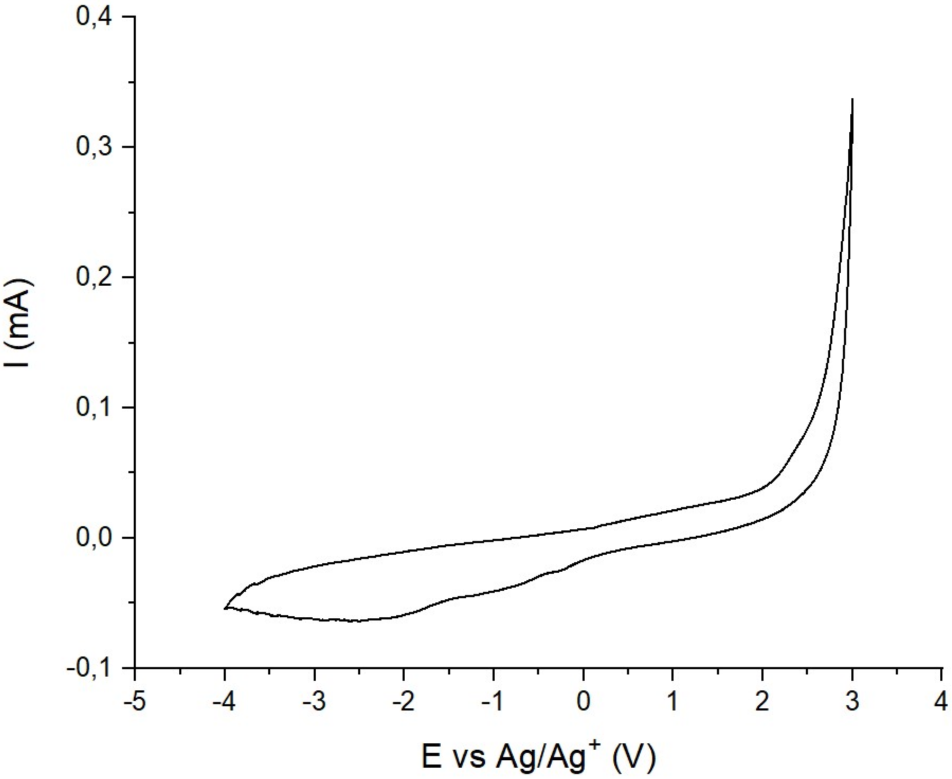

Figure S66. Cyclic voltammogram of Ca[Tf$_2$N]$_2$ 0.1 M in MeCN, on a GC working electrode.

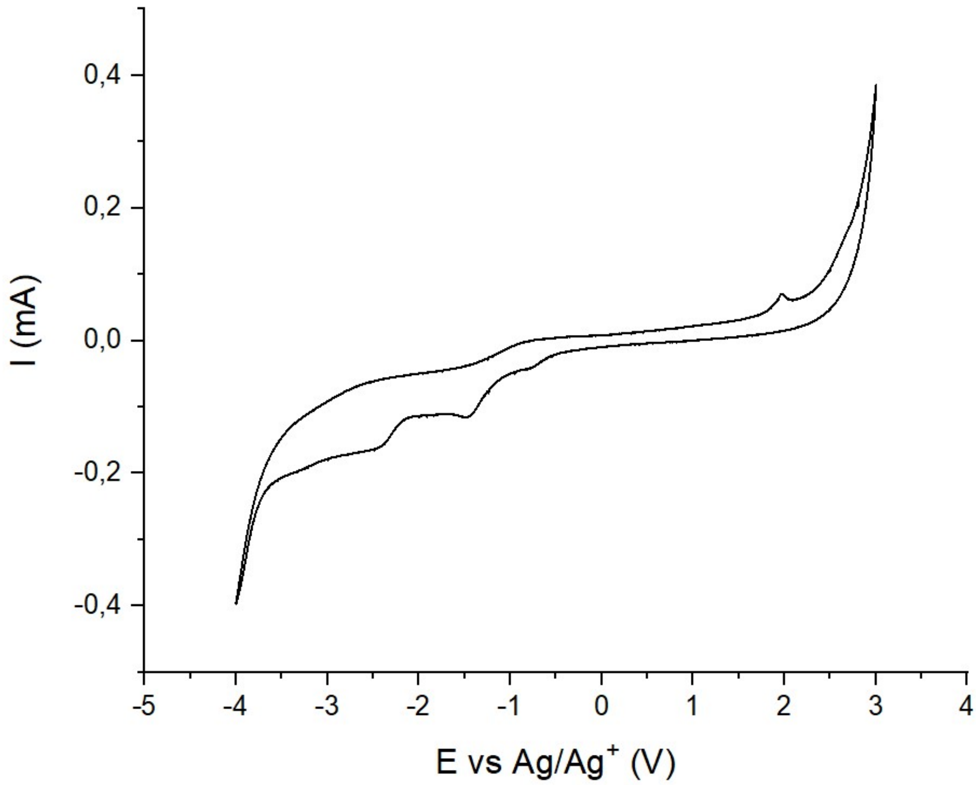

Figure S67. Cyclic voltammogram of $Ca[Bet]_2[Tf_2N]_2$ 0.1 M in MeCN, on a GC working electrode.

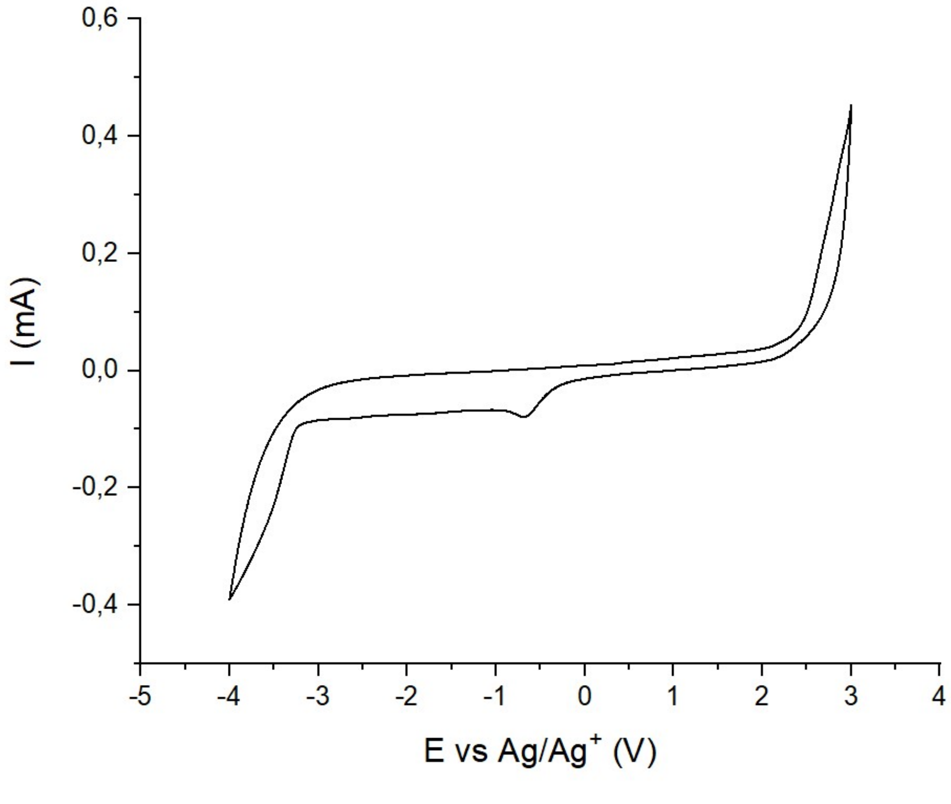

Figure S68. Cyclic voltammogram of $Ca[Tf_2N]_2$ 0.1 M in MeCN, on a GC working electrode.

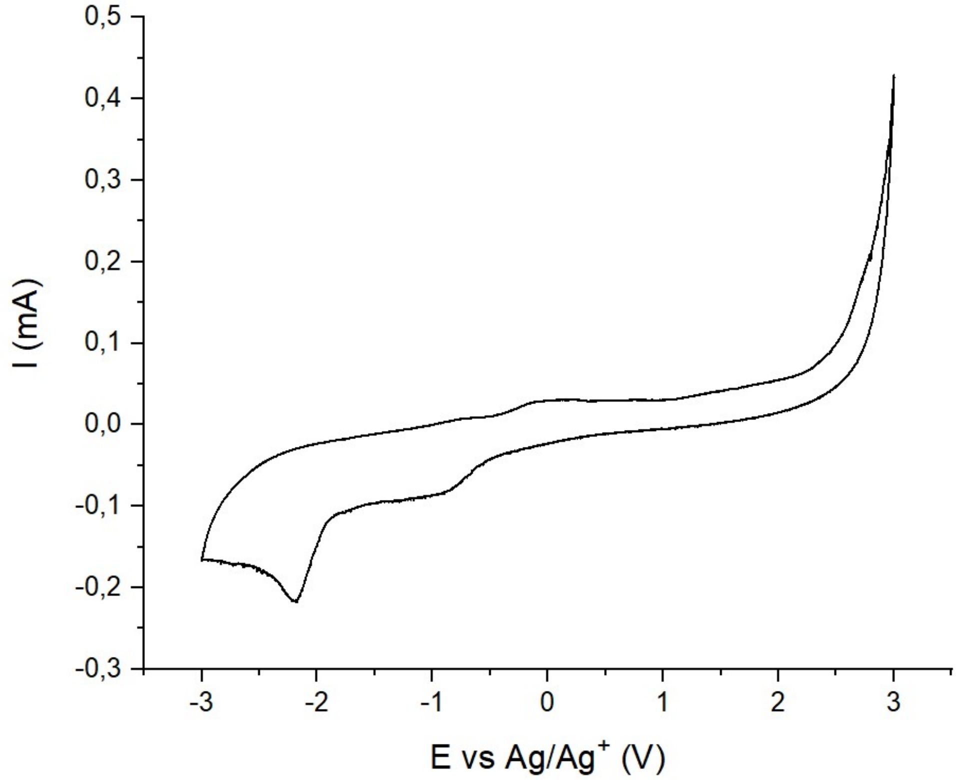

Figure S69. Cyclic voltammogram of $Zn[Bet]_2[Tf_2N]_2$ 0.1 M in MeCN, on a GC working electrode.

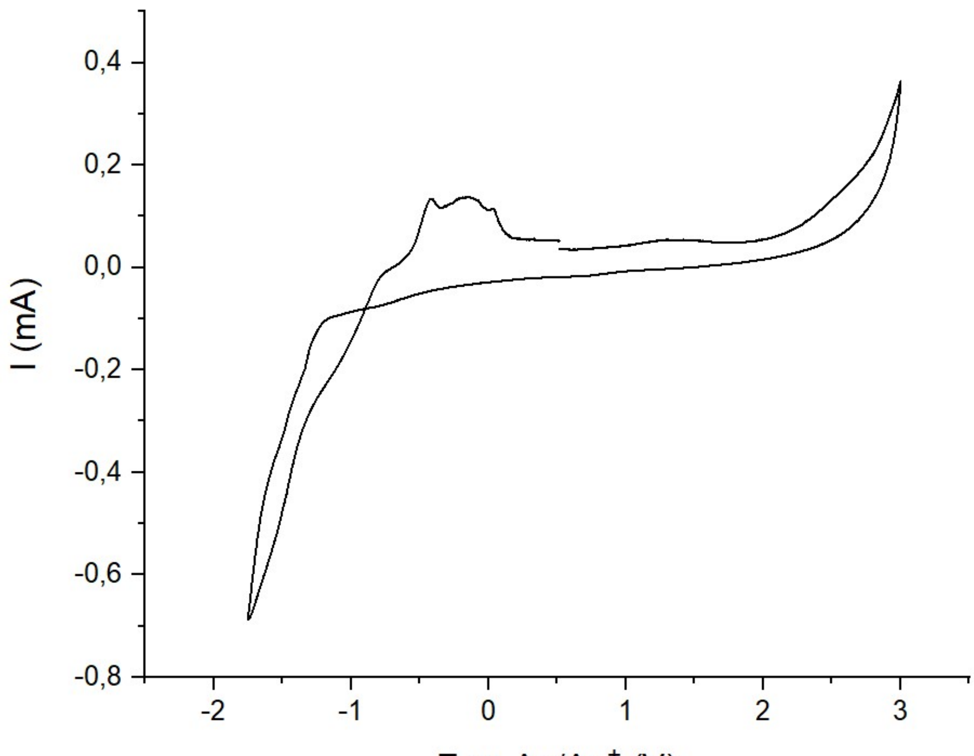

Figure S70. Cyclic voltammogram of $Zn[Tf_2N]_2$ 0.1 M in MeCN, on a GC working electrode.

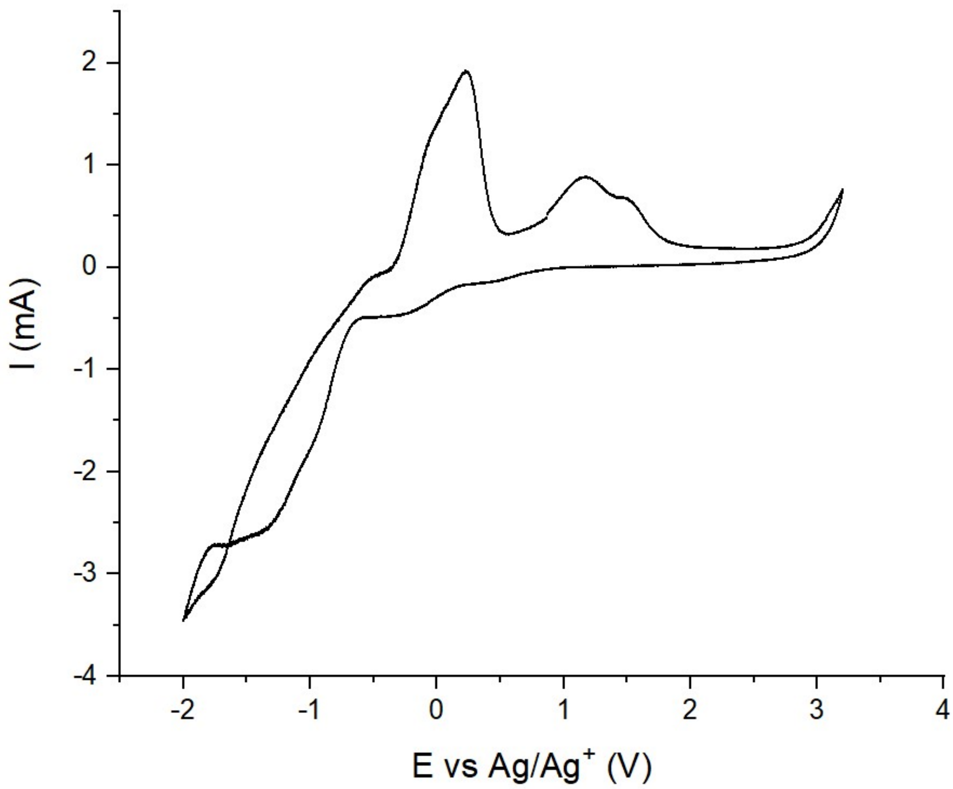

Figure S71. Cyclic voltammogram of Cu[Bet]$_2$[Tf$_2$N]$_2$ 0.1 M in MeCN, on a GC working electrode.

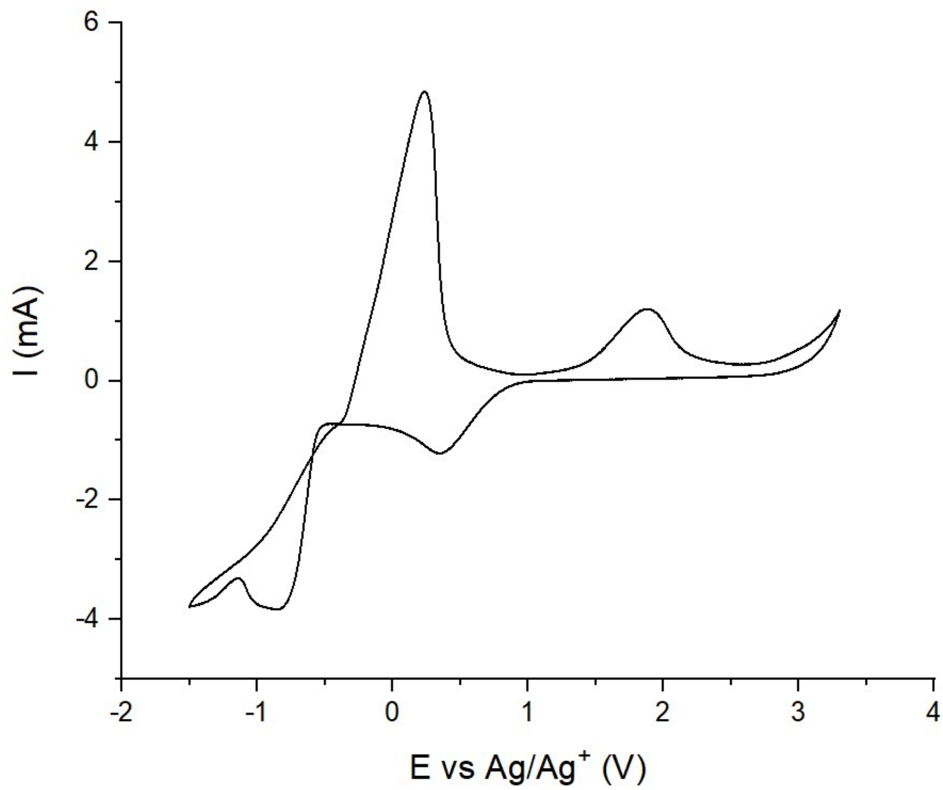

Figure S72. Cyclic voltammogram of Cu[Tf$_2$N]$_2$ 0.1 M in MeCN, on a GC working electrode.

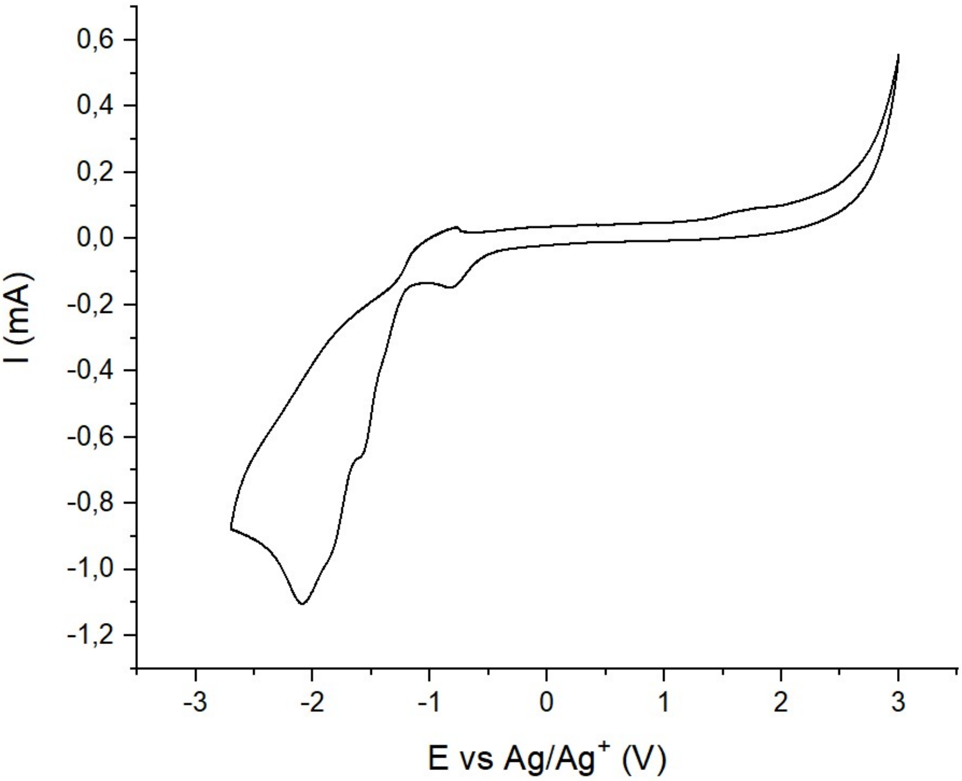

Figure S73. Cyclic voltammogram of Ni[Bet]$_2$[Tf_2N]$_2$ 0.1 M in MeCN, on a GC working electrode.

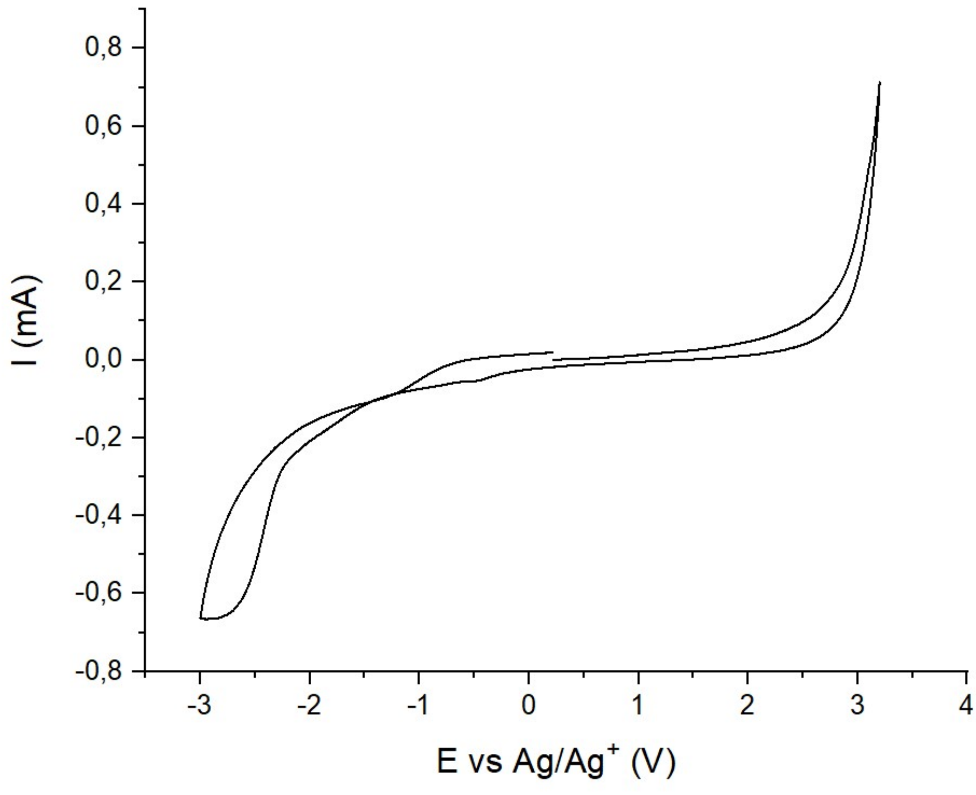

Figure S74. Cyclic voltammogram of Ni[Tf_2N]$_2$ 0.1 M in MeCN, on a GC working electrode.

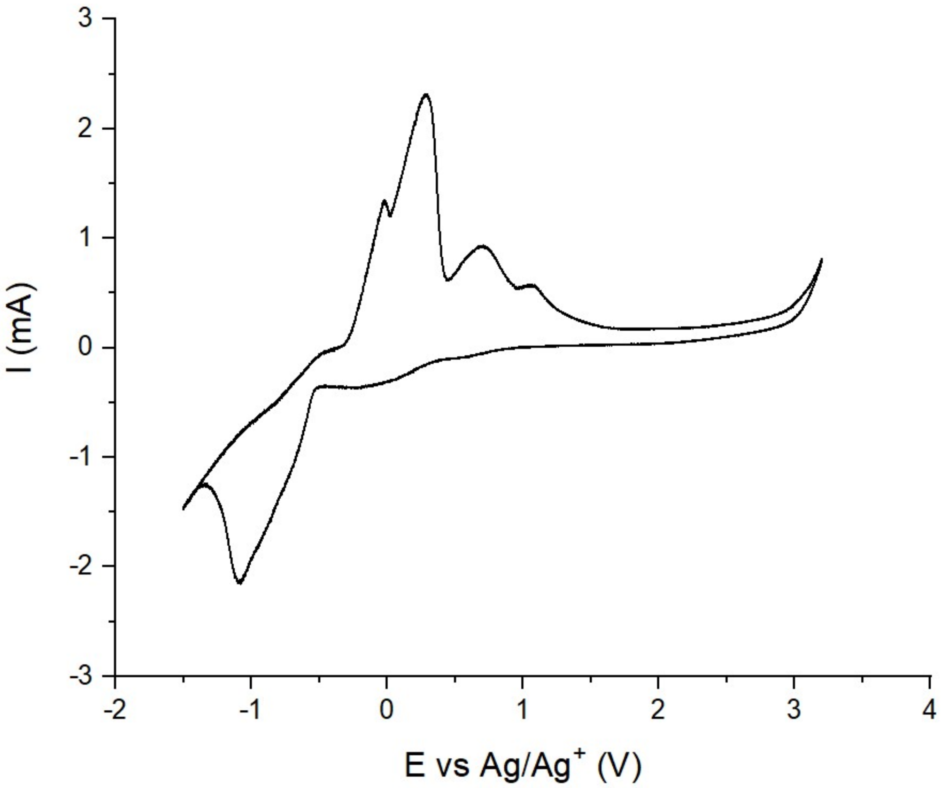

Figure S75. Cyclic voltammogram of $Cu[Bet]_2[Tf_2N]_2$ 0.1 M in MeCN, on a GC working electrode.

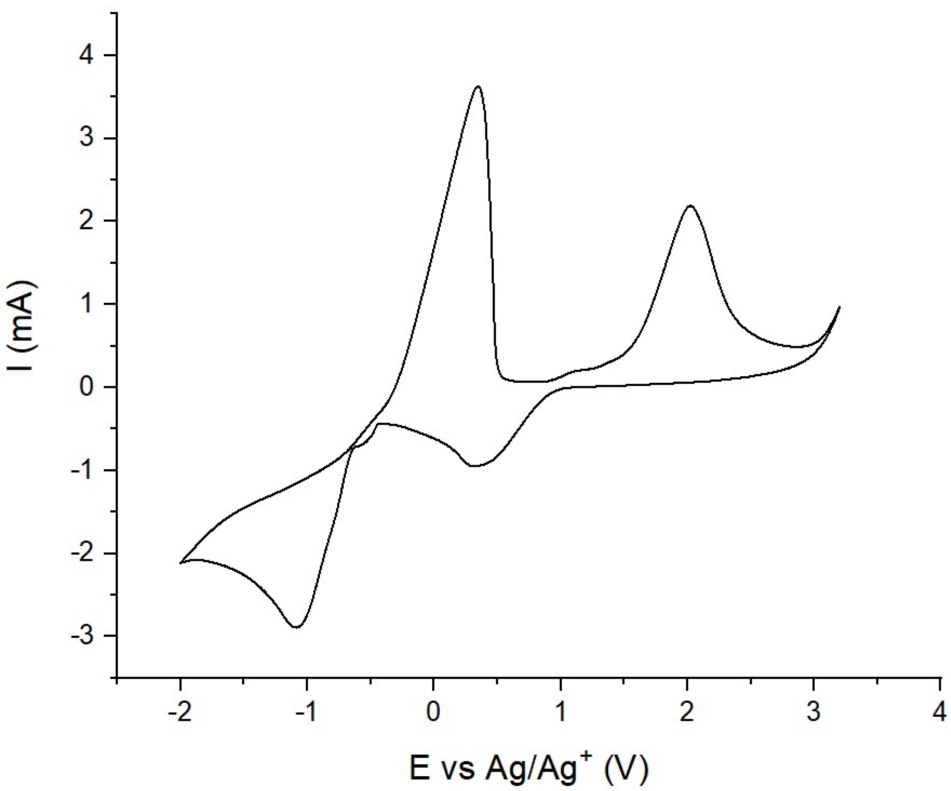

Figure S76. Cyclic voltammogram of $Cu[Tf_2N]_2$ 0.1 M in MeCN, on a Pt working electrode.

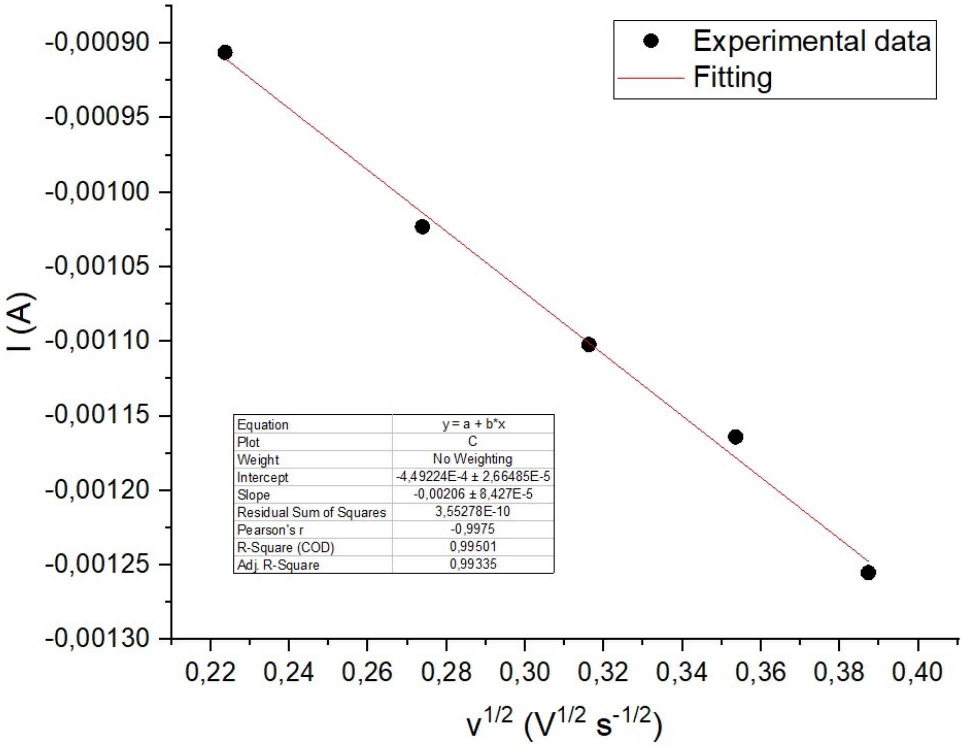

Figure S77. Fitting of data reported in Figure 6b according to Randles-Sevcik method for the determination of *D*.

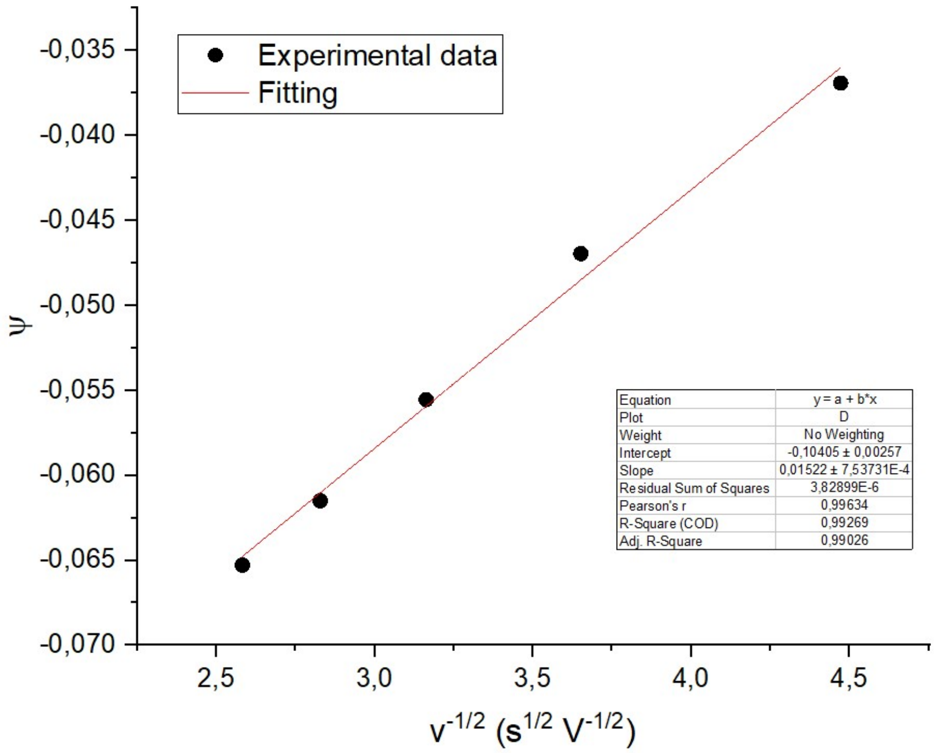

Figure S78. Fitting of data reported in Figure 6b according to Nicholson method for the determination of k_0.